



저작자표시-비영리-변경금지 2.0 대한민국

이용자는 아래의 조건을 따르는 경우에 한하여 자유롭게

- 이 저작물을 복제, 배포, 전송, 전시, 공연 및 방송할 수 있습니다.

다음과 같은 조건을 따라야 합니다:



저작자표시. 귀하는 원저작자를 표시하여야 합니다.



비영리. 귀하는 이 저작물을 영리 목적으로 이용할 수 없습니다.



변경금지. 귀하는 이 저작물을 개작, 변형 또는 가공할 수 없습니다.

- 귀하는, 이 저작물의 재이용이나 배포의 경우, 이 저작물에 적용된 이용허락조건을 명확하게 나타내어야 합니다.
- 저작권자로부터 별도의 허가를 받으면 이러한 조건들은 적용되지 않습니다.

저작권법에 따른 이용자의 권리는 위의 내용에 의하여 영향을 받지 않습니다.

이것은 [이용허락규약\(Legal Code\)](#)을 이해하기 쉽게 요약한 것입니다.

[Disclaimer](#)

공학박사학위논문

**Heat Transfer Analysis of Polymer
Composites for Thermal Insulation and Heat
Sink Applications**

단열 및 방열 소재 적용을 위한
고분자 복합재료의 열전달 해석

2016년 2월

서울대학교 대학원

재료공학부

김 형 민

Heat Transfer Analysis of Polymer Composites for Thermal Insulation and Heat Sink Applications

단열 및 방열 소재 적용을 위한 고분자 복합재료의 열전달 해석

지도교수 윤 재 룬

이 논문을 공학박사 학위논문으로 제출함
2016년 01월

서울대학교 대학원

재료공학부

김 형 민

김 형 민의 공학박사 학위논문을 인준함
2016년 01월

| | | |
|-------|-------|---|
| 위 원 장 | _____ | 인 |
| 부위원장 | _____ | 인 |
| 위 원 | _____ | 인 |
| 위 원 | _____ | 인 |
| 위 원 | _____ | 인 |

**Heat Transfer Analysis of Polymer
Composites for Thermal Insulation and
Heat Sink Applications**

Advisor : Jae Ryoun Youn

by

Hyung Min Kim

2016

Department of Materials Science and Engineering

Graduate School

Seoul National University

Abstract

The heat transfer phenomena through polymer composites is the main topic of this study. This study dealt with diverse processing techniques, morphological analysis, experimental and numerical results of thermal, mechanical behavior. The findings showed that the thermal conductivity of polymer composite decreases with increasing the interfacial thermal resistance, resulting in variation of surface structure. It was also found that nanostructures due to the generation of zinc oxide (ZnO) nanorods were more critical for the heat dissipation than the minimization of surface. This study will contribute to understanding of the underlying physics behind heat transfer phenomena, such as thermal insulation and thermal dissipation.

In chapter 2, the thermal conductivity of aerogel/epoxy composite based on the inexpensive powder form of silica aerogels by using water glass under ambient drying conditions was evaluated to investigate the relationship between the internal structure and the thermal conductivity of the composite. A processing method for preserving the aerogel pores was then developed using ethanol evaporation, which lowered the thermal conductivity of the composite. To enhance the morphostasis of silica aerogel composite, a fabrication method was designed by applying the thermal characteristics of silica aerogels with preservation of pores in the aerogel to achieve extremely low thermal conductivity of the composites. A new process was proposed to generate interfaces between superhydrophobic silica aerogels and a hydrophilic polyvinyl alcohol (PVA) solution and to fabricate the silica aerogel/PVA composite forcibly while PVA is precipitated over the interfaces by making the solvent vaporize at a slow rate during stirring.

In chapter 3, we demonstrated the synergistic effect of dual scale shape memory polyurethane (SMPU) foams that recovered from the compressed shape to their initial dimension above the transition temperature. Such a recovery leads to an enhancement in the thermal features, especially thermal resistance. Dual scale shape memory foams were fabricated by using the salt leaching method and their internal

structure was analyzed morphologically. The porosity and interfacial thermal resistance of the dual scale foam were enhanced significantly, which leads to the excellent thermal resistance compared with other single scale foams. The thermal behavior of foamed materials was modelled analytically. The synergistic effect on mechanical properties, which was induced by the dual size pores, was explained by the result of numerical simulation. In addition, thermo-mechanical properties of the shape memory foam such as shape recovery, shape fixity, and shape repeatability were characterized. SMPU filled with carbon nanotubes (CNTs) has been investigated to actuate by thermo-response. Although the pure SMPU foam was not responsive to microwave radiation, the microwave absorption dosage in the SMPU/CNT foams considerably could be increased with adding amount of CNTs. When exposed to microwave radiation, the embedded CNTs were absorbed the external electromagnetic energy and reacted as heat sources in the SMPU/CNT foamed material were heated volumetrically and led to response fast. The influences of the CNTs on the mechanical and thermal properties of the SMPU foams with 0.01 wt%, 0.05 wt% and 0.1 wt% CNTs were investigated. The shape recovery behaviors of the SMPU foams were also characterized by microwave radiation.

In chapter 4, we studied a new approach where structurally gradient nanostructures were fabricated by means of hydrodynamics. ZnO nanorods were synthesized in a drag-driven rotational flow in a controlled manner. The structural characteristics of nanorods such as orientation and diameter were determined by momentum and mass transfer at the substrate surface. The nucleation of ZnO was induced by shear stress that plays a key role in determining the orientation of ZnO nanorods. The nucleation and growth of such nanostructures were modelled theoretically and analyzed numerically to understand the underlying physics of the fabrication of nanostructures controlled by hydrodynamics. The findings demonstrated that the precise control of momentum and mass transfer enabled the formation of ZnO nanorods with a structural gradient in diameter and orientation. The study also describes the hydrothermal growth of ZnO nanostructures on graphene/polyethylene phthalate (PET) films and their thermal properties. The ZnO nanostructures were

grown on graphene sheets of a few layers thick with seed layer. The dimensions and density of the ZnO nanorods could be easily controlled by changing the hydrothermal growth conditions such as temperature, number of spin coating and concentration of growth solution. Moreover, the interfacial effect induced by ZnO nanostructures was investigated to analyze the thermal behavior of ZnO/graphene/PET film such as heat dissipation, heat flux.

Keywords: heat transfer phenomena, thermal conductivity, silica aerogel, shape memory polyurethane, zinc oxide, nanostructure, thermal insulation, thermal dissipation, interfacial effect, size effect, finite element analysis

Student Number: 2010-20595

Contents

| | |
|--|-----|
| Abstract | i |
| List of Figures | vii |
| List of Tables | xii |
| | |
| I. Introduction | |
| 1.1. Nanomaterial | |
| 1.1.1. Silica aerogel | 13 |
| 1.1.2. Carbon nanotubes (CNTs) | 15 |
| 1.1.3. Graphene | 21 |
| 1.1.4. Zinc Oxide (ZnO) | 24 |
| 1.2. Shape Memory Polyurethane (SMPU) | 29 |
| 1.3. Theoretical background | |
| 1.3.1. Conduction | 32 |
| 1.3.2. Radiation | 35 |
| 1.3.3. Heat transfer in foam material | 37 |
| 1.4. Objectives of Present Work | 38 |
| 1.5. References | 39 |
| | |
| II. Aerogel Composite | |
| 2.1. Silica aerogel/epoxy composites with preserved aerogel pores and low thermal conductivity | |
| 2.1.1. Introduction | 45 |
| 2.1.2. Experimental Section | 47 |
| 2.1.3. Results and Discussion | 52 |
| 2.1.4. Summary | 59 |
| 2.1.5. References | 60 |

2.2. Silica aerogel/polyvinyl alcohol(PVA) insulation composites with preserved aerogel pores using interfaces between the superhydrophobic aerogel and hydrophilic PVA solution

| | |
|----------------------------------|----|
| 2.2.1. Introduction | 62 |
| 2.2.2. Experimental Section | 64 |
| 2.2.3. Results and Discussion | 69 |
| 2.2.4. Summary | 77 |
| 2.2.5. Supplementary Information | 78 |
| 2.2.6. References | 82 |

III. Shape Memory Polyurethane foam

3.1. Synergistic Effect of Dual-Scale Hybrid Shape Memory Foam

| | |
|----------------------------------|-----|
| 3.1.1. Introduction | 85 |
| 3.1.2. Experimental Section | 87 |
| 3.1.3. Theoretical Section | 92 |
| 3.1.4. Results and Discussion | 94 |
| 3.1.5. Summary | 105 |
| 3.1.6. Supplementary Information | 106 |
| 3.1.7. References | 111 |

3.2. Shape memory polyurethane foams embedded CNTs and their remote shape control induced microwave radiation

| | |
|-------------------------------|-----|
| 3.2.1. Introduction | 115 |
| 3.2.2. Experimental Section | 117 |
| 3.2.3. Results and Discussion | 121 |
| 3.2.4. Summary | 130 |
| 3.2.5. References | 131 |

IV. ZnO/GO/PET film

4.1. Hydrodynamic fabrication of structurally gradient ZnO nanorods

| | |
|---|-----|
| 4.1.1. Introduction | 134 |
| 4.1.2. Experimental Section | 136 |
| 4.1.3. Results and Discussion | 138 |
| 4.1.4. Summary | 147 |
| 4.1.5. Supplementary Information | 148 |
| 4.1.6. References | 152 |
| | |
| 4.2. Heat diffusion of flexible ZnO/GO/PET film | |
| 4.2.1. Introduction | 155 |
| 4.2.2. Experimental Section | 158 |
| 4.2.3. Results and Discussion | 162 |
| 4.2.4. Summary | 169 |
| 4.2.5. References | 170 |
| | |
| V. Concluding Remarks | 174 |
| | |
| Korean Abstract | 177 |

List of Figures

- Figure 1.1.** The several structures of CNTs.
- Figure 1.2.** The Stone-Wales transformation occurring in an armchair nanotube under axial tension.
- Figure 1.3.** Schematic diagram of roll-up of graphene sheet leading to the three different types of CNTs.
- Figure 1.4.** Atomic structure and energy-momentum distribution of graphene.
- Figure 1.5.** Diverse growth forms of zinc oxide(ZnO): Nanorods, Nanowires, Nanobelt, Nanocomb, Nanohelix, Nanoring, Nanocage.
- Figure 1.6.** Enhancement of Surface area of nanomaterials at nanoscale.
- Figure 1.7.** Zinc Oxide crystal structure: Hexagonal Wurtzite, Cubic Zinc Blende, Cubic Rock salt.
- Figure 1.8.** Mechanism of the thermally induced shape memory effect. T_{trans} = thermal transition temperature related to the switching phase.
- Figure 1.9.** Dodecaeder model for a foam cell. (a) Perspective view. (b) Cross-section through struts and walls.
- Figure 2.1.1.** Particle and pore size distribution of the as-received aerogel.
- Figure 2.1.2.** Schematic diagram of the processing method for preserving aerogel pores.
- Figure 2.1.3.** Thermal conductivity of the aerogel/epoxy composites with respect to the volume fraction of the aerogel.
- Figure 2.1.4.** SEM images of the aerogel/epoxy composites with (A) as-received aerogel of 25 vol%, (B) as-received aerogel of 75 vol%, (C) plasma-treated aerogel of 25 vol%, (D) plasma-treated aerogel of 75 vol%, (E) 25 vol% preserved aerogel pores, and (F) 75 vol% preserved aerogel pores.
- Figure 2.1.5.** SEM images of pristine and plasma-treated aerogels. The white arrows indicate the particle size of the individual particles of the aerogel.
- Figure 2.2.1.** Processing procedures for preparation of silica aerogel/PVA composites.

Figure 2.2.2. Thermal conductivity of raw materials and silica aerogel/polymer composites.

Figure 2.2.3. SEM images of (a) as-received silica aerogel powder and silica aerogel/epoxy composites with (b) 25, (c) 50 and (d) 75 vol % aerogel.

Figure 2.2.4. SEM images of the silica aerogel/PVA composites with (a) 3 % concentration of PVA solution with high magnification, (b) 3 % concentration of PVA solution, (c) 10 % concentration of PVA solution and (d) 20 % concentration of PVA solution.

Figure 2.2.5. Thermal conductivity of silica aerogel/PVA composites with respect to (a) the concentration in the PVA solution at a hot plate temperature of 20 °C and (b) the hot plate temperature with the 10 wt% PVA solution.

Figure 2.2.6. Thermogravimetric analysis curves for the silica aerogel/PVA composites with respect to (a) the concentration of the PVA solution at a hot plate temperature of 20 °C and (b) the hot plate temperature with the 10 wt% PVA solution.

Figure S2.2.1. Schematic diagram of the aerogel synthesis. In the first step of the synthesis, water glass was used as the starting material and silica sol with a silica content of 29 wt% was prepared using distilled water. For surface modification and gelation, hexamethyldisiloxane and nitric acid were added to the silica sol. The hydrogel obtained by the co-precursor method was immersed in an n-Hexane solvent at 60 °C for 10 h in order to exchange the solvent and remove ions, including sodium. The modified gel was dried continuously at 170 °C for 20 min and 200 °C for 10 min under the ambient pressure.

Figure. S2.2.2. Image of the interface between the silica aerogel and the PVA solution with respect to the volume of the raw materials.

Figure 3.1.1. Processing procedure for preparation of SMPU foams.

Figure 3.1.2. SEM images of SMPU foam specimens: (a) SMPU foam-100, (b) SMPU foam-200, (c) SMPU foam-400, (d) functionally gradient SMPU foam, and (e) hybrid SMPU foam and (f) porosity of the SMPU foams.

Figure 3.1.3. Experimental and theoretical thermal conductivity of SMPU foams.

Figure 3.1.4. Numerical simulation results: (a) 3 dimensional unit cell of SMPU foam-

400, (b) 3 dimensional unit cell of hybrid SMPU foam, (c) compressive stress field of SMPU foam-400, and (d) compressive stress field of hybrid SMPU foam.

Figure 3.1.5. (a) Compressive stress-strain curves of SMPU foams, (b) moduli of the SMPU foams, and (c) comparison of experimental and numerical specific compressive moduli of SMPU foams.

Figure 3.1.6. Results of each thermo-mechanical cyclic loading of the SMPU foam-400 specimen for 4 cycles.

Figure 3.1.7. (a)-(c) SEM images of SMPU foam-400: (a) original, (b) compressed, and (c) recovered states, (d) porosity of SMPU foam-400 in the thermo-mechanical cycle, and (e) thermal conductivity and thermal resistance of SMPU foam-400 in the thermo-mechanical cycle.

Figure S3.1.1. SEM images of the filtered NaCl particles: sintered glass filter size of (a) 100, (b) 200, and (c) 400 μm and particle size distribution of the filtered NaCl particles. Average particle size of the NaCl was (d) 127.5, (e) 242, and (f) 413.8 μm .

Figure S3.1.2. Shape recovery and shape fixity of SMPU foam specimens.

Figure S3.1.3. DSC result of the synthesized SMPU.

Figure S3.1.4. 3D unit cell images (a) SMPU foam-400, and (b) hybrid SMPU foam.

Figure 3.2.1. Processing procedure for preparation of SMPU/CNT foams.

Figure 3.2.2. Thermal conductivity of SMPU foams as a function of CNTs weight fraction.

Figure 3.2.3. SEM images of SMPU/CNT foam specimens: (a) SMPU foam with 0.1 wt% of CNTs, (b) raw SMPU foam, (c) SMPU foam with 0.1 wt% of CNTs.

Figure 3.2.4. Thermogravimetric analysis curves for the SMPU/CNT foams with respect to CNTs weight fraction.

Figure 3.2.5. (a) Compressive stress-strain curves of SMPU/CNT foams, and (b) normalized Young's moduli of SMPU foams as a function of CNTs weight fraction.

Figure 3.2.6. DSC results of the SMPU foams as a function of CNTs weight fraction.

Figure 3.2.7. (a) Temperature versus time for the SMPU/CNT foams with microwave radiation, and (b) shape recovery and shape fixity of SMPU foam specimens as a function of CNTs weight fraction.

Figure 4.1.1. Schematic diagrams of (a) the experimental procedures for the primary nucleation of ZnO seeds by heterogeneous nucleation, the secondary nucleation of ZnO nuclei by shear flow, and the growth of ZnO nanorods under shear stress and (b) a conceptual model of velocity boundary thickness and concentration boundary layer thickness developed by shear stress.

Figure 4.1.2. Simulation results: (a) 3 dimensional velocity field, (b) velocity profiles in the rotating flow, (c) shear rate as a function of the radius of Si substrate, (d) predicted normalized nucleation density of ZnO nanorods, (e) concentration distribution, and (f) predicted concentration boundary layer thickness as a function of the radius of Si substrate.

Figure 4.1.3. SEM images of the ZnO nanorods grown: the case without shear stress at (a) the center, (b) center-periphery, and (c) edge of Si substrate and the case with shear stress at (d) the center, (e) center-periphery, and (f) edge of Si substrate

Figure 4.1.4. XRD patterns of ZnO nanorods grown at (a) the center, (b) centre-periphery, and (c) edge of Si substrate

Figure 4.1.5. Diameter histograms of the ZnO nanorods grown under shear stress at (a) the center of Si substrate, (b) centre-periphery of Si substrate, and (c) edge of Si substrate and (d) correlation between the average diameter of ZnO nanorods and the radius of Si wafer.

Figure S4.1.1. SEM images of ZnO nanorods grown with different temperature of the nutrient solution. (a) 40 °C (b) 70 °C (c) 90 °C.

Figure S4.1.2. SEM images of ZnO nanorods grown with different concentration of ZnO colloid at temperature of 90 °C. (a) 0.03M (b) 0.05M.

Figure S4.1.3. SEM images of ZnO nanorods grown with three spin coating times under shear stress at a rate of 100 rpm. (a) schematic diagram of experiment (b) center of Si substrate (c) centre-periphery of Si substrate (d) edge of Si substrate.

Figure 4.2.1. Processing procedure for preparation of ZnO/rGO/PET films.

Figure 4.2.2. SEM images of graphene film specimens: (a) rGO/PET film, (b) rGO/PET with sparse ZnO nanostructures, and (c) rGO/PET with abundant ZnO

nanostructures.

Figure 4.2.3. Raman spectra of graphene oxide/PET and reduced graphene oxide film.

Figure 4.2.4. XPS spectra of (a) graphene oxide/PET film, and (b) reduced graphene oxide/PET film.

Figure 4.2.5. XRD spectra of graphene oxide/PET film and reduced graphene oxide/PET films with ZnO nanostructures.

Figure 4.2.6. Temperature profiles of rGO/PET with and without ZnO nanostructures.

List of Tables

Table 1.1. Physical properties of CNTs.

Table 2.1.1. BET results of the composites with respect to the volume fraction of the aerogel.

Table 2.2.1. Physical properties of materials used for the experiment.

Table 2.2.2. Surface area and density of the silica aerogel composites.

Table S2.2.1. Success or failure of specimen preparation under different process conditions.

I. Introduction

1.1. Nanomaterial

1.1.1. Silica aerogel

Silica aerogel is extremely nano-porous materials with a high porosity (75 ~ 99.87 %) and open pores (1 ~ 100 nm pore size) [1-4]. Silica aerogel is formed by dispersion of a gas in a solid and can be considered as the opposite of aerosols. In the past, silica aerogel was prepared from wet gels by using the supercritical drying technique, which removed the formation of interfaces between liquid and vapor within the gel network and induced a surface tension that caused a shrinkage of their structure. Recently, materials called aerogels can be maintained to typical structure and network although a liquid of a gel is replaced by air [5]. In 1931, Kistler tried to eliminate the wet gel prepared from aqueous waterglass [6, 7]. By replacing a liquid by a gas without a shrinkage, silica aerogel as well as aerogel of alumina, tungsten oxide, ferric oxide, tin oxide and cellulose were fabricated successfully. In the late 1970s, Teichner *et al.* developed a better synthetic process including a time-consuming and laborious solvent exchange step to enhance Kistler's method [8]. In this process, the waterglass was replaced with a tetramethylorthosilicate (TMOS) and this technique led to major advances in the application of sol-gel chemistry. In 1983, Hunt and the Microstructured Materials Group at Lawrence Berkely Lab. (LBL) investigated that TMOS was changed to the much safer tetraethylorthosilicate (TEOS) due to its toxic component and the alcohol within an alcogel could be changed to liquid carbon dioxide before supercritical drying process without collapsing the structural network [9]. This represented major advances in safety because the critical point of CO₂ (31 °C and 1050 psi) can be occurred under much less extreme conditions than the critical point of methanol (240 °C and 1600 psi). In the late 1980s, Hrubesh and researchers at

Lawrence Livermore National Laboratory (LLNL) fabricated silica aerogel with the lowest density (0.003 g/cm^3) and developed the techniques by using inorganic aerogels such as resorcinolformaldehyde (RF) and melamine-formaldehyde (MF) aerogels [10]. Organic aerogel could be pyrolyzed to manufacture carbon aerogels. It can be expanded a completely new area in aerogel research field. However, the expensive, energy-intensive, and dangerous supercritical drying must be substituted with cost-effective and safe ambient drying in order to fabricate aerogels for large scale in commercial application [11, 12]. In recent years, several research groups have further developed the ambient drying process to make it more cost-effective and safe.

Silica aerogel has numerous applications due to its high porosity, high internal surface area ($500 \sim 1200 \text{ m}^2/\text{g}$), low dielectric constant ($1.1 \sim 2.2$), low refractive index ($1.0 \sim 1.1$), light weight, and low thermal conductivity (up to $0.03 \text{ W/m}\cdot\text{K}$) [13-18]. Silica aerogels are preferred application for high-temperature insulations because the low thermal conductivity and the thermal stability of silica aerogels. Silica aerogels are commonly used as the thermal insulation in refrigerators and steam pipes. For example, Rover Space Vehicle which used in the Mars Pathfinder Mission by NASA was protected with an aerogel insulation tile. Silica aerogels are investigated as transparent insulation materials (TIM) such as house wall insulation and window glazing materials (smart glazing) because of their transparency, non-flammability and excellent thermal properties [19-22]. For large-scale application of TIM, Wittwer *et al.* developed the TIM system which was long-time stability, high optical transmission, and sufficient heat resistance [23]. Silica aerogels are also successfully used as heat-storage systems [24]. Due to an ultra-low dielectric constant (k), silica aerogel films can be utilized for inter-metal dielectric (IMD) materials [25, 26]. The chemical-vapor-deposited dense silica aerogel films are currently employed as IMD in order to minimize interconnect resistance, capacitance delay, power consumption, and cross talk. Silica aerogel films have also advantages such as thermal stability ($< 600 \text{ }^\circ\text{C}$) and small pore size in applications for the thin film dielectrics: microwave striplines, extremely lightweight electronic packages, spacers for electrodes in vacuum tubes [27].

1.1.2. Carbon nanotubes (CNT)

Carbon nanotubes (CNTs) were first reported by Iijima in 1991 and many researchers have been investigating CNT-based nanocomposites due to excellent electrical, thermal and mechanical properties [28-31]. Typically, the CNTs have diameter of nanometer size, length of micro size, aspect ratio above 1000 because CNTs have graphite sheets rolled into a cylinder of several microns in length and a few nanometers in diameter.

These CNTs can exist as diverse forms as shown in figure 1.1. The CNTs consist from one to many layers of carbon atom such as single-walled carbon nanotubes (SWCNTs), double-walled carbon nanotubes (DWCNTs), multi-walled carbon nanotubes (MWCNTs) and ropes [32].

As the CNTs have defects generated during synthesis process, Stone-Wales defect have occurred frequently. It is comprised of two structures that are five and seven membered rings such as a 7-5-5-7 defect in figure 1.2. By the Stone-Wales defect, deformation of the curvature and attachment of the functional group are occurred at the carbon-carbon double bonds [33]. Moreover, the binding energy of atoms of functional groups on the wall of CNTs should be increased with decreasing tube diameter [34].

Three important vectors, such as the chiral vector, translational vector, and symmetry vector, determine the structure of nanotubes. Figure 1.3 shows the structure of CNTs and the characteristic chiral vector well known as the roll-up vector which can be described by the following [35].

$$\vec{C}_h = n\vec{a}_1 + m\vec{a}_2 \quad (1.1)$$

where the intergers (n, m) are the number of steps along the unit vectors (\vec{a}_1 and \vec{a}_2) of the hexagonal lattice. There are three kinds of CNTs depending on the orientation of

carbon atoms around the nanotube circumference such as armchair ($n = m$), zigzag ($n = 0$ or $m = 0$) and chiral (all others). The chirality, roll-up vector of nanotube defines the nanotube diameter as well as the properties of CNTs such as electronic and mechanical properties of the CNT. For example, CNTs can be either metallic or semiconducting depending on tube roll-up vector, chirality [36]. Moreover, the properties of CNTs depend on atomic arrangement, length of the tube, and the nanostructure. The physical properties of CNTs and graphite are shown in Table 1.1. According to these properties, CNTs can be used in various fields such as conductive inks, transparent organic electrodes and flexible display panels [37].

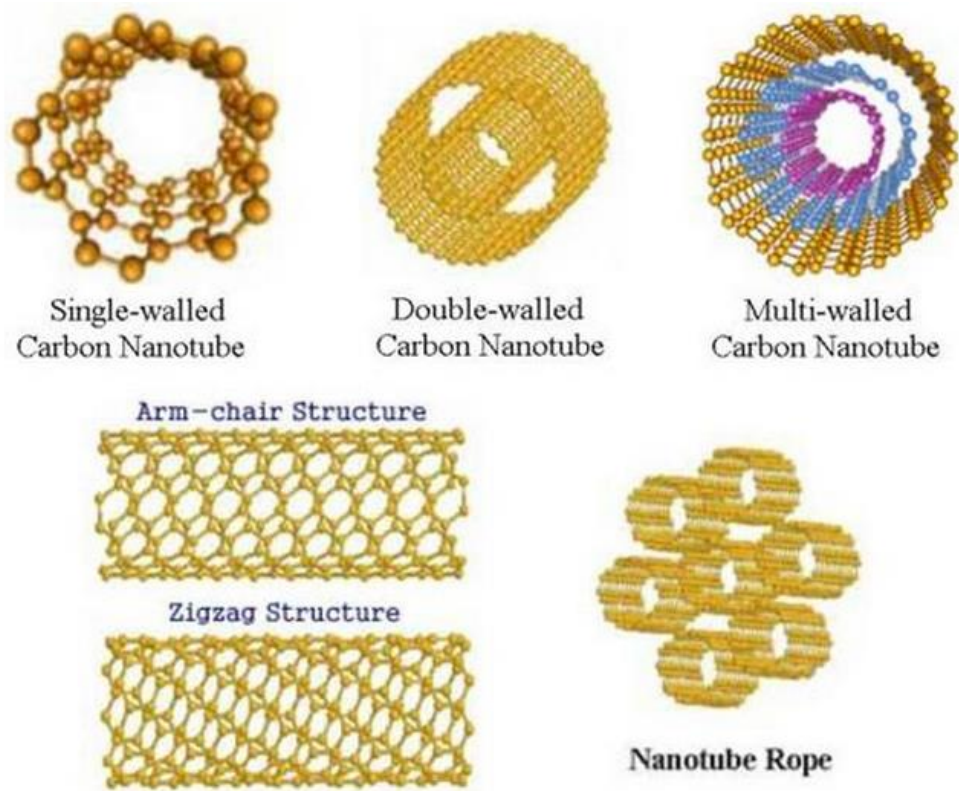


Figure 1.1. The several structures of CNTs.

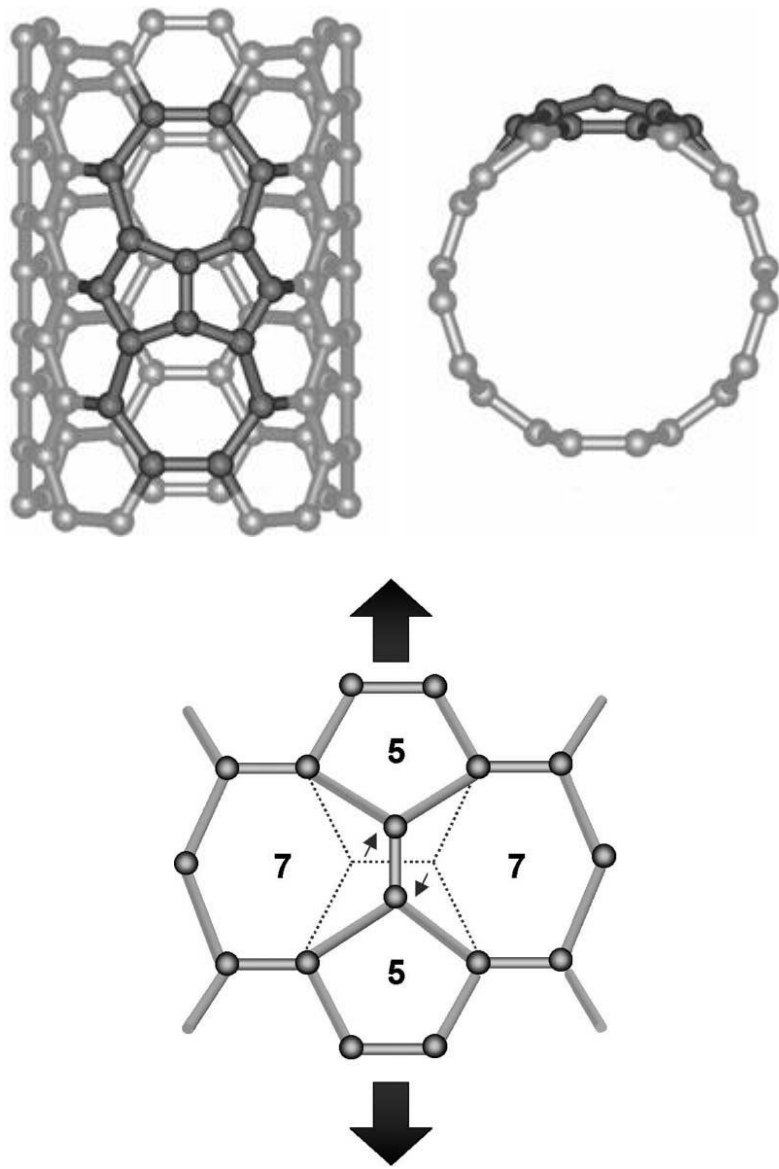


Figure 1.2. The Stone-Wales transformation occurring in an armchair nanotube under axial tension.

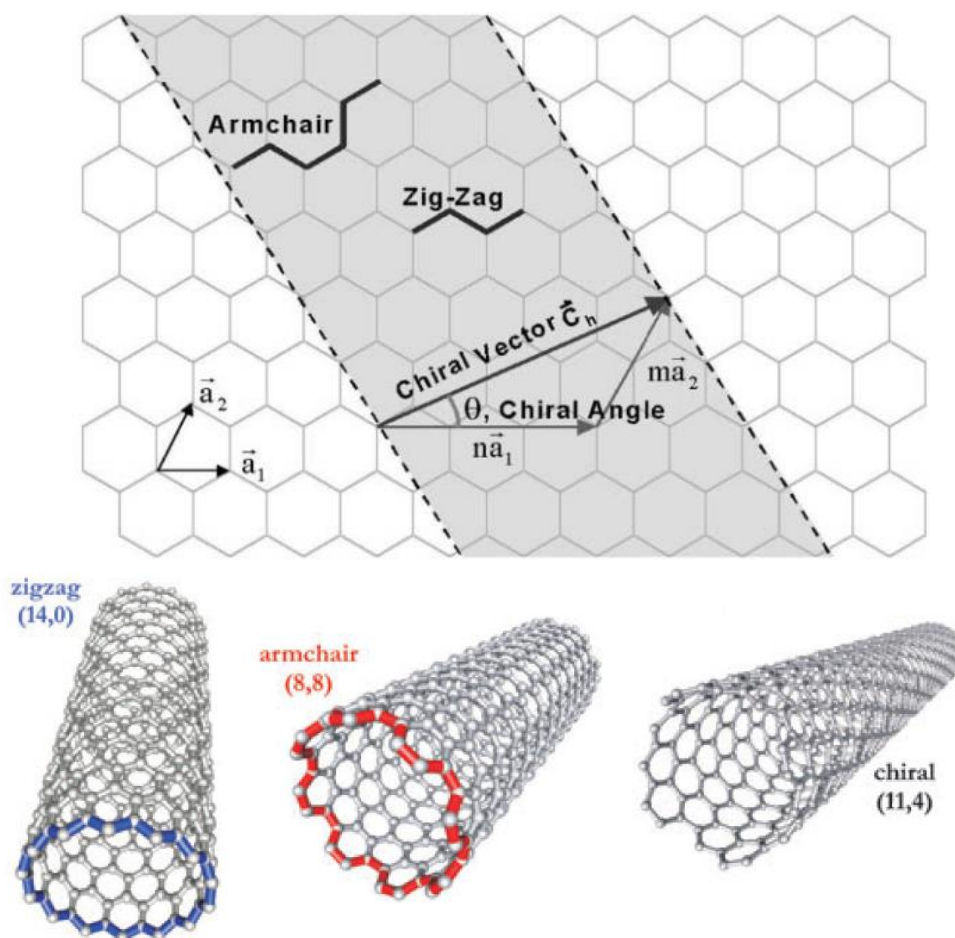


Figure 1.3. Schematic diagram of roll-up of graphene sheet leading to the three different types of CNTs.

Table 1.1. Physical properties of CNTs.

| Properties | SWCNTs |
|-----------------------|---|
| Specific Gravity | 0.8 g/cm ³ |
| Elastic Modulus | ~1 TPa |
| Strength | 50 – 500GPa |
| Resistivity | 5 – 50 $\mu\Omega$ cm |
| Thermal Conductivity | 3000 W m ⁻¹ K ⁻¹ |
| Thermal Stability | >700 °C (in air); 2800°C (in vacuum) |
| Specific Surface Area | ~400-900m ² /g |

| Properties | MWCNTs |
|-----------------------|---|
| Specific Gravity | 1.8 g/cm ³ |
| Elastic Modulus | ~0.3 – 1 TPa |
| Strength | 10 – 60 GPa |
| Resistivity | 5 – 50 $\mu\Omega$ cm |
| Thermal Conductivity | 3000 W m ⁻¹ K ⁻¹ |
| Thermal Stability | >700 °C (in air); 2800°C (in vacuum) |
| Specific Surface Area | ~200 – 400m ² /g |

1.1.3. Graphene

Graphene, a carbon nanomaterial, is a one-atom thick planar sheet of sp^2 -bonded carbon atoms that are densely packed in a hexagonal honeycomb crystal lattice as shown in figure 1.4 [38]. The band structure of graphene was previously predicted to be Dirac cone shape band structure, which has linear band structure at K point resulting in zero effective mass of carriers. On the basis of fundamental study, graphene has become one of the most exciting topics of research since it was experimentally discovered in 2004 [39].

Graphene can be enable to be used in various kinds of application because of the unique and excellent properties of graphene [40]. The thermal conductivity of graphene can be dominantly affected by phonon transport rather than carrier density because intrinsic graphene has relatively low carrier density. By simulation results, the theoretical thermal conductivity of graphene can be predicted to 6,000 W/m·K [41]. In addition, the experimental thermal conductivity of graphene was measured to be about 5,000 W/m·K which is about 10 times higher than that of copper [42]. Even though graphene is atomically thin layer, it is the strongest material ever discovered because of its inherent strength. The graphene has ultimate tensile strength of 130 GPa which is about 300 times higher than that of steel. Moreover, experimental spring constants and a Young's modulus were measured to be $1 \sim 5$ N/m and 0.5 TPa, respectively [43]. Recently, the flexibility of the graphene film was experimentally investigated and related researches represented that the graphene film can be elongated until 11 % extension. Unique electronic properties of graphene can be explained by its abnormal band structure. Since electron and hole have zero effective mass in graphene, these Dirac fermions can be ballistically transported. For this reason, the highest theoretical mobility could be observed in graphene transistor and is about 140 times higher than that of Si. Moreover, corresponding mobility was also experimentally investigated [44]. Graphene can be used as a transparent conductive electrode. Although the resistance of intrinsic graphene is actually quite high due to the zero density of state at Dirac points, conductivity can be significantly increased because the Fermi level and carrier density

can be tuned by doping [45]. Graphene is transparent because only 2.3 % of white light per one layer is absorbed. Theoretical opacity of graphene can also be investigated by using $(1 - T) \approx \pi\alpha \approx 2.3 \%$ which is based on the fine structure constant of graphene [46]. Graphene can be used as transparent conducting material because of these properties of graphene. Although there exist few commercial applications until now, it can be seen that graphene will be applied to various fields in the future.

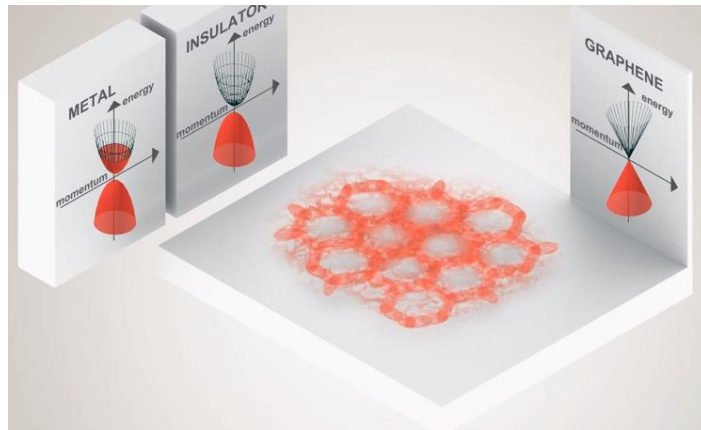
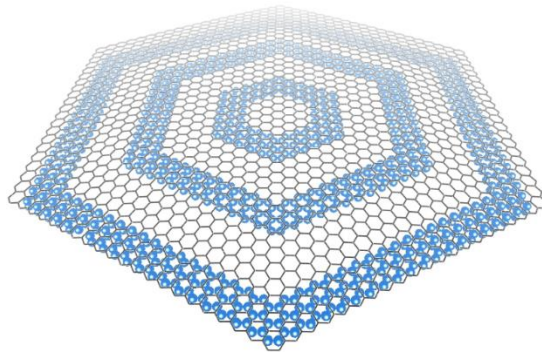
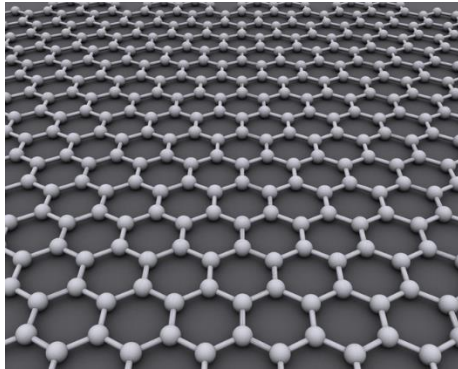


Figure 1.4. Atomic structure and energy-momentum distribution of graphene.

1.1.4. Zinc oxide (ZnO)

Now that a basic idea has been developed to study nanomaterials. In the 1960s, zinc oxide (ZnO) played a major role in photonic devices, sensors and transducers. However, its new properties and applications have been discovered with the recent advances in nanotechnology.

Study of 1D transport phenomena is one of investigation method that helps us understand electrical, thermal and mechanical properties of nanomaterials. Studying a low dimensional system is not only for the understanding the physical phenomena but also for developing larger, more complex and functional systems. ZnO has carried out a key role in this study mainly due to the various morphologies such like nanocombs, nanorings, nanohelices, nanowires, nanorods and nanocages as shown in figure 1.5 [47].

Several researches show that nanoscale ZnO has many novel properties which are not observed in its bulk state. This is mainly due to effects of quantum confinement and enhanced surface area [48]. Nanoscale material has drastic effects on the surface area to volume ratio as seen in figure 1.6. As the surface area can be increased by nanomaterial, the reaction areas can be larger. As a results, this effect can be influenced to chemical properties as well as mechanical, thermal, electrical and optical properties.

ZnO is made up three crystalline structures as shown in figure 1.7. The hexagonal structure is the most general form and is stable at room temperature. Zincblende can be grown by sing another cubic lattice as the base. Rocksalt only occurs at very high pressures. Both the hexagonal and cubic structures have no inversion symmetry. In this study, we have focused primarily on the Wurtzite structure which composed of a covalent crystal and a hexagonal closed packing with the following lattice parameters: $a = 3.296 \text{ \AA}$ and $c = 5.2065 \text{ \AA}$. All the atoms are tetrahedrally coordinated and stacked alternately as shown in figure 1.7. This coordination results in non-symmetry of the crystal. Another important factor is the charged surfaces because one of the facets (0001) has a positive charge, the opposite side has a negatively charged oxygen surface. Such charged surface normally

undergoes surface reconstruction due to a net dipole moment along the axis. Therefore, ZnO remains perfectly flat and stable.

ZnO nanostructures have many novel properties which are used for a wide range of applications. It has a large band gap of 3.37 eV and high excitation energy of 60 mV. It can be seen that ZnO nanostructures are ideal materials for photo diodes in the blue-UV region. By constructing a nanostructure, it is possible to control the heat transfer. Nanomaterials have a lower thermal conductivity compared to the bulk forms. Due to the effect of surface area, this leads to increased phonon dispersion which inhibits thermal transport across the system. ZnO nanostructures will be very effective in thermo-electric devices by fabricating at local hotspots in electronics. ZnO nanostructures have a piezoelectric property by the strong dipole moment in the ZnO crystal. On exerting a pressure along the cornering direction of the tetrahedron, the charge centers are distorted which gives rise to electric dipole. This phenomenon can be applied in resonators, probes in scanning probe microscopy and sensors.

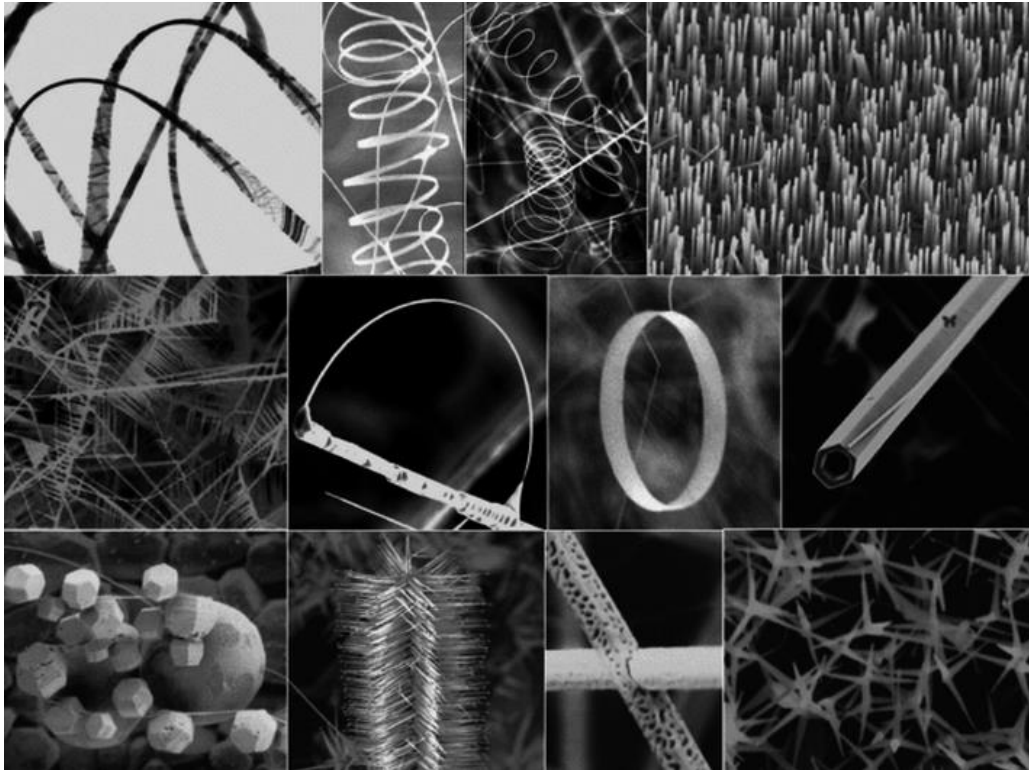


Figure 1.5. Diverse growth forms of zinc oxide(ZnO): Nanorods, Nanowires, Nanobelt, Nanocomb, Nanohelix, Nanoring, Nanocage.

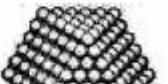
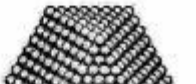
| Full-shell Clusters | | Total Number of Atoms | Surface Atoms (%) |
|---------------------|---|-----------------------|-------------------|
| 1 Shell |  | 13 | 92 |
| 2 Shells |  | 55 | 76 |
| 3 Shells |  | 147 | 63 |
| 4 Shells |  | 309 | 52 |
| 5 Shells |  | 561 | 45 |
| 7 Shells |  | 1415 | 35 |

Figure 1.6. Enhancement of Surface area of nanomaterials at nanoscale.

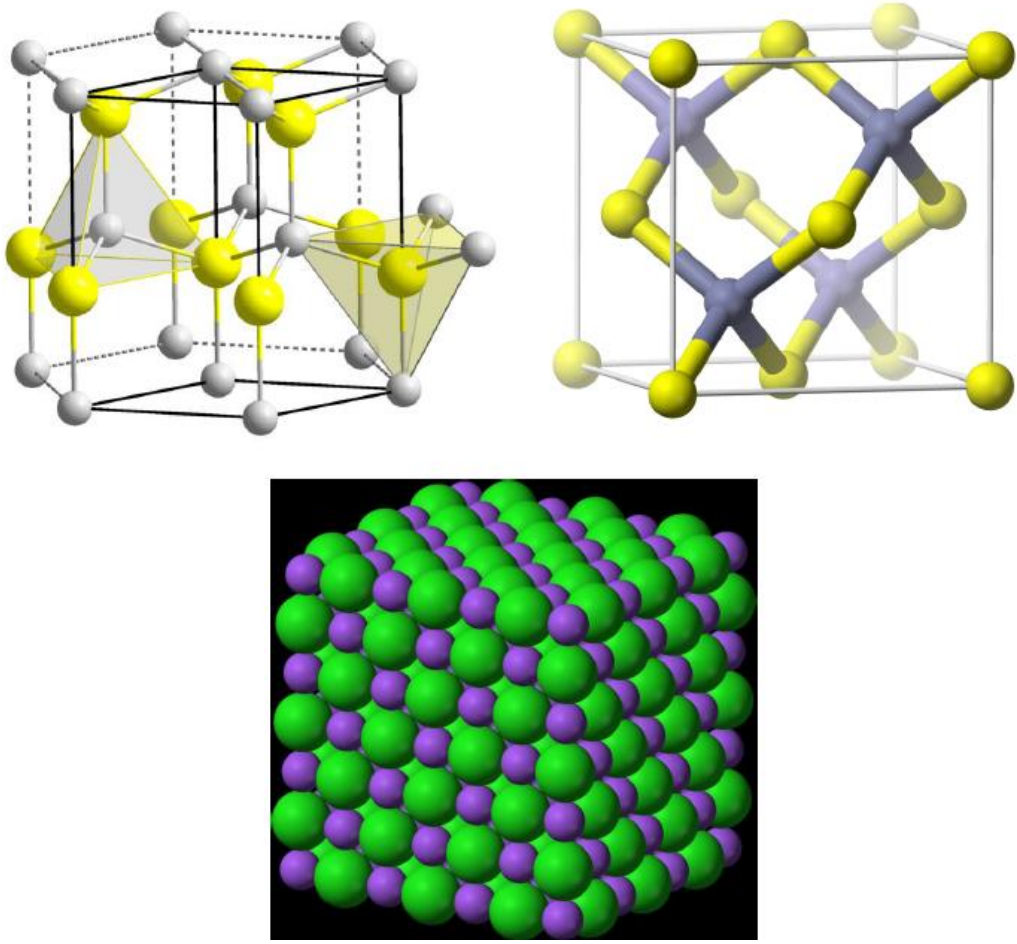


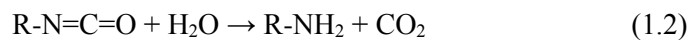
Figure 1.7. Zinc Oxide crystal structure: Hexagonal Wurtzite, Cubic Zinc Blende, Cubic Rock salt.

1.2. Shape Memory Polyurethane (SMPU)

Polyurethane (PU) is composed of urethane links which is formed by reacting diisocyanates with polyols. PU is a polymer having a broad scope of thermal, mechanical and chemical properties. Therefore, it is used in a wide range of industrial applications such as thermal insulation, furniture, packaging and appliances. When occasion demands, PU can be manufactured to diverse forms such as coatings, adhesives, fibers, thermoplastic elastomers and foams.

Shape memory effects have been observed in diverse polymers such as polynorbornene, styrene-butadiene copolymer and polyurethane [49, 50]. PU is one of the shape memory polymers (SMPs) which can change actively in response to external stimuli such as heat, light, moisture, pH and electric field [51]. Figure 1.8 shows the mechanism of the shape memory effect of SMPs based on the formation of structure separated phase. A shape memory polyurethane (SMPU) is a block copolymer which consists of hard segments and soft segments. These two segments have been separated in the structure due to the thermodynamic incompatibility. Physical properties of the SMPU are influenced by the degree of the phase separation. Therefore, the appropriate SMPU can be fabricated by controlling the ratio of the hard segment and soft segment and adjusting molecular weights of each segment [52].

Typically, SMPU foams were used as insulating materials because they have a low thermal conductivity as well as a morphostasis [53]. There are several methods to manufacture SMPU foams such as chemical blowing agent method, physical blowing method and salt leaching method. The distilled water which generate carbon dioxide by reacting with isocyanate is frequently used as chemical blowing agent. As a result, polyuria group can be formed as amine reacts with isocyanate.



Foam structure can be generated when carbon dioxide occurs in the mixture and

additional isocyanate will be needed to react with water [54]. Chlorofluorocarbons (CFC) and hydrochlorofluorocarbon (HCFC) gases are widely used as physical blowing agent. As CFC or HCFC gases change phases from liquid to vapor, a porous structure can be formed [55, 56]. In this study, cellular SMPU specimens were fabricated by the salt leaching method which is one of particulate leaching method [57, 58]. The manufacture method is simple and it is easy to control the porosity and the pore size of the foam by changing the size and the amount of the salt particles.

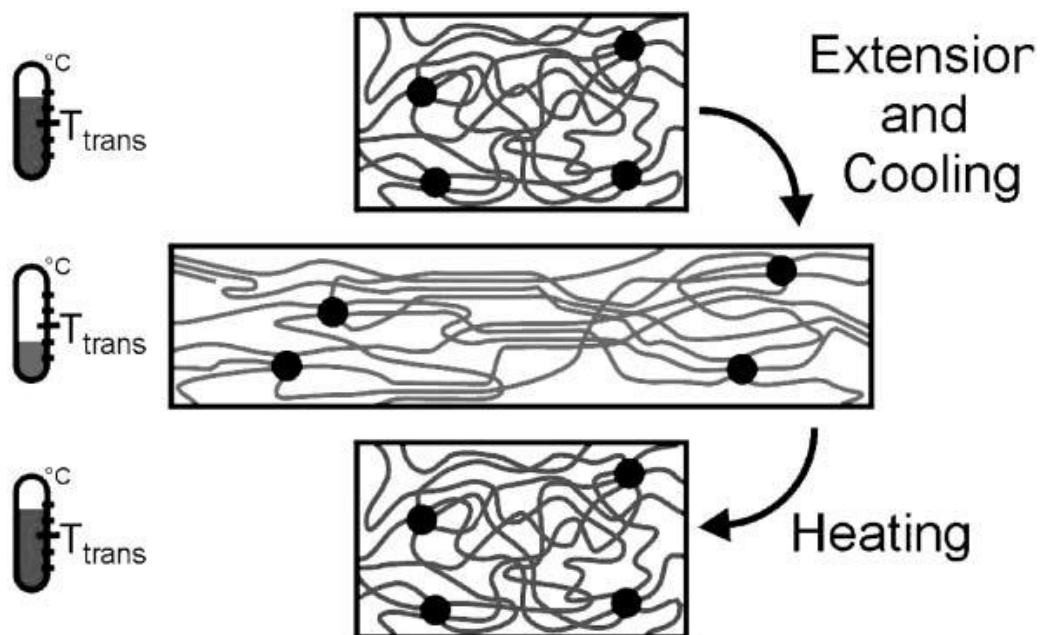


Figure 1.8. Mechanism of the thermally induced shape memory effect. T_{trans} = thermal transition temperature related to the switching phase.

1.3. Theoretical background

1.3.1. Conduction

Conduction heat transfer is given by Fourier's law as shown below.

$$q = -KA \frac{\partial T}{\partial X} \quad (1.4)$$

where K is the thermal conductivity, q is the heat flux, A is the unit area, and $\partial T/\partial X$ is temperature gradient. Considering the structure of foam material, it is necessary to verify the effective thermal conductivity, K , of the foam material from the porosity of foam and thermal conductivities of polymer and gas in order to apply Fourier's law to the foam material. However, the predictive value of the effective thermal conductivity can be changed with the modelling method due to the complexation of foam microstructure. In this study, the foam structure was modelled to the formation of cells which resemble regular pentagonal dodecahedrons as shown in figure 1.9. We should consider the level of contribution of strut and wall to predict more correctly because medium conductivity is increased linearly with volume fraction of the solid. Hence, the upper limit model of the conduction heat transfer through real foam is suggested as below [56, 59].

$$K = K_g + \left(\frac{2}{3} - \frac{f_s}{3} \right) (1 - V_g) K_s \quad (1.5)$$

By considering the difference between the in-line and the staggered lower limits for cubical bubbles, the lower limit equation for real foam is also given to estimate the error as shown below [60].

$$K = K_g + 0.8 \left(\frac{2}{3} - \frac{f_s}{3} \right) (1 - V_g) K_s \quad (1.6)$$

An average cell diameter ϕ_c and a mean wall thickness δ can be derived from scanning electron microscope (SEM) pictures considering orientation effects. These data allow one to determine the mass fraction $m_s / (m_w + m_s)$ and $m_w / (m_w + m_s)$ of struts and walls, respectively. The following equations containing the geometrical proportions of the dodecahedron are then used [61, 62].

$$\frac{m_s}{\rho_s} = 2.8\phi_c\phi_s^2 - 3.9\phi_s^3 \quad (1.7)$$

$$\frac{m_w}{\rho_s} = [1.3\phi_c^2 - 5.4\phi_c\phi_s + 1.7\phi_s^2] \delta \quad (1.8)$$

where ρ_s is the density of the bulk material. Typically, the mass fraction of the struts is obtained by using the following equation [61, 62].

$$f_s = \frac{m_s}{m_w + m_s} \approx 0.6 \sim 0.9 \quad (1.9)$$

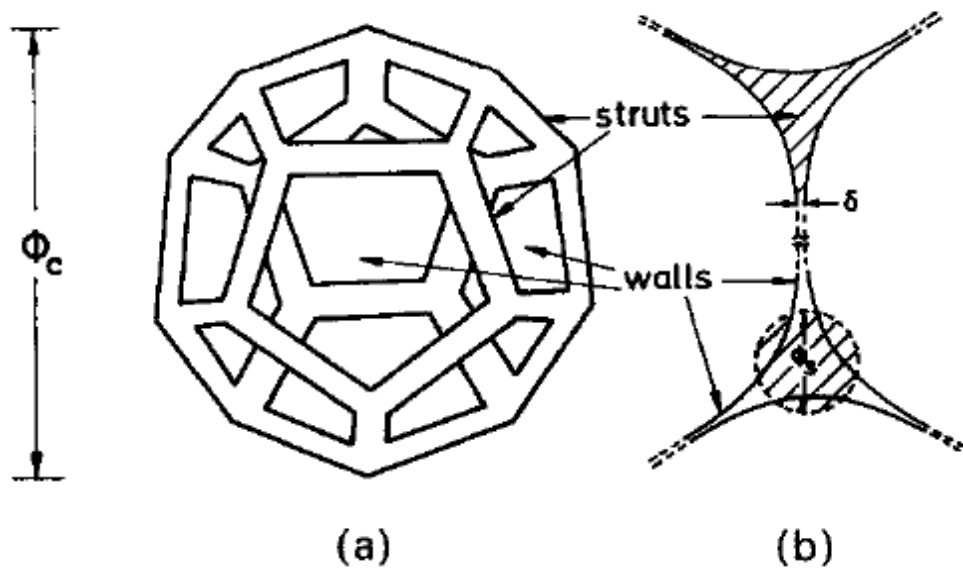


Figure 1.9. Dodecaeder model for a foam cell. (a) Perspective view. (b) Cross-section through struts and walls.

1.3.2. Radiation

In general, the relation between temperature and heat generated by radiation is given by Stefan-Boltzmann equation shown below.

$$q = \varepsilon \sigma AT^4 \quad (1.10)$$

where σ is Stefan-Boltzmann constant, ε is emissivity, A is radiation area, and T is temperature. Radiation heat transfer in the foam material is more complex and difficult to analyze than conduction heat transfer in the foam material because radiation energy can be decreased with absorption and scattering by the strut of the foam structure. Because of these reasons, the radiation heat transfer can be estimated by using the experimental data. Among several methods, Rosseland's radiation theory based on the experimental data is the most reasonable equation. Radiation heat transfer of the foam material can be predicted by using extinction coefficient obtained from experiment [63, 64].

$$q_r = -\frac{16\sigma T^3}{3K_R} \frac{dT}{dx} \quad (1.11)$$

where subscript R means average value of Rosseland which is calculated according to wavelength. However, there are various methods to estimate K_R and it is difficult to obtain the experimental extinction coefficient. Therefore, the following simple equation is suggested by assuming that layers of gas and solid are parallel to each other and wall is transparent and strut is opaque, thereby the decrease of radiation heat transfer by scattering is neglected [65].

$$K_r = \frac{4\sigma\varepsilon LT^3}{2-\varepsilon} \quad (1.12)$$

where L is thickness of gas layer which means the cell size. This equation indicates the relationship between the thermal conductivity caused by radiation and the cell size of the foam material. To predict more accurately the thermal conductivity caused by radiation, the correction factor based on experiment is utilized to compensate equation 1.12.

$$K_r = k \frac{4\sigma\epsilon LT^3}{2 - \epsilon} \quad (1.13)$$

where k is correction factor which is obtained through experiment of this research. The theoretical thermal conductivity by radiation is regarded by subtracting theoretical thermal conductivity by conduction from overall experimental thermal conductivity of foam material because the predicted thermal conductivity by conduction is quite accurate. The correction factor, k , is determined to be 3.7 in this study.

1.3.3. Heat transfer in foam material

The thermal conductivity of foam materials is explained by four different mechanisms: conduction through the gas phase (K_g), conduction along the cell walls and struts of the solid polymer (K_s), convection within the cells (K_c), and thermal radiation (K_r). The total heat transfer can be predicted as the sum of the heat transfer by the four mechanisms considered separately. It is widely accepted that convection plays a minor role in heat transfer in cell material provided the cells are less than 1.5 mm in diameter [66, 67]. Therefore, in this study, the convective heat transfer is assumed to be negligible because of the reduced volume of the cells, which is lower than the limit set above. The contribution from thermal radiation to the effective thermal conductivity of polymer foams is not negligible. For example, it was reported that as much as 7 ~ 25 % of thermal conductance in polystyrene was through radiative heat transfer [68, 69]. For foams with the same density, heat radiation can be reduced by decreasing cell size or increasing radiation absorption through the addition of infrared light absorbing fillers such as carbon nanotubes and graphene [70-73]. As a result, the thermal conductivity can be expressed as below.

$$K = K_g + \left(\frac{2}{3} - \frac{f_s}{3} \right) (1 - V_g) K_s + k \frac{4\sigma\epsilon L T^3}{2 - \epsilon} \quad (1.14)$$

1.4. Objectives of Present Work

The main objectives of this study are to investigate the heat transfer phenomena in micro/nano structures and to control the thermal properties of polymer composites. This study includes several processing techniques, relationships between fundamental structure and properties, experimental and numerical results of physical behavior, and application to polymer nanocomposite and foam material.

The effects of the surface area, internal structure, and content of fillers on the thermal behavior of silica aerogel composites are investigated in chapter 2. The morphological properties of silica aerogel composites are observed to identify the influence of internal structure. For the intensive study, a new processing method for preserving pores of silica aerogel in composites is demonstrated.

In chapter 3, thermal and mechanical properties of the shape memory polyurethane (SMPU) foam are characterized to investigate the pore size effect of the SMPU foam. The thermal conductivities of the SMPU foam materials are also measured according to the shape of SMPU foam such as original, compressed, and recovered shape. For more detailed investigation, the thermal conductivities of the SMPU foam materials are modelled theoretically. Three dimensional mechanical analysis is also performed to investigate the synergistic effect according to composition of pore size in SMPU foam materials by using a commercial numerical analysis.

The effect of the surface structure on the thermal properties of graphene/PET film coated with zinc oxide (ZnO) nanorods are investigated in chapter 4. The distribution state of ZnO nanorods is very important factor in determining thermal dissipation properties of the ZnO/graphene/PET film system. Moreover, the growth mechanism of ZnO nanostructures is analyzed by modified classical nucleation theory. The numerical results are compared with the experimental results.

1.5. References

- [1] Fricke J. Aerogels—highly tenuous solids with fascinating properties. *Journal of non-Crystalline solids* 1988, 100, 169-173.
- [2] Hrubesh L, Poco J. Thin aerogel films for optical, thermal, acoustic and electronic applications. *Journal of non-crystalline solids* 1995, 188, 46-53.
- [3] Fricke J, Tillotson T. Aerogels: production, characterization, and applications. *Thin Solid Films* 1997, 297, 212-223.
- [4] Fricke J. Aerogels. *Scientific American* 1988, 258, 92-97.
- [5] Hüsing N, Schubert U. Aerogels—airy materials: chemistry, structure, and properties. *Angewandte Chemie International Edition* 1998, 37, 22-45.
- [6] Kistler S. Coherent Expanded Aerogels and Jellies. *Nature* 1931, 127, 741.
- [7] Kistler S. Coherent expanded-aerogels. *The Journal of Physical Chemistry* 1932, 36, 52-64.
- [8] Teichner S, Nicolaon G, Vicarini M, Gardes G. Inorganic oxide aerogels. *Advances in Colloid and Interface Science* 1976, 5, 245-273.
- [9] Tewari P, Hunt A, Lieber J, Lofftus K. Microstructural properties of transparent silica aerogels. In *Aerogels*. Springer, 1986, 142-147.
- [10] Tillotson T, Hrubesh L. Transparent ultralow-density silica aerogels prepared by a two-step sol-gel process. *Journal of Non-Crystalline Solids* 1992, 145, 44-50.
- [11] Fricke J, Emmerling A. Aerogels—recent progress in production techniques and novel applications. *Journal of Sol-Gel Science and Technology* 1998, 13, 299-303.
- [12] Prakash S, Brinker C, Hurd A, Rao S. Ambient-pressure silica aerogel films. In *MRS Proceedings*; Cambridge Univ Press, 1994, 205.
- [13] Hrubesh L, Pekala R. Dielectric properties and electronic applications of aerogels. In *Sol-Gel Processing and Applications*. Springer, 1994, 363-367.
- [14] Nilsson O, Fransson Å, Sandberg O. Thermal Properties of Silica Aerogel. In *Aerogels*. Springer, 1986, 121-126.
- [15] Pekala R, Farmer J, Alviso C, Tran T, Mayer S, Miller J, Dunn B. Carbon aerogels for electrochemical applications. *Journal of non-crystalline solids* 1998, 225, 74-80.

- [16] Farmer J, Fix D, Mack G, Pekala R, Poco J. Capacitive deionization of NaCl and NaNO₃ solutions with carbon aerogel electrodes. *Journal of the Electrochemical Society* 1996, 143, 159-169.
- [17] Tsou P. Silica aerogel captures cosmic dust intact. *Journal of Non-Crystalline Solids* 1995, 186, 415-427.
- [18] Hrubesh L. Aerogel applications. *Journal of Non-Crystalline Solids* 1998, 225, 335-342.
- [19] Hunt A. Light scattering studies of silica aerogels. Lawrence Berkeley National Laboratory 2010.
- [20] Wang P, Körner W, Emmerling A, Beck A, Kuhn J, Fricke J. Optical investigations of silica aerogels. *Journal of non-crystalline solids* 1992, 145, 141-145.
- [21] Hornfeck M, Theiss W, Clasen R. IR spectroscopy of porous silica gels. *Journal of non-crystalline solids* 1992, 145, 154-158.
- [22] Fricke J. Thermal transport in porous superinsulations. In *Aerogels*. Springer, 1986, 94-103.
- [23] Wittwer V. Development of aerogel windows. *Journal of Non-Crystalline Solids* 1992, 145, 233-236.
- [24] Zobel W, Strahle R. Heat Storage Battery for Car Applications. In *Proceedings Vehicle Thermal Management Systems Conference*, 1995, 379-385.
- [25] Hyun S. H, Kim J. J, Park H. H. Synthesis and Characterization of Low-Dielectric Silica Aerogel Films. *Journal of the American Ceramic Society* 2000, 83, 533-540.
- [26] Jo M. H, Park H. H, Kim D. J, Hyun S. H, Choi S. Y, Paik J. T. SiO₂ aerogel film as a novel intermetal dielectric. *Journal of applied physics* 1997, 82, 1299-1304.
- [27] Paik J. A, Dunn B. MEMS with thin-film aerogel. 2001.
- [28] Iijima S. Helical microtubules of graphitic carbon. *nature* 1991, 354, 56-58.
- [29] McEuen P, Bockrath M, Cobden D, Yoon Y. G, Louie S. Disorder, pseudospins, and backscattering in carbon nanotubes. *Physical Review Letters* 1999, 83, 5098.
- [30] Uchida T, Kumar S. Single wall carbon nanotube dispersion and exfoliation in polymers. *Journal of applied polymer science* 2005, 98, 985-989.
- [31] Berber S, Kwon Y. K, Tomanek D. Unusually high thermal conductivity of carbon

- nanotubes. *Physical review letters* 2000, 84, 4613.
- [32] Moniruzzaman M, Winey K. Polymer nanocomposites containing carbon nanotubes. *Macromolecules* 2006, 39, 5194-5205.
- [33] Zhao J, Park H, Han J, Lu J. Electronic properties of carbon nanotubes with covalent sidewall functionalization. *The Journal of Physical Chemistry B* 2004, 108, 4227-4230.
- [34] Mylvaganam K, Zhang L. Nanotube functionalization and polymer grafting: an ab initio study. *The Journal of Physical Chemistry B* 2004, 108, 15009-15012.
- [35] Thostenson E, Ren Z, Chou T. W. Advances in the science and technology of carbon nanotubes and their composites: a review. *Composites science and technology* 2001, 61, 1899-1912.
- [36] Reich, S, Thomsen C, Maultzsch J. Carbon nanotubes: basic concepts and physical properties; John Wiley & Sons, 2008.
- [37] Bhattacharyya S, Kymakis E, Amaratunga G. Photovoltaic properties of dye functionalized single-wall carbon nanotube/conjugated polymer devices. *Chemistry of materials* 2004, 16, 4819-4823.
- [38] Zurutuza A, Marinelli C. Challenges and opportunities in graphene commercialization. *Nature nanotechnology* 2014, 9, 730-734.
- [39] Gomez De Arco L, Zhang Y, Schlenker C, Ryu K, Thompson M, Zhou C. Continuous, highly flexible, and transparent graphene films by chemical vapor deposition for organic photovoltaics. *ACS nano* 2010, 4, 2865-2873.
- [40] Reina A, Jia X, Ho J, Nezich D, Son H, Bulovic V, Dresselhaus M, Kong J. Large area, few-layer graphene films on arbitrary substrates by chemical vapor deposition. *Nano letters* 2008, 9, 30-35.
- [41] Lee W. H, Park J, Sim S. H, Lim S, Kim K. S, Hong B. H, Cho K. Surface-directed molecular assembly of pentacene on monolayer graphene for high-performance organic transistors. *Journal of the American Chemical Society* 2011, 133, 4447-4454.
- [42] Cheng Z, Zhou Q, Wang C, Li Q, Wang C, Fang Y. Toward intrinsic graphene surfaces: a systematic study on thermal annealing and wet-chemical treatment of SiO₂-

- supported graphene devices. *Nano letters* 2011, 11, 767-771.
- [43] Kim K. S, Zhao Y, Jang H, Lee S. Y, Kim J. M, Kim K. S, Ahn J. H, Kim P, Choi J. Y, Hong B. H. Large-scale pattern growth of graphene films for stretchable transparent electrodes. *Nature* 2009, 457, 706-710.
- [44] Li X, Magnuson C, Venugopal A, Tromp R, Hannon J, Vogel E, Colombo L, Ruoff R. Large-area graphene single crystals grown by low-pressure chemical vapor deposition of methane on copper. *Journal of the American Chemical Society* 2011, 133, 2816-2819.
- [45] Li X, Cai W, An J, Kim S, Nah J, Yang D, Piner R, Velamakanni A, Jung I, Tutuc E. Large-area synthesis of high-quality and uniform graphene films on copper foils. *Science* 2009, 324, 1312-1314.
- [46] Bae S, Kim H, Lee Y, Xu X, Park J. S, Zheng Y, Balakrishnan J, Lei T, Kim H. R, Song Y. I. Roll-to-roll production of 30-inch graphene films for transparent electrodes. *Nature nanotechnology* 2010, 5, 574-578.
- [47] Wang Z. Zinc oxide nanostructures: growth, properties and applications. *Journal of Physics: Condensed Matter* 2004, 16, R829.
- [48] Klabunde K, Richards R. *Nanoscale materials in chemistry*. Wiley Online Library 2001.
- [49] Jeon H. G, Mather P. T, Haddad T. Shape memory and nanostructure in poly (norbornyl-POSS) copolymers. *Polymer International* 2000, 49, 453-457.
- [50] Kim B. K, Lee S. Y, Xu M. Polyurethanes having shape memory effects. *Polymer* 1996, 37, 5781-5793.
- [51] Behl M, Lendlein A. Actively moving polymers. *Soft Matter* 2007, 3, 58-67.
- [52] Lendlein A, Kelch S. Shape-memory polymers. *Angewandte Chemie International Edition* 2002, 41, 2034-2057.
- [53] Hu J, Zhu Y, Huang H, Lu J. Recent advances in shape-memory polymers: Structure, mechanism, functionality, modeling and applications. *Progress in Polymer Science* 2012, 37, 1720-1763.
- [54] Szycher M. *Szycher's handbook of polyurethanes*. CRC press 1999.
- [55] Koo M. S, Chung K, Youn J. R. Reaction injection molding of polyurethane foam

- for improved thermal insulation. *Polymer Engineering & Science* 2001, 41, 1177-1186.
- [56] Thirumal M, Khastgir D, Singha N, Manjunath B, Naik Y. Effect of foam density on the properties of water blown rigid polyurethane foam. *Journal of applied polymer science* 2008, 108, 1810-1817.
- [57] Agrawal C, Ray R. Biodegradable polymeric scaffolds for musculoskeletal tissue engineering. *Journal of biomedical materials research* 2001, 55, 141-150.
- [58] Mooney D, Baldwin D, Suh N. P, Vacanti J, Langer R. Novel approach to fabricate porous sponges of poly (D, L-lactic-co-glycolic acid) without the use of organic solvents. *Biomaterials* 1996, 17, 1417-1422.
- [59] Progelhof R, Throne J, Ruetsch R. Methods for predicting the thermal conductivity of composite systems: a review. *Polymer Engineering & Science* 1976, 16, 615-625.
- [60] Skochdopole R. The thermal conductivity of foamed plastics. *Chem. Eng. Prog* 1961, 57, 55-59.
- [61] Kuhn J, Ebert H, Arduini-Schuster M, Büttner D, Fricke J. Thermal transport in polystyrene and polyurethane foam insulations. *International journal of heat and mass transfer* 1992, 35, 1795-1801.
- [62] Schuetz M, Glicksman L. A basic study of heat transfer through foam insulation. *Journal of Cellular Plastics* 1984, 20, 114-121.
- [63] Glicksman L, Schuetz M, Sinofsky M. Radiation heat transfer in foam insulation. *International journal of heat and mass transfer* 1987, 30, 187-197.
- [64] 장민석, 폴리우레탄포움의 구조적 변화에 따른 열전도도의 예측. 서울대학교 대학원, 1998.
- [65] Jones, T. The effect of thickness and temperature on heat transfer through foamed polymers. 1968.
- [66] Modesti M, Dall'Acqua C, Lorenzetti A, Florian E. Mathematical model and experimental validation of water cluster influence upon vapour permeation through hydrophilic dense membrane. *Journal of membrane science* 2004, 229, 211-223.
- [67] Holman J. *Heat Transfer of International Edition*. McGraw-Hill, New York, 2009.
- [68] Glicksman L, Torpey M. The influence of cell size and foam density on the

thermal conductivity of foam insulation. In Polyurethanes World Congress, Germany, 1987, 80-84.

[69] Williams R, Aldao C. Thermal conductivity of plastic foams. *Polymer Engineering & Science* 1983, 23, 293-298.

[70] Loeb A. Thermal conductivity: VIII, a theory of thermal conductivity of porous materials. *Journal of the American Ceramic Society* 1954, 37, 96-99.

[71] Almanza O, Rodríguez-Pérez M, De Saja J. Prediction of the radiation term in the thermal conductivity of crosslinked closed cell polyolefin foams. *Journal of Polymer Science Part B: Polymer Physics* 2000, 38, 993-1004.

[72] Kompan M, Kompan F, Gladkikh P, Terukov E, Rupyshev V, Chetaev Y. Thermal conductivity of a composite medium with a disperse graphene filler. *Technical Physics* 2011, 56, 1074-1078.

[73] Chen L, Rende D, Schadler L, Ozisik R. Polymer nanocomposite foams. *Journal of Materials Chemistry A* 2013, 1, 3837-3850.

II. Aerogel Composite

2.1. Silica aerogel/epoxy composites with preserved aerogel pores and low thermal conductivity

2.1.1. Introduction

Interests on insulating materials have increased in recent years since effective insulating materials play a key role in energy savings and efforts to address worldwide problems of global warming, oil price inflation, and carbon dioxide production. Among insulating materials, aerogels have the lowest documented thermal conductivity and thus show great promise for applications. An aerogel is a dried gel with a very high porosity [1] and was discovered in the early 1930s by Kistler [2]. Silica aerogels were initially synthesized by traditional low-temperature, sol-gel chemistry [3, 4], but little further development was achieved for several decades. Silica aerogels have received significant attention in the last two decades due to their commercial potential.

A silica aerogel is composed of nanosized (1 ~ 100 nm) particles with an open cell structure and has a high specific surface area (500 ~ 1200 m²/g), low density (0.003 ~ 0.1 g/cm³), low dielectric constant (1.1 ~ 2.0), and low thermal conductivity (0.013 ~ 0.14 W/m·K) [5-8]. The excellent adiabatic capabilities of silica aerogels suggest that they have very high potential for applications in thermal, acoustic and electronic fields, particularly for thermal insulation applications such as the heat protection of space shuttles, nuclear reactors, and ordinary steam pipes [9-14]. However, silica aerogels are limited in their applications as an insulation material because they are brittle and fragile under relatively low external stresses, and the fabrication of aerogel products is complicated due to the high porosity of the aerogel.

There are two main research issues for silica aerogels. The first is the development of more durable silica aerogels with higher strength and stiffness. Randall et al. have contributed to this topic extensively by investigating silane precursors and reinforcement with polymers, as summarized in a review article [15]. The other one is the manufacture of inexpensive silica aerogels and silica aerogel composites for a potential market of such materials as composite parts, fibers, and textiles. Since the silica aerogel is expensive due to the high cost of the raw materials and the long drying process with super critical fluids, an appropriate processing method is required to fabricate a polymer composite based on an inexpensive powder form of silica aerogels produced by using water glass and ambient drying conditions [8]. A polymer binding system for silica aerogels was proposed by Schmidt and Schwertfeger, and a material system utilizing both a thermoplastic polymer and a wet solution has been demonstrated to be a good binder for silica aerogel [16]. The effects of wet, dry, and dual mixing on the thermal conductivity of aerogel/polyvinylbutyral(PVB) composites have been investigated, and dry mixing was shown to be more suitable than other methods [17]. A thermosetting polymer has been applied to aerogel composites to improve the service temperature of the composites [18]. A liquid epoxy has been used as the polymer matrix to prepare the aerogel/epoxy composite by wet mixing [19, 20], but the thermal insulation properties were not satisfactory [20].

In this study, silica aerogel powder/epoxy composites were prepared with varying volume fractions of the aerogel. The thermal conductivities of the composites were measured with a heat flow meter to evaluate the insulating ability of the composites. The thermal conductivity of the epoxy composites filled with plasma treated aerogels was also measured to investigate the relationship between the internal structure of the aerogel and the thermal conductivity of the composites. To prevent filling of the aerogel pores with the epoxy matrix, a preparation method for preserving the aerogel pores in the final composite was developed using ethanol evaporation.

2.1.2. Experimental Section

2.1.2.1. Material

The silica aerogel powder was supplied by EM-POWER Co., Ltd. (Asan-si, Korea), and the procedure for synthesizing the silica aerogel is briefly summarized below. Water glass was used as the starting material, and silica sol with a silica content of 29 wt% was prepared using distilled water. For surface modification and gelation, the co-precursor method was used, in which hexamethyldisilazane and nitric acid were added to the silica sol. The hydrogel obtained by the co-precursor method was immersed in n-hexane at 60 °C for 10 h to exchange the solvent and remove ions, including sodium. The modified gel was sequentially dried at 170 °C for 20 min and 200 °C for 10 min at ambient pressure. Properties of the supplied aerogel, which were related to the thermal conductivity of the composites based on the polymer matrix, are listed below. The thermal conductivity, stable temperature, density, pore volume, and porosity of the silica aerogels were 0.02 W/m·K, -200 °C ~ 450 °C, 0.05 g/cm³, 35 ml/g, and 90 %, respectively. As shown in figure 2.1.1, 95 % of the aerogel particles had a size between 1 and 10 μm. The pore sizes of the aerogels were smaller than 20 nm, and the average pore size was approximately 9 nm [21].

2.1.2.2. Preparation of silica aerogel powder/epoxy composites

Pristine silica aerogel powder was treated with plasma (Model BD-10AV, Electro-Technic Products Inc., USA) for 30 s to alter the structure of the aerogel, such as particle size and surface area, and to investigate the effects of the altered aerogel structure on the thermal conductivity of the silica aerogel powder/epoxy composites. The epoxy resin (YD-128) and hardener (IPDA), i.e., the diglycidyl ether of Ltd. (Seoul, Korea). The silica aerogel powder/epoxy composites were prepared by mixing the aerogels with the epoxy mixture for 30 min, i.e., the epoxy resin and hardener were mixed with respect to the volume fraction of the aerogel and the aerogel type such

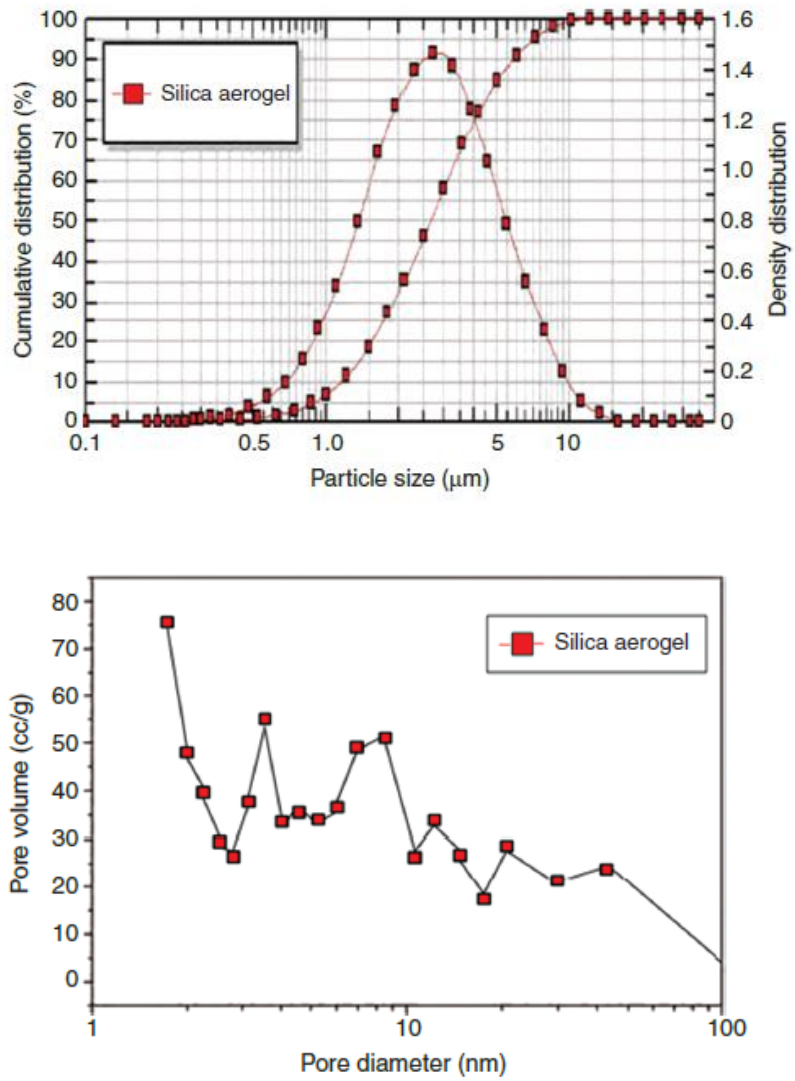


Figure 2.1.1. Particle and pore size distribution of the as-received aerogel.

bisphenol-A and the modified aromatic amine, were supplied by Kukdo Chemical Co., as as-received and plasma-treated aerogels. Before the hardening of the composites, the specimens were molded for characterization by pressing the mixture at 20 °C under 1.5 MPa for 5 h. A preparation method for the silica aerogel powder/epoxy composite was developed to preserve the pores in the aerogel, as shown in figure 2.1.2. The silica aerogels were immersed in ethanol to fill the pores of the aerogel with ethanol. A silica aerogel powder/epoxy composite with high porosity was prepared by mixing the aerogel/ethanol mixture, epoxy resin, and hardener, and then pressing the specimen at 80 °C under 1 MPa for 5 h to remove the ethanol from the pores of the aerogel before the hardening of the composite.

2.1.2.3. Measurement of thermal conductivity

The thermal conductivity of the prepared composite specimen was measured with a thermal analyzer (Thermo Labo II-KES-F7, KATO TECH Co., Tokyo, Japan) that functions as a heat flow meter. The thermal conductivity was calculated using the following equation.

$$k = \frac{W \times D}{A \times \Delta T} \quad (2.1.1)$$

where W is the heat flow in watts, D is the thickness of the sample in meters, ΔT is the temperature difference between the hot and the cold plates in Celsius (°C), and A is the surface area of the hot plate ($25 \times 10^{-4} \text{ m}^2$).

2.1.2.4. Morphology of silica aerogel powder/epoxy composite

The as-received and plasma-treated aerogels and the fractured surfaces of the silica aerogel powder/epoxy composites were coated with platinum under vacuum for 300 s using a sputter coating machine (Cressington Scientific Instruments, UK).

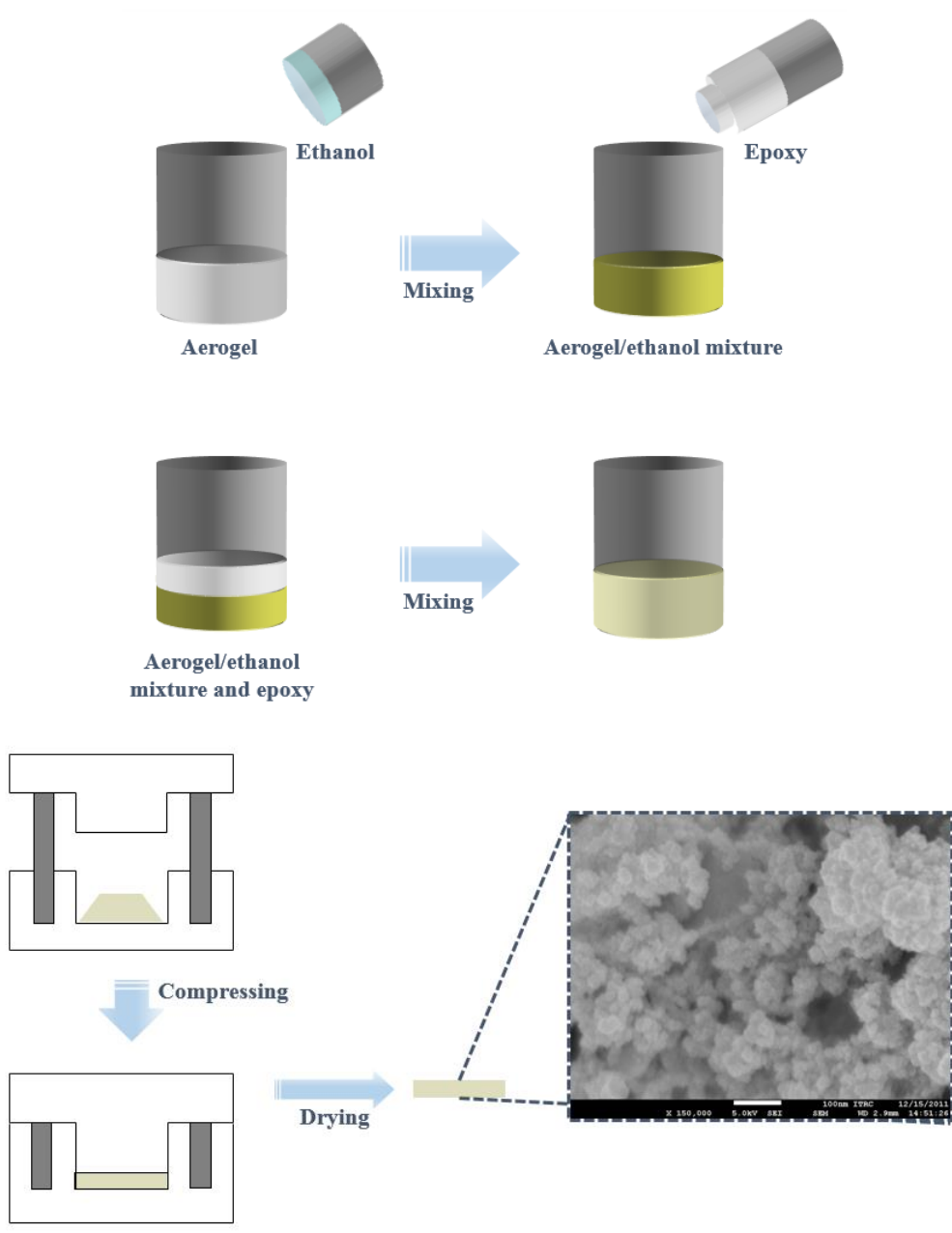


Figure 2.1.2. Schematic diagram of the processing method for preserving aerogel pores.

The morphologies of the as-received and plasma-treated aerogels and of the fractured surfaces of the silica aerogel powder/epoxy composite were observed with a field emission scanning electron microscope (FE-SEM, JSM-6390LV, JEOL, Tokyo, Japan) to investigate the internal structure of the aerogels and composites.

2.1.2.5. Pore characterization of silica aerogel and the aerogel powder/epoxy composite

The specific surface area, pore volume, and pore size of the aerogels and composites were measured by the Brunauer-Emmett-Teller method (BET method, ASSP 2010, Micromeritics, Norcross, USA). The aerogel and composite samples were heated to 150 °C and 40 °C under vacuum (10^{-5} Torr) for 2 and 24 h to remove the adsorbed species, respectively. Nitrogen adsorption data were acquired at 77 K. All nitrogen adsorption/desorption measurements were equilibrated for 10 s before being recorded.

2.1.2.6. Density of the silica aerogel powder/epoxy composite

The density of the composites was measured at 25 °C using a density-gradient column filled with carbon tetrachloride and n-heptane.

2.1.3. Results and Discussion

The thermal conductivity of the silica aerogel powder/epoxy composite is shown in figure 2.1.3 with respect to the volume fraction of the aerogel. The as-received silica aerogel powder/epoxy composite showed thermal conductivities from 0.11 to 0.12 W/m·K, while the thermal conductivities of the plasma-treated silica aerogel powder/epoxy composite were 0.09 ~ 0.11 W/m·K. The measured values were higher than expected when considering the extremely low thermal conductivity of the silica aerogel, 0.02 W/m·K.

The results were attributed to the fact that the pores of the aerogel were filled with the epoxy matrix as shown in the SEM images of the fracture surfaces of the composites (Figure 2.1.4(A)-(D)). Ge et al. [22] reported a similar phenomenon in which the pores of a silica aerogel were filled with an epoxy matrix when the composite was prepared with a silica aerogel and a liquid epoxy. No obvious trend was observed in the thermal conductivity of the composite containing the as-received or the plasma-treated aerogel as the volume fraction of the aerogel was varied from 25 to 75 vol%.

The results can be explained by the interfacial thermal resistance and the intrinsic thermal conductivity of the silica. First, it can be assumed that the composite consists of a biphasic material system of the silica structure and epoxy matrix because the pores of the aerogel in the composites were filled with the epoxy resin as discussed previously. Second, increasing the volume fraction of the aerogel must have generated both a larger amount of silica, whose intrinsic thermal conductivity is 1.3 W/m·K, and a larger interface area between the silica structure and the epoxy matrix. Third, the conflicting results may stem from the generation of a larger interface area, which causes a decrease in the thermal conductivity of the composite, and a higher volume fraction of silica, which causes an increase in the thermal conductivity of the composite. According to Pernot et al., the room temperature thermal conductivity of a single crystalline SiGe material was reduced to approximately 0.9 W/m·K by engineering a set of individual phonon-scattering nanodots at the interface [23]. Every et al. reported

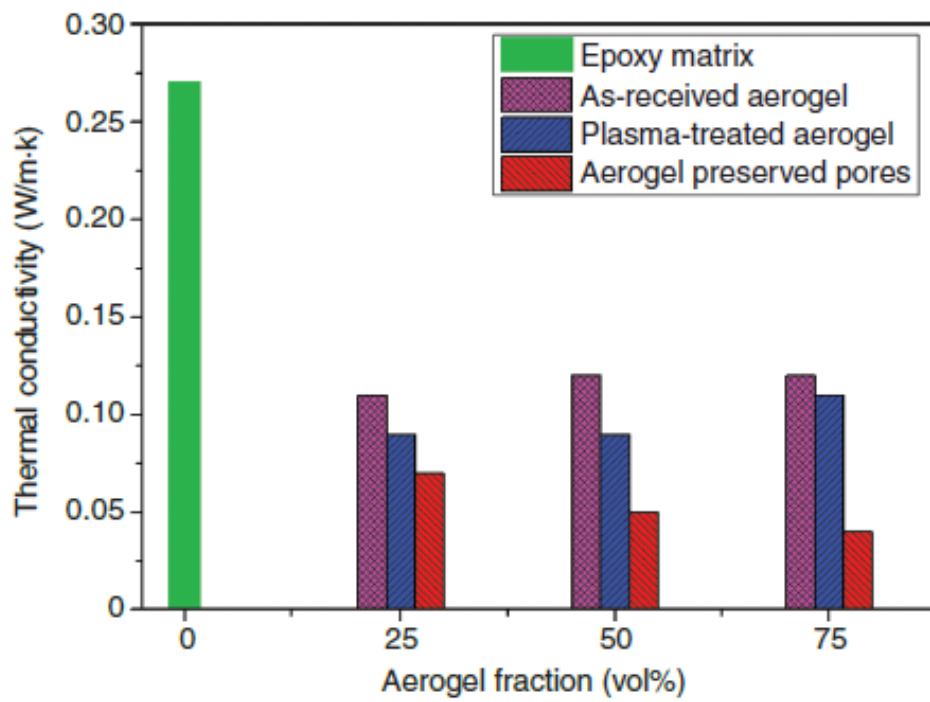


Figure 2.1.3. Thermal conductivity of the aerogel/epoxy composites with respect to the volume fraction of the aerogel.

that the thermal conductivity of zinc sulfide was lowered by the addition of sub-micron-size particles of diamond whose thermal conductivity was much higher than that of the zinc sulfide [24]. These references obviously showed the significant effect of the interfacial thermal resistance on the thermal conductivity of the composite materials.

Figure 2.1.5 shows the SEM images of the as-received and plasma-treated aerogels. The surface area of the plasma-treated aerogel is larger than that of the pristine aerogel because the size of the silica particles in the plasma-treated aerogel is smaller than that of the silica particles in the pristine aerogel.

The surface areas of the as-received and plasma-treated aerogels measured by the BET method are listed in the inserted table of figure 2.1.5. The surface areas of the as-received and plasma-treated aerogels were 614.26 and 635.45 m²/g, respectively. Despite the changed structure of the plasma-treated silica aerogel, the thermal conductivity of the composite filled with the plasma-treated aerogel was similar to that of the composite with the same volume fraction of as-received aerogel, indicating that the structure change induced by the plasma treatment does not play an important role in the thermal conductivity of the silica aerogel composites as the aerogel pores were filled with polymer matrix.

To obtain a composite with low thermal conductivity, the pores of the aerogel should be preserved in the silica aerogel powder/epoxy composite. A new method of preparing the silica aerogel powder/epoxy composite using ethanol evaporation was developed to preserve the pores in the aerogel. Details of the procedure are explained in the experimental part and shown in figure 2.1.2. According to the method, the ethanol prevents the aerogel pores from being filled by the epoxy during the mixing process and then vaporizes to restore the pores in the aerogel during the hardening process. The pores of the aerogel in the epoxy composite fabricated with the new preparation method are readily identified by the SEM images shown in figure 2.1.4(E) and (F). From the BET results listed in Table 2.1.1, the pore volume of the composites with preserved aerogel pores was increased significantly as the aerogel volume fraction in the composites was increased. Although the aerogel pores were preserved by using

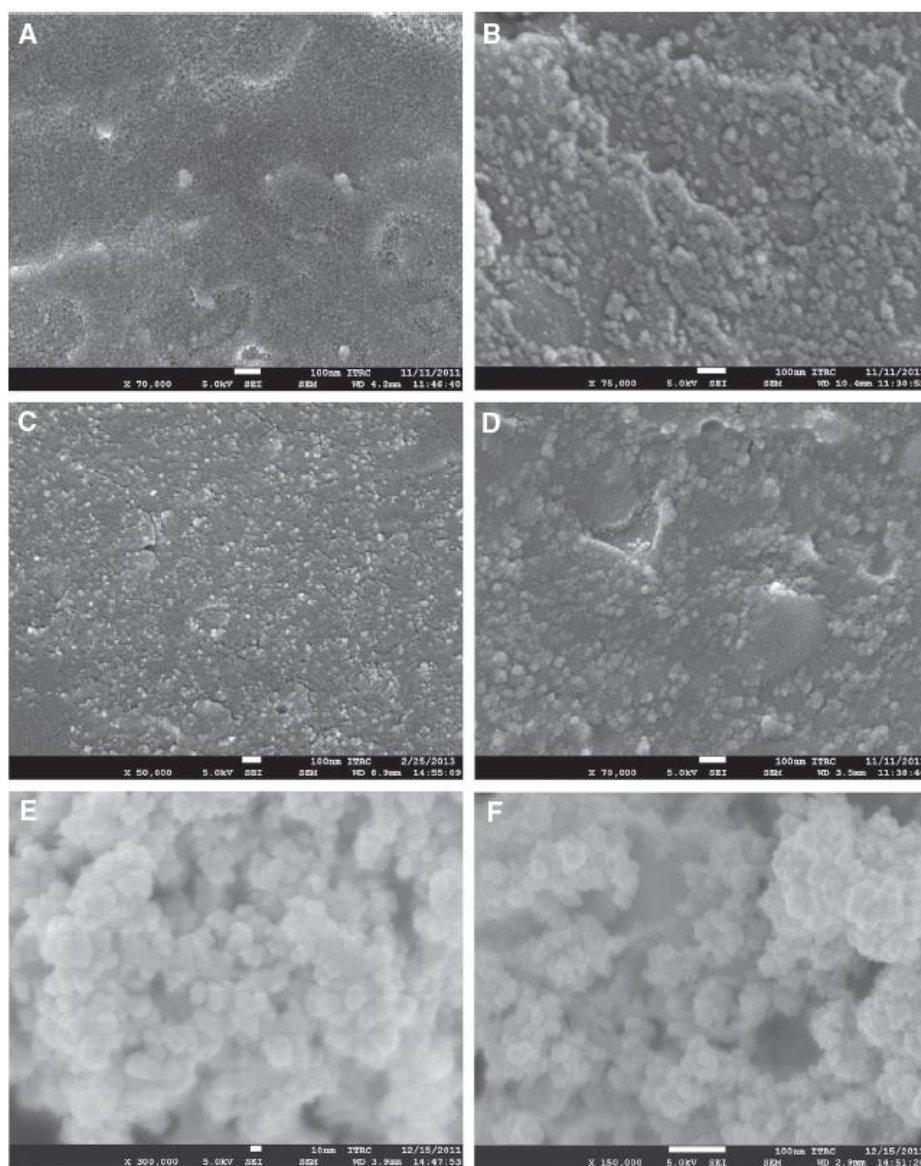


Figure 2.1.4. SEM images of the aerogel/epoxy composites with (A) as-received aerogel of 25 vol%, (B) as-received aerogel of 75 vol%, (C) plasma-treated aerogel of 25 vol%, (D) plasma-treated aerogel of 75 vol%, (E) 25 vol% preserved aerogel pores, and (F) 75 vol% preserved aerogel pores.

the proposed processing method, some parts of the aerogel pores were still impregnated by the epoxy matrix, considering the entire pore volume of the aerogel used. The thermal conductivity of the composites with preserved aerogel pores was reduced as the aerogel volume fraction was increased in the composites. The thermal conductivity of the composite containing the as-received aerogel of 75 vol% with preserved pores was 0.04 W/m K, as shown in figure 2.1.3. Therefore, preserving the aerogel pores in the composite had a great effect on the thermal conductivity of the composite.

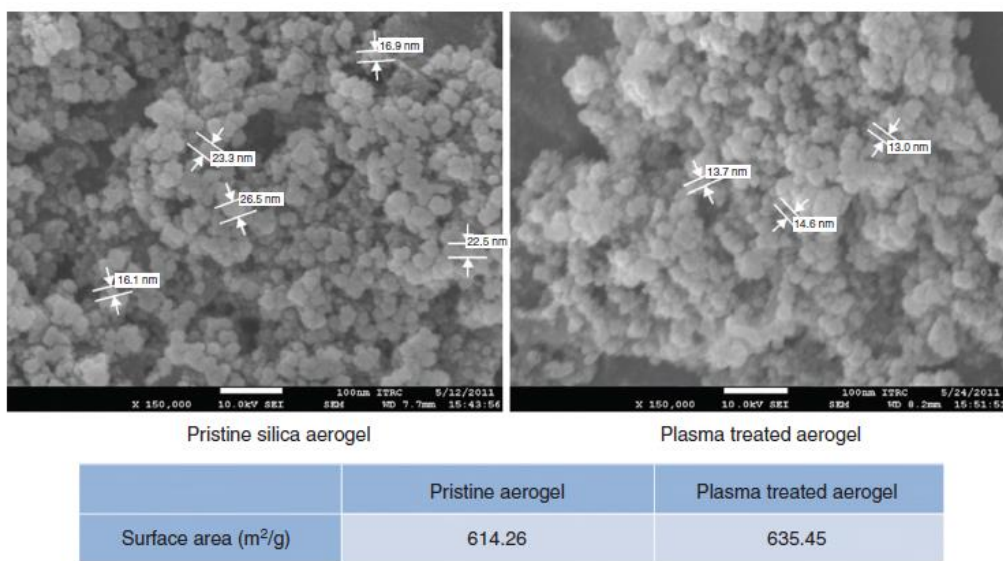


Figure 2.1.5. SEM images of pristine and plasma-treated aerogels. The white arrows indicate the particle size of the individual particles of the aerogel, and the surface of the aerogels are listed in the inserted table.

Table 2.1.1. BET results of the composites with respect to the volume fraction of the aerogel.

| | Pore volume (ml/g) | Pore size (nm) |
|------------------------|--------------------|---------------------|
| As-received | | |
| 25 vol% | 0 | – |
| 50 vol% | 0 | – |
| 75 vol% | 0 | – |
| Preserved pores | | |
| 25 vol% | 6.3 | 3–30 (average: 8.2) |
| 50 vol% | 12.5 | 3–30 (average: 8.4) |
| 75 vol% | 19.2 | 3–30 (average: 8.1) |

| | Surface area (m ² /g) | Density (g/ml) | Porosity (%) |
|------------------------|----------------------------------|----------------|--------------|
| As-received | | | |
| 25 vol% | 0 | 1.11 | 0 |
| 50 vol% | 0 | 1.11 | 0 |
| 75 vol% | 0 | 1.12 | 0 |
| Preserved pores | | | |
| 25 vol% | 122.84 | 0.91 | 18.1 |
| 50 vol% | 245.68 | 0.81 | 35.7 |
| 75 vol% | 368.52 | 0.73 | 54.8 |

2.1.4. Summary

The thermal conductivity of a silica aerogel powder/epoxy composite was investigated with respect to the volume fraction of as-received and plasma-treated aerogels. The as-received silica aerogel powder/epoxy composite displayed a range of thermal conductivity values from 0.112 to 0.123 W/m·K, while the plasma-treated silica aerogel powder/epoxy composite exhibited values from 0.085 to 0.110 W/m·K. The thermal conductivity of the silica aerogel composite was higher than expected because the pores of the as-received and plasma-treated aerogels were filled with the epoxy resin during the processing of the composites. The change in the silica aerogel structure induced by the plasma treatment, such as the size of the individual particle and surface area, did not play an important role in the thermal conductivity of the silica aerogel composites due to the impregnation of aerogel pores with polymer matrix. A preparation method for preserving the aerogel pores during the processing of the composite was proposed and developed using ethanol evaporation. The thermal conductivity of the composites with preserved aerogel pores was reduced as the aerogel volume fraction was increased in the composites, and the lowest thermal conductivity of the prepared composite containing the as-received aerogel of 75 vol% with preserved pores was 0.04 W/m·K.

2.1.5. References

- [1] Hüsing N, Schubert U. Aerogels - airy materials: chemistry, structure, and properties. *Angew Chem Int Edit* 1998, 37(1-2), 22-45.
- [2] Kistler S. Coherent expanded aerogels and jellies. *Nature* 1931, 127(3211), 741.
- [3] Zarzycki J. Past and present of sol-gel science and technology. *J Sol-Gel Sci Technol.* 1997, 8(1-3), 17-22.
- [4] Pierre A, Pajonk G. Chemistry of aerogels and their applications. *Chem Rev.* 2002, 102(11), 4243-4266.
- [5] Fricke J. Aerogels - highly tenuous solids with fascinating properties. *J Non-Cryst Solids* 1988, 100(1-3), 169-173.
- [6] Fricke J, Emmerling A. Aerogels. *J Am Ceram Soc.* 1992, 75(8), 2027-2035.
- [7] Schultz J, Jensen K, Kristiansen F. Super insulating aerogel glazing. *Sol Energy Mater Sol Cells* 2005, 89(2-3), 275-285.
- [8] Soleimani D, Abbasi M. Silica aerogel; synthesis, properties and characterization. *J Mater Process Technol.* 2008, 199(1-3), 10-26.
- [9] Moreno-Castilla C, Maldonado-Hódar F. Carbon aerogels for catalysis applications: an overview. *Carbon* 2005, 43(3), 455-465.
- [10] Tomasi R, Sireude D, Marchand R, Scudeller Y, Guillemet P. Preparation of a thermal insulating material using electrophoretic deposition of silica particles. *Mater Sci Eng B-Adv Funct Solid-State Mater.* 2007, 137(1-3), 225-231.
- [11] Fesmire J, Sass J. Aerogel insulation applications for liquid hydrogen launch vehicle tanks. *Cryogenics* 2008, 48(5-6), 223-231.
- [12] Rani T, Subha M, Venkata Reddy G, Kim Y, Ahn Y. Synthesis of water-glass-based silica aerogel powder via with and without squeezing of hydrogels. *J Appl Polym Sci.* 2010, 115(3), 1675-1679.
- [13] Baetens R, Jelle B, Gustavsen A. Aerogel insulation for building applications: a state-of-the-art review. *Energy Build.* 2011, 43(4), 761-769.
- [14] Sehaqui H, Zhou Q, Berglund LA. High-porosity aerogels of high specific surface area prepared from nanofibrillated cellulose (NFC). *Compos Sci Technol.* 2011, 71(13),

1593-1599.

[15] Randall J, Meador M, Jana S. Tailoring mechanical properties of aerogels for aerospace applications. *ACS Appl Mater Interfaces* 2011, 3(3), 613-626.

[16] Schmidt M, Schwertfeger F. Applications for silica aerogel products. *J Non-Cryst Solids* 1998, 225, 364-368.

[17] Kim G, Hyun S. Effect of mixing on thermal and mechanical properties of aerogel-PVB composites. *J Mater Sci.* 2003, 38(9), 1961-1966.

[18] Teh P, Mariatti M, Wagiman A, Beh K. Effect of curing agent on the properties of mineral silica filled epoxy composites. *Polym Compos.* 2008, 29(1), 27-36.

[19] Zhao J, Ge D, Zhang S, Wei X. Studies on thermal property of silica aerogel/epoxy composite. *Materials science forum. Switzerland: Trans Tech Publications* 2007, 1581-1584.

[20] Gupta N, Ricci W. Processing and compressive properties of aerogel/epoxy composites. *J Mater Process Technol.* 2008, 198(1-3), 178-182.

[21] Kim S. Y, Noh Y. J, Lim J, You N. H. Silica aerogel/polyimide composites with preserved aerogel pores using multi-step curing. *Macromol Res.* 2014, 22(1), 108-111.

[22] Ge D, Yang L, Li Y, Zhao J. Hydrophobic and thermal insulation properties of silica aerogel/epoxy composite. *J Non-Cryst Solids* 2009, 355(52-54), 2610-2615.

[23] Pernot G, Stoffel M, Savic I, Pezzoli F, Chen P, Savelli G, Jacquot A, Schumann J, Denker U, Mönch I, Deneke C, Schmidt O, Rampnoux J, Wang S, Plissonnier M, Rastelli A, Dilhaire S, Mingo N. Precise control of thermal conductivity at the nanoscale through individual phonon-scattering barriers. *Nat Mater.* 2010, 9(6), 491-495.

[24] Every A, Tzou Y, Hasselman D, Raj R. The effect of particle size on the thermal conductivity of ZnS/diamond composites. *Acta Mater.* 1992, 40(1), 123-129.

2.2. Silica aerogel/polyvinyl alcohol(PVA) insulation composites with preserved aerogel pores using interfaces between the superhydrophobic aerogel and hydrophilic PVA solution

2.2.1. Introduction

Aerogels are unique materials due to their distinctive three-dimensional solid structures which are mostly filled with air and they are typically classified according to their back bone materials [1-7]. Carbon aerogels are carbon based highly porous materials with excellent physical properties and are expected to be utilized in various applications such as high-temperature thermal insulators, hydrogen fuel storage devices, electric double layer capacitors and catalyst supports [1-4]. Inorganic oxide aerogels are expected to have a wide variety of applications including thermal super-insulators, adsorbents, catalyst carriers and sensors. In particular, they are promising materials for thermal insulation [5-7]. Thermal management in composites using silica has been extensively reported such as a second phase to modify the polymer matrix [8], a second filler incorporated to induce multi-functional properties of the composites [9], and a coating material for the filler to vary the surface characteristics of the filler [10], etc. Silica aerogels discovered by Kistler in the 1930s are characterized by a high specific surface area of 500 ~ 1200 m²/g, a low density of 0.003 ~ 0.1 g/cm³, a low dielectric constant of 1.1 ~ 2.0, a low thermal conductivity of 0.013 ~ 0.14 W/m·K and superhydrophobicity [11-16]. These properties of silica aerogels give them potential for commercialization in fields such as audio, electricity, and heat generation, especially as insulators for the thermal protection of steam pipes or space-crafts [17-22]. In recent years, silica aerogels have been widely studied to investigate how to make them stronger and more stable. Meador et al. reported a variety of ways in which silane precursors and polymer reinforcements can be used for such purposes [23]. More recent studies have considered how to manufacture inexpensive silica aerogels or silica aerogel composites for commercial purposes. Schmidt and Schwertfeger proposed a silica aerogel/polymer binding system and found that thermoplastic polymers and wet

solutions are better binders for silica aerogels [24]. The effects of wet, dry and dual mixing processes on the thermal conductivity of aerogel/polyvinylbutyral composites were investigated and it was reported that dry mixing was more appropriate than other techniques for the insulation performance of composites [25]. In another report, thermosetting polymers were used in an attempt to raise the service temperature of aerogel composites [26]. Aerogel/epoxy composites were prepared by a wet mixing technique using a liquid epoxy resin, but their insulation performance was not good [27, 28]. Most recently, Kim et al. developed a process of preparing polyimide composites with preserved pores in silica aerogels through multi-step curing and reported excellent thermal insulation of the polyimide composites [29]. Polyamic acid which is a polyimide precursor and silica aerogel powders prepared by using relatively inexpensive water glass and ambient drying process were used as the raw material. The polyamic acid solution filled with the silica aerogel powder was converted to a polyimide composite with preserved pores in silica aerogel as the polyamic acid was cured and the solvent was vaporized during the multi-step curing. From the above reports, it is clear that the excellent insulation performance of aerogel/polymer composites can be achieved when the pores of the aerogel are well preserved. Silica aerogel/polymer composites will have better insulation properties when aerogel pores are not impregnated with polymer resin from the beginning of the fabrication process than when the pores are filled with other materials or are ultimately restored during the process. Therefore, superhydrophobicity of the aerogel was utilized in this study. The simultaneous use of hydrophobic silica aerogels and hydrophilic polymers or solvents can result in immiscibility or phase separation, and the subsequent forced fabrication can induce the preservation of pores in the aerogels. As shown in figure 2.2.1, interfaces were formed in this study between the silica aerogels and the hydrophilic polyvinylalcohol (PVA) solution and then the silica aerogel/PVA composites were fabricated while precipitating PVA over the interface by making the solvent vaporize at a slow rate during stirring. The Thermal properties of the aerogel composites were examined with respect to the PVA concentration in solution and the process temperature which were recognized as most important processing parameters.

2.2.2. Experimental Section

2.2.1. Silica aerogel

Silica aerogel powder was supplied by EM-POWER Co., Ltd(Asan-si, Korea). The synthesis method of the silica aerogel is presented in figure S2.2.1. Table 2.2.1 shows the physical properties of the aerogel and the resins related to the thermal performance of silica aerogel composites [30].

2.2.2. Preparation of silica aerogel/PVA composites

PVA powder supplied by Daejung Chemicals Co., Ltd.(Siheung-si, Korea) was dissolved in deionized (DI) water at 60 °C, and PVA solutions were prepared according to PVA contents (i.e. 3, 5, 10 and 20 wt%). When the silica aerogel powder is added to the PVA solution at a volume ratio of 1:1, the aerogel and PVA solution separated into two layers because of their different chemical natures, as can be seen in figure 2.2.1. To produce the silica aerogel/PVA composites, the PVA solutions and silica aerogel powders which were separated by an interface in the beakers were stirred for 48 h at 300 rpm while being heated to 20, 40, 60 or 80 °C on a hot plate. Scale-up of the proposed processing can be possible by selecting an appropriate stirring method because the interfaces between the silica aerogel powder and PVA solution can be generated irrespective of the utilized amount of raw materials as shown in figure S2.2.2.

2.2.3. Preparation of silica aerogel/epoxy composites

Epoxy resin (YD 128), diglycidyl ether of bisphenol-A, and a hardening agent (IPDA), modified aromatic amine, were obtained from Kukdo Chemical Co., Ltd. (Seoul, Korea). Silica aerogel powders were immersed in an epoxy mixture prepared by mixing the epoxy resin and the hardener at a ratio of 1:1. The mixture of silica aerogel/epoxy resin was used to prepare specimens of the silica aerogel/epoxy

composite according to the volume fraction of the aerogels. The composite samples were pressed for 5 h under a pressure of 1.5 MPa at 20 °C for hardening of the composite.

2.2.4. Measurement of thermal conductivity

Thermal conductivity of the composite specimen was measured by using a thermal conductivity measurement instrument (C-Therm TCi, C-Therm Technologies Ltd., New Brunswick, Canada) based on the modified transient plane source method. When an electric current is applied to the heating part of a sensor to generate a small amount of heat, the generated heat causes a temperature rise of approximately 2 °C at the interface between the sensor and the composite. The temperature rise at the interface causes a voltage drop in the sensor element. The thermal conductivity was determined by measuring the rate of increase in sensor voltage and the test was conducted at room temperature.

2.2.5. Morphology of the composite

The surfaces of aerogel/epoxy and aerogel/PVA composite specimens were coated with platinum for 300 seconds by using a sputter coating machine (Sputter Coater-108, Cressinton Scientific Instruments, Watford, UK). The coated surfaces of the aerogel/epoxy and aerogel/PVA composites were observed with a field emission scanning electron microscope (FE-SEM, Nova NanoSEM 450, FEI Corp., OR, USA) to examine how the aerogel structure in each composite affected the thermal conductivity of the composite.

2.2.6. Weight fraction of the silica aerogel powder in the composite

The silica aerogel content in the composite was measured with a thermogravimetric analyzer (Q50, TA Instrument, New Castle, USA) under normal

atmospheric conditions at a temperature range of 40 to 900 °C with a heating rate of 10 °C /min.

2.2.7. Pore characterization of silica aerogel powder in the composite

The specific surface area of the aerogel and composites was measured using the Brunauer-Emmett-Teller method (BET method, ASSP 2010, Micromeritics, Norcross, USA). The aerogel and composite samples were heated to 110 °C under vacuum (10^{-5} Torr) for 1 h to remove adsorbed species. Nitrogen adsorption data were acquired at 77 K. All nitrogen adsorption/desorption measurements were equilibrated for 10 seconds before being recorded.

Table 2.2.1. Physical properties of materials used for the experiment.

| | Measured silica aerogel |
|------------------------------|-------------------------|
| Density (g/cm ³) | 0.05 |
| Thermal conductivity (W/m K) | 0.02 |
| Particle size (μm) | 1–10 (average 2.5) |
| Pore size (nm) | 1–20 (average 9) |

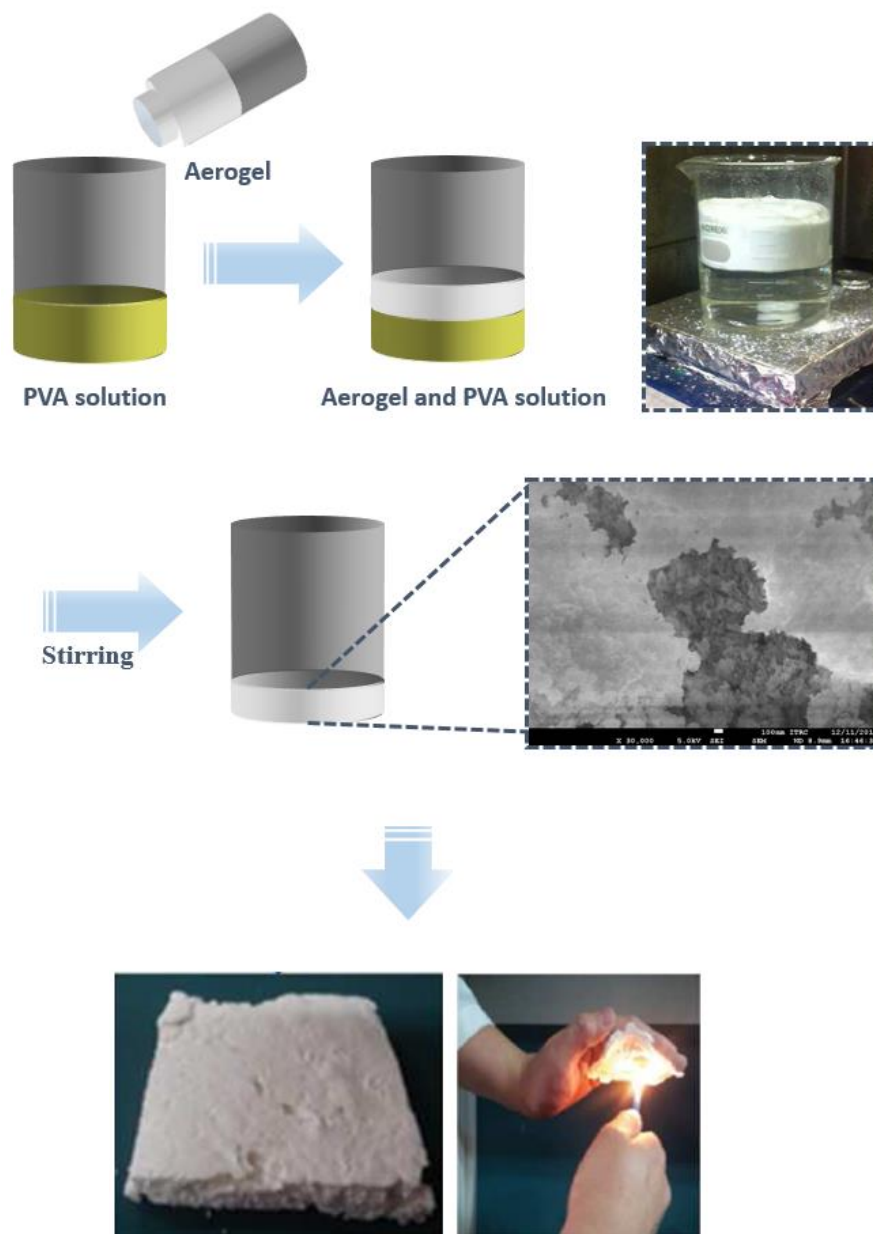


Figure 2.2.1. Processing procedures for preparation of silica aerogel/PVA composites.

2.2.3. Results and Discussion

Figure 2.2.2 shows the thermal conductivity of the silica aerogel/epoxy composite with respect to the volume fraction of aerogels. The Thermal conductivity of the silica aerogel/epoxy composite was measured and found to be in a range of from 0.112 to 0.123 W/m·K, which was equivalent to 41 ~ 46 % of that of the resin. Considering the low thermal conductivity of the aerogels, the 0.02 W/m·K, thermal conductivity of the silica aerogel/epoxy composite was higher than expected because the epoxy resin infiltrated into the pores of the silica aerogels as shown in figure 2.2.3. Ge et al. also reported that the pores of the silica aerogel were filled with the epoxy matrix when composites were prepared using silica aerogels and liquid epoxy [31]. It indicates that aerogel pores must be preserved to prepare composites with low thermal conductivity.

Figure 2.2.2 shows the thermal conductivity of silica aerogel/PVA composites prepared using the proposed process schematized in figure 2.2.1. The measured thermal conductivity of the silica aerogel/PVA composites ranged from 0.022 to 0.053 W/m·K, which values correspond to 11 ~ 27 % of the value of the resin and an outstanding flame retardant property of the composite was also observed as shown in figure 2.2.1.

As shown in figure 2.2.4(a), the pores in the silica aerogels are well preserved in the PVA-coated composite with 3 % PVA solution and the preserved pores of the silica aerogel incorporated in the composites were more clearly observed by the nitrogen adsorption result as summarized in Table 2.2.2. PVA coating layer of the silica aerogel/PVA composites was thicker and broader with increasing the concentration of PVA solution as shown in figure 2.2.4(b) ~ (d) and the pores inside the composites under PVA coating were preserved when considering morphology, surface area, and thermal conductivity results of the composites. For example, relatively low thermal conductivity of the composite with 20 % PVA solution, 0.053 W/m·K, can be achieved with low surface area of only 1 m²/g. Since the silica aerogel/PVA composite had lower thermal conductivity than the silica aerogel/epoxy composite, it is confirmed

from these results that the preservation of aerogel pores in the composite is an important requirement for excellent insulation properties. The lowest thermal conductivity of the silica aerogel/PVA composites prepared in this study, 0.022 W/m·K, was close to the thermal conductivity of the aerogel, 0.02 W/m·K, and was lower than the lowest thermal conductivity of silica aerogel/polyimide composites reported recently [29]. Therefore, the proposed process is effective enough to produce composites of low thermal conductivity by preserving aerogel pores.

PVA concentration in the solution, temperature of the hot plate, stirring rate, and volume ratio of the aerogel in the PVA solution are important factors for the proposed process in preparing composites with better physical properties. As described in the Supporting Information, the PVA concentration in the solution and the hot plate temperature were regarded as key process conditions. Figure 2.2.5(a) shows the thermal conductivity of the silica aerogel/PVA composite with respect to the PVA concentration. The thermal conductivity of the composite became lower as the PVA concentration decreased.

A thermal analysis of the silica aerogel/PVA composite was conducted to assess how the aerogel content is associated with the concentration of the PVA solution. Since the aerogel content in a composite can be measured according to the weight residue at 700 °C or higher, the remaining quantity of aerogels in the composite increases with decreasing PVA concentration as shown in figure 2.2.6(a). Therefore, it can be concluded from the weight residue and BET results shown in Table 2.2.2 that the extremely low thermal conductivity was generated by increasing the silica aerogel content and surface area inside the composites. Figure 2.2.5(b) shows how the thermal conductivity of the silica aerogel/PVA composite varies with hot plate temperature. Similar thermal conductivity was observed regardless of the hot plate temperature. It is shown by the graph plotted in figure 2.2.6(b) that the aerogel content was varied by small amount and that the hot plate temperature does not have a significant effect on the remaining amount of aerogels and is a minor factor compared with the concentration in the PVA solution.

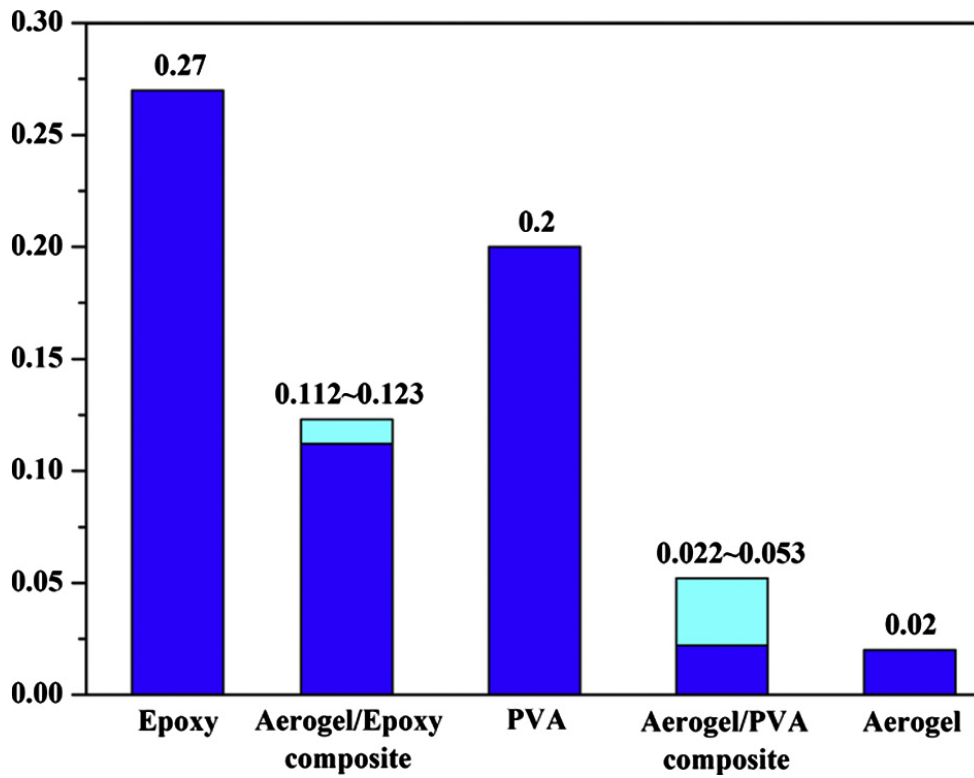


Figure 2.2.2. Thermal conductivity of raw materials and silica aerogel/polymer composites.

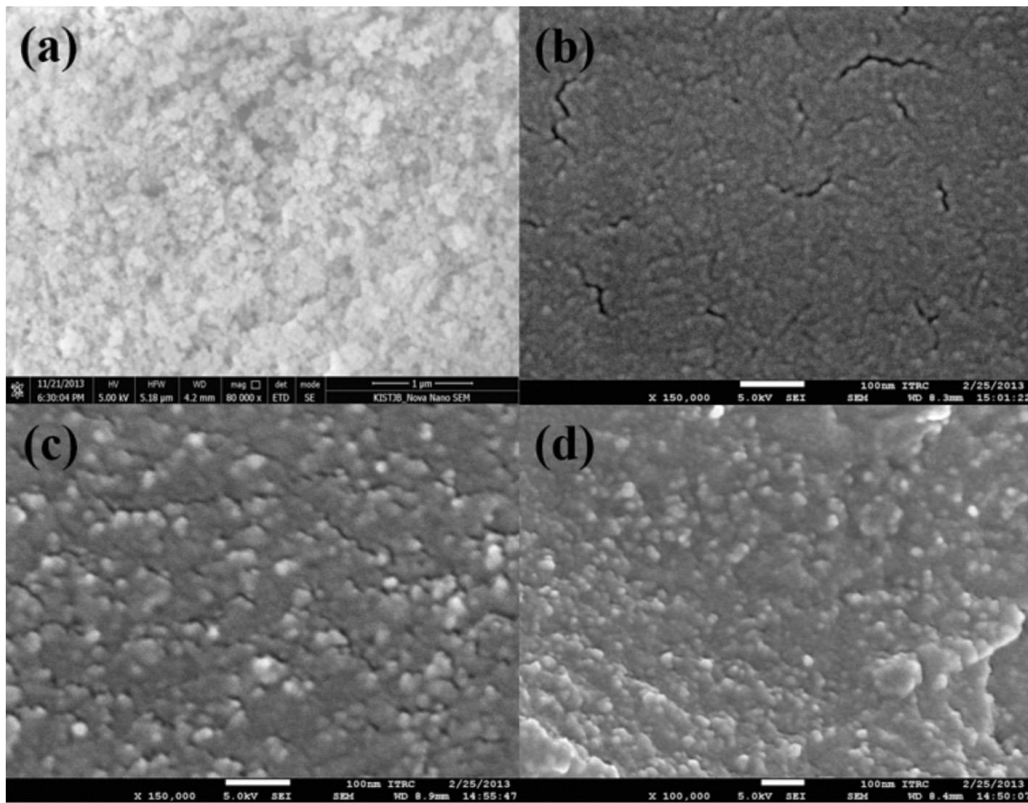


Figure 2.2.3. SEM images of (a) as-received silica aerogel powder and silica aerogel/epoxy composites with (b) 25, (c) 50 and (d) 75 vol % aerogel.

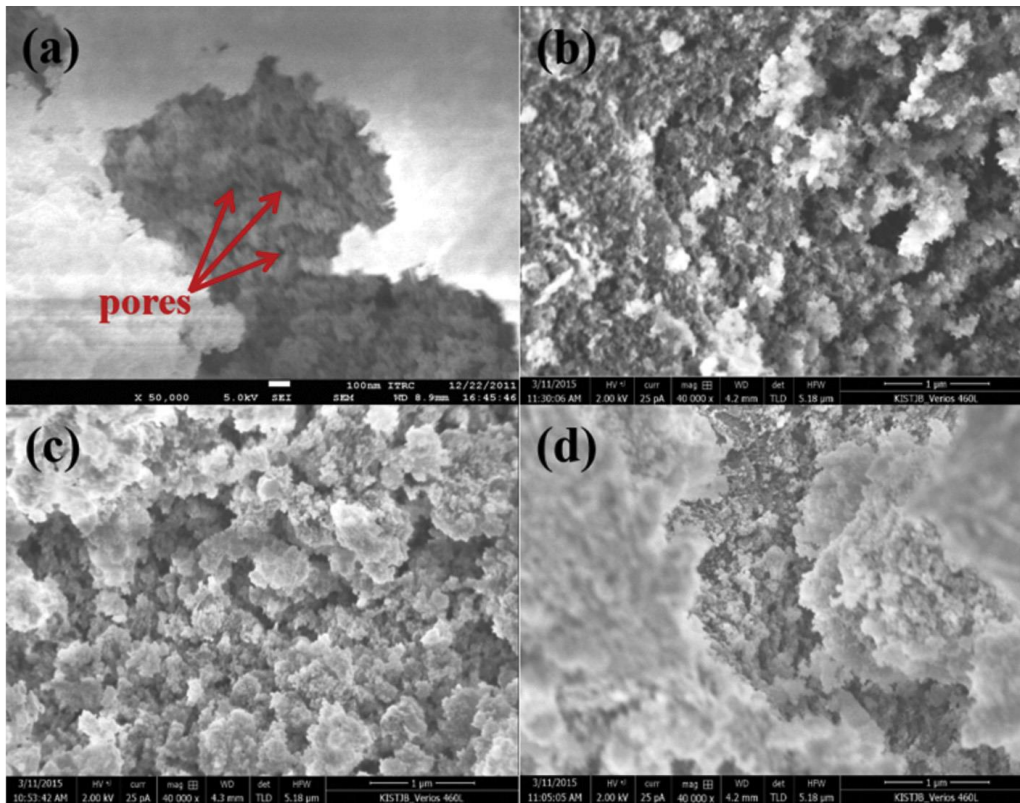


Figure 2.2.4. SEM images of the silica aerogel/PVA composites with (a) 3 % concentration of PVA solution with high magnification, (b) 3 % concentration of PVA solution, (c) 10 % concentration of PVA solution and (d) 20 % concentration of PVA solution.

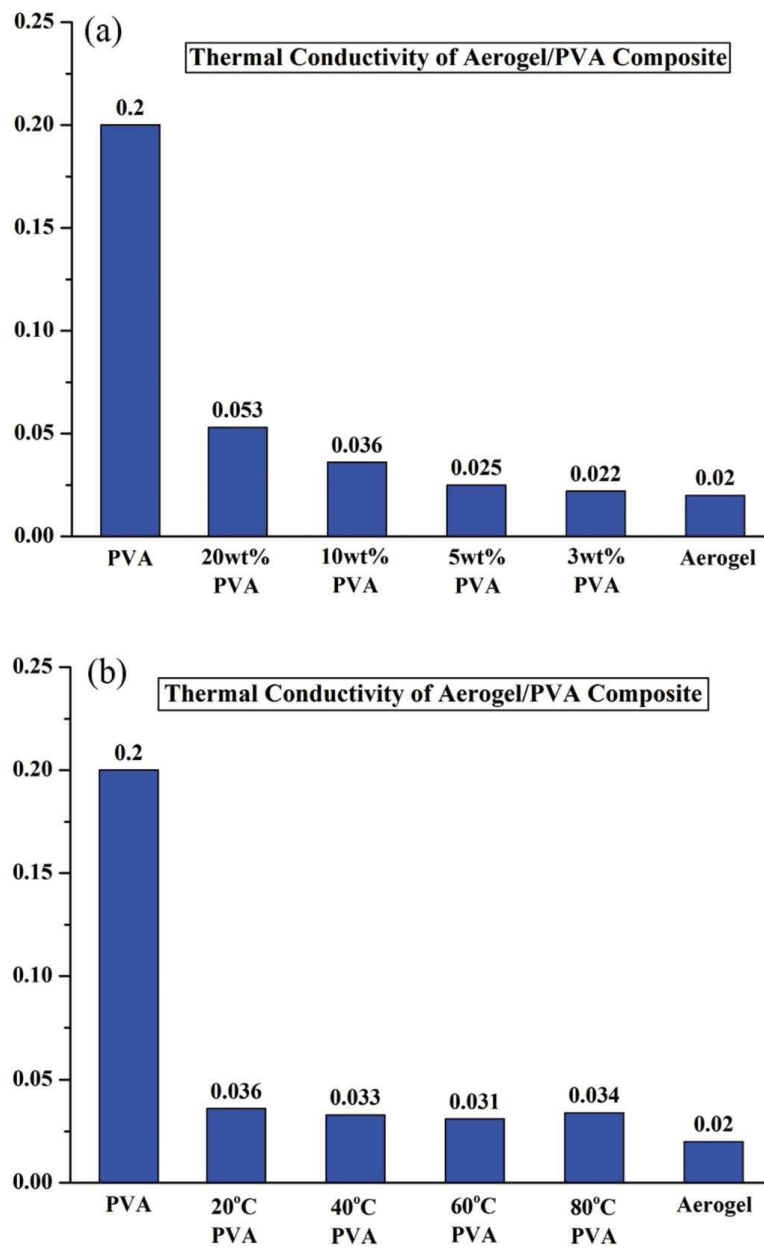


Figure 2.2.5. Thermal conductivity of silica aerogel/PVA composites with respect to (a) the concentration in the PVA solution at a hot plate temperature of 20 °C and (b) the hot plate temperature with the 10 wt% PVA solution.

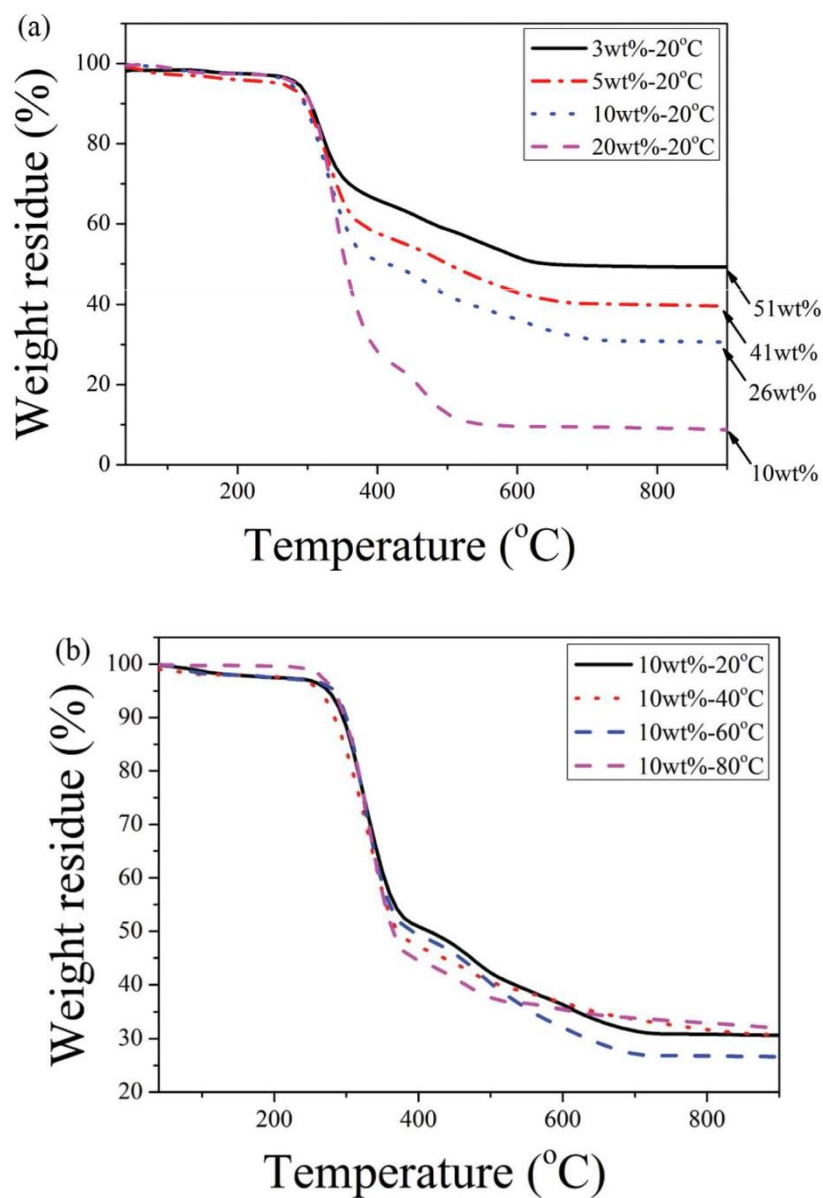


Figure 2.2.6. Thermogravimetric analysis curves for the silica aerogel/PVA composites with respect to (a) the concentration of the PVA solution at a hot plate temperature of 20 °C and (b) the hot plate temperature with the 10 wt% PVA solution.

Table 2.2.2. Surface area and density of the silica aerogel composites.

| | 25 vol% Epoxy | 50 vol% Epoxy | 75 vol% Epoxy |
|-----------------------------------|---------------|---------------|---------------|
| *Surface area (m ² /g) | 0 | 0 | 0 |
| Density (g/cc) | 1.11 | 1.11 | 1.12 |

* Surface area of the silica aerogel: 614 m²/g.

| | 20 wt% PVA | 10 wt% PVA | 5 wt% PVA | 3 wt% PVA |
|-----------------------------------|------------|------------|-----------|-----------|
| *Surface area (m ² /g) | 1 | 26 | 183 | 355 |
| Density (g/cc) | 0.98 | 0.93 | 0.85 | 0.74 |

2.2.4. Summary

A processing method was proposed in this study to prepare silica aerogel composites with preserved pores in the silica aerogel and extremely low thermal conductivity of the composites. Interfaces between the superhydrophobic silica aerogels and the hydrophilic PVA solution are generated and then the silica aerogel/PVA composites are fabricated forcibly during stirring while the PVA resin is precipitated over the interfaces by making the solvent vaporize at a slow rate. The silica aerogel/PVA composites prepared using the proposed process constituted the silica aerogel particles with well-preserved pores and exhibited a low thermal conductivity of 0.022 W/m·K. The thermal conductivity value is only 11 % of thermal conductivity of the PVA resin and 20 % of the lowest thermal conductivity of the silica aerogel/epoxy composites without preserving the aerogel pores. Assuming that the pores in silica aerogels are well preserved, the volume fraction of the silica aerogel in the composites is the most important physical factor determining the thermal conductivity and the volume fraction of the aerogel is strongly dependent on the concentration in the PVA solution.

2.2.5. Supplementary Information

With regard to the proposed fabrication process for production of silica aerogel/PVA composites, several key process conditions were determined and a pilot test was conducted to investigate the effects of certain process conditions on the thermal conductivity of the composites. As mentioned in the manuscript, the PVA concentration in the solution, the hot plate temperature, the stirring rate and the volume ratio of the PVA solution were suggested and investigated as important processing parameters. Since a higher the content of aerogel in composites leads to the lower their thermal conductivity becomes, the 1:1 volume ratio of PVA solution to aerogel used in this study is regarded as a condition that allows final composite materials to have the highest possible aerogel content. In the pretest results, the stirring rate was fixed at 300 rpm, a favorable condition for the preparation of specimens. Higher stirring rates hindered the formation of interfaces and thus led to the decreased thermal conductivity of the finished composite materials, and at lower stirring rates it became difficult to prepare specimens. This is thought to have resulted from the lack of physical force in mixing precipitated PVA in aerogels. The condition of hot plate temperature was pre-tested at 20 °C intervals, and in some cases, specimens could not be obtained at 80 °C as shown in Table S2.2.1. For the hot plate, we determined the four final temperature conditions of 20, 40, 60 and 80 °C. The PVA solution was prepared at concentrations of 3, 5, 10, 20 and 30 wt%. However, the 30 wt% PVA solution was excluded from the process conditions because its high viscosity made it difficult to prepare the specimen. As a result, the four concentration levels of 3, 5, 10 and 20 wt% were used for the PVA solution.

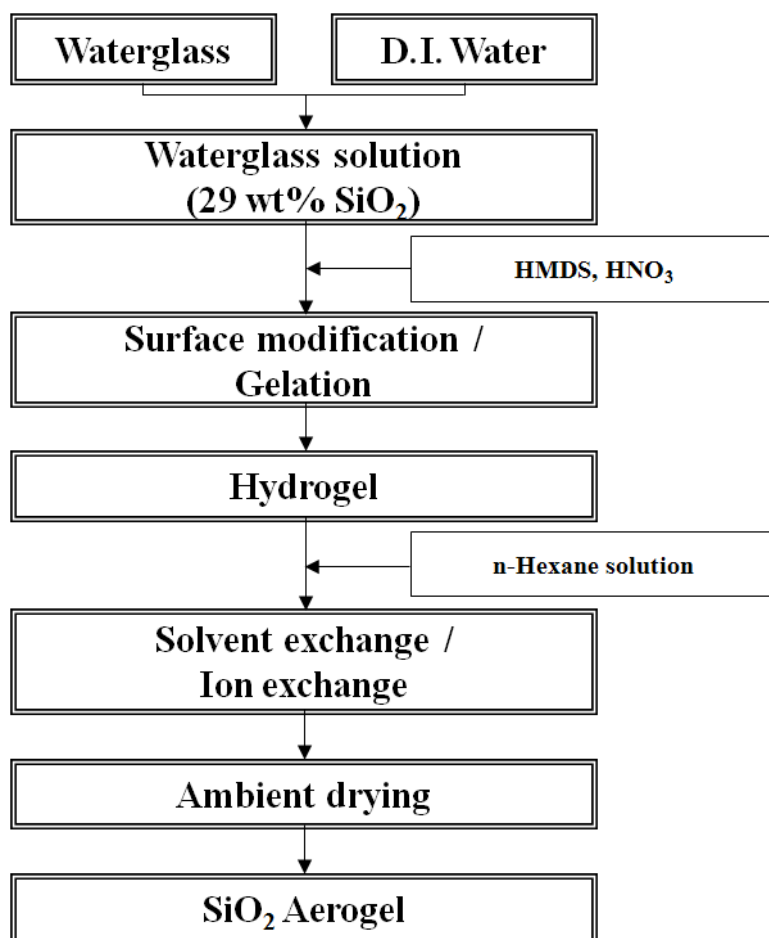


Figure S2.2.1. Schematic diagram of the aerogel synthesis. In the first step of the synthesis, water glass was used as the starting material and silica sol with a silica content of 29 wt% was prepared using distilled water. For surface modification and gelation, hexamethyldisiloxane and nitric acid were added to the silica sol. The hydrogel obtained by the co-precursor method was immersed in an n-Hexane solvent at 60 °C for 10 h in order to exchange the solvent and remove ions, including sodium. The modified gel was dried continuously at 170 °C for 20 min and 200 °C for 10 min under the ambient pressure.



Figure. S2.2.2 Image of the interface between the silica aerogel and the PVA solution with respect to the volume of the raw materials.

Table S2.2.1. Success or failure of specimen preparation under different process conditions.

| | 20 °C | 40 °C | 60 °C | 80 °C |
|--------|-------|-------|-------|-------|
| 3 wt% | ○ | × | × | × |
| 5 wt% | ○ | ○ | ○ | × |
| 10 wt% | ○ | ○ | ○ | ○ |
| 20 wt% | ○ | ○ | ○ | × |
| 30 wt% | × | × | × | × |

2.2.6. References

- [1] Lu X, Arduini-Schuster M, Kuhn J, Nilsson O, Fricke J, Pekala R. Thermal conductivity of monolithic organic aerogels. *Science* 1992, 255, 971-972.
- [2] Biener J, Stadermann M, Suss M, Worsley M, Biener M, Rose K, et al. Advanced carbon aerogels for energy applications. *Energy Environ Sci* 2011, 4, 656-667.
- [3] Guo K, Hu Z, Song H, Du X, Zhong L, Chen X. Low-density graphene/carbon composite aerogels prepared at ambient pressure with high mechanical strength and low thermal conductivity. *RSC Adv* 2015, 5, 5197-5204.
- [4] Chang Y, Wu C, Wu P. Synthesis of large surface area carbon xerogels for electrochemical double layer capacitors. *J Power Sources* 2013, 223, 147-154.
- [5] Cao F, Ren L, Li X. Synthesis of high strength monolithic alumina aerogels at ambient pressure. *RSC Adv* 2015, 5, 18025-18028.
- [6] Yang J, Li S, Luo Y, Yan L, Wang F. Compressive properties and fracture behavior of ceramic fiber-reinforced carbon aerogel under quasi-static and dynamic loading. *Carbon* 2011, 49, 1542-1549.
- [7] Karout A, Buisson P, Perrard A, Pierre A. Shaping and mechanical reinforcement of silica aerogel biocatalysts with ceramic fiber felts. *J Sol-Gel Sci Technol* 2005, 36, 163-171.
- [8] Chen B, Shih C, Chen A. Ductile PLA nanocomposites with improved thermal stability. *Compos Pt A-Appl Sci Manuf* 2014, 43, 2289-2295.
- [9] Mirzapour A, Asadollahi M, Baghshaei S, Akbari M. Effect of nanosilica on the microstructure, thermal properties and bending strength of nanosilica modified carbon fiber/phenolic nanocomposite. *Compos Pt A-Appl Sci Manuf* 2014, 63, 159-167.
- [10] Zhao J, Du F, Cui W, Zhu P, Zhou X, Xie X. Effect of silica coating thickness on the thermal conductivity of polyurethane/SiO₂ coated multiwalled carbon nanotube composites. *Compos Pt A-Appl Sci Manuf* 2014, 58, 1-6.
- [11] Kistler S. Coherent expanded aerogels and jellies. *Nature* 1931, 127, 741.
- [12] Hüsing N, Schubert U. Aerogels-airy materials: chemistry, structure, and properties. *Angew Chem Int Edit* 1998, 37, 22-45.

- [13] Fricke J. Aerogels – highly tenuous solids with fascinating properties. *J Non-Cryst Solids* 1988, 100, 169-173.
- [14] Fricke J, Emmerling A. Aerogels. *J Am Ceram Soc* 1992, 75, 2027-2036.
- [15] Schultz J, Jensen K, Kristiansen F. Super insulating aerogel glazing. *Sol Energy Mater Sol Cells* 2005, 89, 275-285.
- [16] Dorcheh A, Abbasi M. Silica aerogel; synthesis, properties and characterization. *J Mater Process Technol* 2008, 199, 10-26.
- [17] Moreno-Castilla C, Maldonado-Hódar F. Carbon aerogels for catalysis applications: an overview. *Carbon* 2005, 43, 455-465.
- [18] Tomasi R, Sireude D, Marchand R, Scudeller Y, Guillemet P. Preparation of a thermal insulating material using electrophoretic deposition of silica particles. *Mater Sci Eng B-Adv Funct Solid-State Mater* 2007, 137, 225-231.
- [19] Fesmire J, Sass J. Aerogel insulation applications for liquid hydrogen launch vehicle tanks. *Cryogenics* 2008, 48, 223-231.
- [20] Rani T, Subha M, Reddy G, Kim Y. H, Ahn Y. S. *J Appl Polym Sci* 2010, 115, 1675-1679.
- [21] Baetens R, Jelle B, Gustavsen A. Aerogel insulation for building applications: a state-of-the-art review. *Energy Build* 2011, 43, 761-769.
- [22] Sehaqui H, Zhou Q, Berglund L. High-porosity aerogels of high specific surface area prepared from nanofibrillated cellulose (NFC). *Compos Sci Technol* 2011, 71, 1593-1599.
- [23] Randall J, Meador M, Jana S. Tailoring mechanical properties of aerogels for aerospace applications. *ACS Appl Mater Interfaces* 2011, 3, 613-626.
- [24] Schmidt M, Schwertfeger F. Applications for silica aerogel products. *J Non-Cryst Solids* 1998, 225, 364-368.
- [25] Kim G. S, Hyun S. H. Effect of mixing on thermal and mechanical properties of aerogel-PVB composites. *J Mater Sci* 2003, 38, 1961-1966.
- [26] Teh P, Mariatti M, Wagiman A, Beh K. Effect of curing agent on the properties of mineral silica filled epoxy composites. *Polym Compos* 2008, 29, 27-36.
- [27] Zhao J, Ge D, Zhang S, Wei X. Studies on thermal property of silica

aerogel/epoxy composite. Mater Sci Forum 2007, 546-549.

[28] Gupta N, Ricci W. Processing and compressive properties of aerogel/epoxy composites. J Mater Process Technol 2008, 198, 178-182.

[29] Kim S. Y, Noh Y. J, Lim J, You N. H. Silica aerogel/polyimide composites with preserved aerogel pores using multi-step curing. Macromole Res 2014, 22, 108-111.

[30] Kim H. M, Kim H. S, Kim S. Y, Youn J. R. Silica aerogel/epoxy composites with preserved aerogel pores and low thermal conductivity. E-Polymers 2015, 15, 111-117.

[31] Ge D, Yang L, Li Y, Zhao J. Hydrophobic and thermal insulation properties of silica aerogel/epoxy composite. J Non-Cryst Solids 2009, 355, 2610-2615.

III. Shape Memory Polyurethane Foam

3.1. Synergistic Effect of Dual-Scale Hybrid Shape Memory Foam

3.1.1. Introduction

Interest on insulating materials has increased since an effective insulating material plays a key role in saving energy and reducing carbon dioxide production. In particular, polyurethane (PU) foams have been used in many insulation applications due to their low thermal conductivity and good processability [1-3]. PU is generally composed of hard and soft segments, and their thermodynamic incompatibility results in a phase separated structure. Hard segments formed by hydrogen bonding with dipole-dipole interaction affect the crystallization below the melting temperature and soft segments act as a reversible phase controlling the shape memory effect. Due to the thermo-elastic phase transformation, PU is used as a shape memory polymer (SMP) which can be deformed in response to external stimuli such as heat, light, moisture, pH, and electric field [4-10]. The shape memory materials have received significant attention recently [11-14]. For instance, shape memory alloys (SMAs) such as copper-aluminium-nickel (Cu-Al-Ni) and nickel-titanium (NiTi) alloys show superior shape memory performance and good stability. However, their manufacturing processes are complex and expensive [15-17]. On the other hand, shape memory polyurethane (SMPU) has been recognized as a fascinating shape memory material due to its excellent properties including a wide temperature range for shape recovery (-30 ~ 70 °C), high shape recoverability, easy processing conditions, and low cost compared with SMAs [18-21]. Moreover, the SMPU can be controlled by changing the molar ratio of hard segments to soft segments, molecular weight of soft segments, and polymerization process [22-24].

Two different blowing agents have usually been adopted for foaming of the

SMPU, i.e., chemical blowing agent and physical blowing agent [25-27]. The salt leaching method was used in this study to produce a new foam structure with dual scale pore sizes [28]. The dual scale hybrid PU foam showed strong shape memory behavior and synergistic enhancement was found in the thermal and mechanical performance of the hybrid foam. Theoretical analysis for heat transfer and numerical modeling for mechanical response of the SMPU foam were carried out and compared with experimental results.

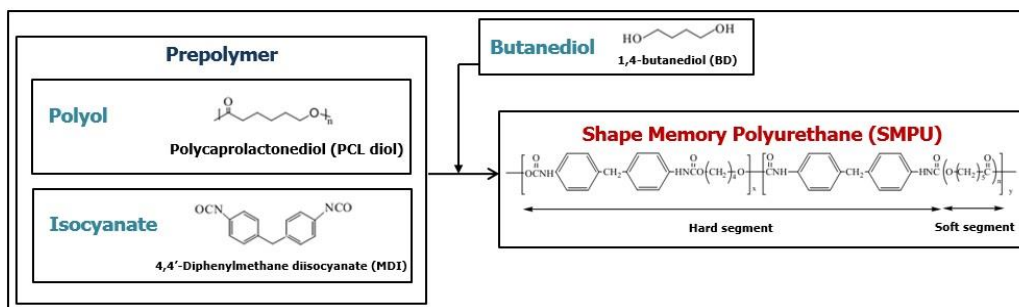
3.1.2. Experimental Section

3.1.2.1. Synthesis of SMPU

A mixture of poly caprolactone diol (PCL diol, $M_n=4,000$ g/mol, Perstop) and 4,4'-diphenylmethane diisocyanate (MDI, Junsei Chemical) was reacted in a four neck cylindrical flask with continuous mechanical stirring under nitrogen atmosphere at 80 °C for 3h to prepare a prepolymer. 1,4-butanediol (BD, Sigma Aldrich) was added into the prepolymer as a chain extender for controlling the degree of polymerization. The SMPU obtained by the prepolymerization method was dried at room temperature under vacuum to remove the solvent and hardened further at 100 °C in an oven for morphological stabilization. (Scheme 3.1.1).

3.1.2.2. Fabrication of SMPU foam

The processing procedure for the SMPU foam is described schematically in figure 3.1.1. First, SMPU pellets were dissolved in tetrahydrofuran (THF, Daejung Chemicals) and a 25 wt% solution of SMPU in THF was prepared. Sodium chloride (NaCl, Daejung Chemicals) particles were ground and filtered by several micro glass filters with pore sizes of 100, 200, and 400 μm to control the pore size of the SMPU foam. Filtered NaCl particles were added to the SMPU solution at a volume ratio of 8 to 10 and SMPU/NaCl composites were prepared by using the different particle sizes of NaCl. The mixture of SMPU/NaCl particle was dried at 40 °C for 3 days to remove the THF completely. In order to leach NaCl particles from the SMPU/NaCl composite, the composite samples were immersed in deionized (DI) water. The SMPU foams with pore sizes of 100, 200 and 400 μm were obtained by drying at room temperature for 2 days. A hybrid SMPU foam with dual scale pores with sizes of 100 and 400 μm and a functionally gradient SMPU foam composed of 100, 200 and 400 μm pores were also prepared.



Scheme 3.1.1. Schematic diagram of the synthesis of shape memory polyurethane (SMPU) by prepolymerization method.

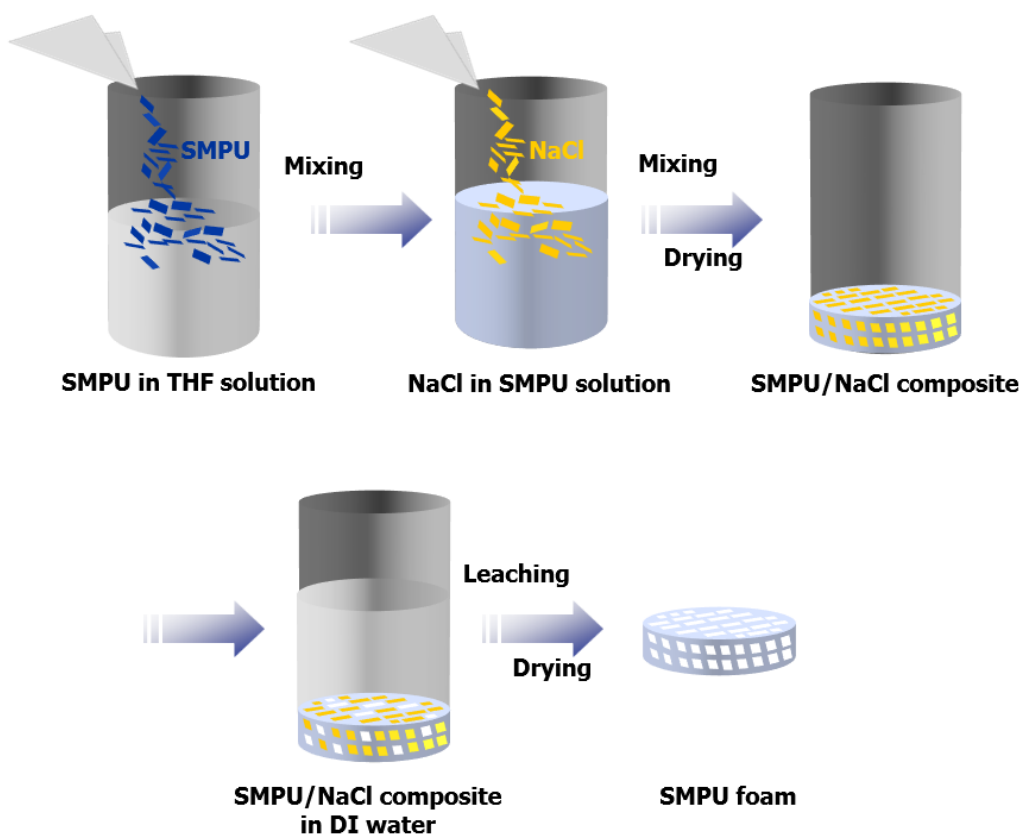


Figure 3.1.1. Processing procedure for preparation of SMPU foams.

3.1.2.3. Structural Characterization

Isopropyl alcohol (IPA) was used as a solvent to measure the average diameter of the NaCl particles. A particle size analyzer (S3500 Series, Microtrac Inc.) based on the laser light diffraction method was used in order to determine the particle size distributions of the samples. The morphology of the filtered NaCl particles and fractured surface of the SMPU foam were observed with a field-emission scanning electron microscope (FE-SEM, JSM-7600F, JEOL) to investigate the internal structure of the SMPU foam.

3.1.2.4. Thermal Characterization

The transition temperature (T_{tr}) of the SMPU was measured with a differential scanning calorimeter (DSC, 200 F3 Maia, Netzsch) from -20 °C to 250 °C at a heating rate of 10 °C/min. Figure S3.1.3 shows the results of the DSC analysis. An endothermic peak was observed at 53.8 °C. Previous studies have reported the relation between the transition temperature and molecular structure of SMPU synthesized with PCL as polyol [34-36]. The thermal conductivity of the specimen was measured with a thermal analyzer (TCi, C-THERM) which is based upon the modified transient plane source (MTPS) method. The thermal analyzer has a central heater/sensor element surrounded by a guard ring which is used as a heat generator. The one-sided interfacial reflectance sensor supplies heat to the sample. The range of measurable thermal conductivity of the apparatus is from 0 to 100 W/m·K.

3.1.2.5. Shape Memory and Mechanical Characterization

Thermo-mechanical tests were carried out with a temperature controlled universal testing machine (UTM, WL2100, WITHLAB) to investigate the shape memory effect and compressive stress of the SMPU foam. The specimens were prepared with a size of 35 (diameter) × 20 (thickness) mm². The specimen was heated

up to T_h and compressed to 80 % of its original thickness with a crosshead speed of 10 mm/min. The specimen was cooled down to T_l and then maintained at the temperature for 10 min after the removal of the load. The specimen was reheated to T_h and maintained at the temperature for 10 min. The shape recovery and shape fixity are obtained by using the following equations.

$$\text{Shape recovery (\%)} = \frac{\varepsilon_m - \varepsilon_r}{\varepsilon_m} \times 100 \quad (3.1.1)$$

$$\text{Shape fixity (\%)} = \frac{\varepsilon_f}{\varepsilon_m} \times 100 \quad (3.1.2)$$

where $T_h = T_{ir} + 20^\circ\text{C}$, $T_l = T_{ir} - 20^\circ\text{C}$, ε_m = strain at an 80 % compression, ε_r = recovered strain at T_h , and ε_f = strain at T_l .

3.1.3. Theoretical section

3.1.3.1. Heat transfer theory

Heat transfer mechanisms in foam materials are classified into three categories: convection, conduction, and radiation. If the cell size is smaller than 1.5 mm, convection can be neglected because the space in each cell is extremely small [37]. Therefore, the overall thermal conductivity of the foam is determined by conduction and radiation heat transfer [38]. However, it is difficult to make accurate prediction because foams consist of complex microstructures and energy radiation can be absorbed or scattered in the foam structure. The effective thermal conductivity of the foam was proposed by Glickman as shown below [39, 40].

$$K = K_g + \left(\frac{2}{3} - \frac{f_s}{3} \right) (1 - V_g) K_s \quad (3.1.3)$$

where K_g is the conductivity of the gas, f_s is the proportion of strut in the total polymer, V_g is the porosity of the foam material, and K_s is the conductivity of polymer. The estimation of radiation heat transfer can be carried out based on experimental data by using Rosseland's radiation theory. In this paper, the radiative contribution to heat transfer as a function of the cell size is given by the equation shown below [41].

$$K_r = k \frac{4\sigma\varepsilon LT^3}{2 - \varepsilon} \quad (3.1.4)$$

where σ is the Stefan-Boltzmann constant, ε is the emissivity, L is the cell size of foam material, T is temperature, and k is the correction factor obtained by experimental data. As a result, the overall thermal conductivity of the SMPU foam can be re-expressed as below.

$$K = K_g + \left(\frac{2}{3} - \frac{f_s}{3} \right) (1 - V_g) K_s + k \frac{4\sigma\epsilon LT^3}{2 - \epsilon} \quad (3.1.5)$$

3.1.4. Results and Discussion

NaCl particles were employed to generate pores in the PU matrix and their size was controlled by grinding and filtering (Figure S3.1.1). The average particle sizes of the prepared NaCl particles were 127.5, 242 and 413.8 μm , which were almost equal to the sizes of the used filters. SEM images of the SMPU foams fabricated using the filtered NaCl particles are presented in figures 3.1.2(a)-(c). After SMPU/NaCl composites were prepared, the NaCl particles were dissolved by immersing them in DI water. The pore size of the SMPU foam was found consistent with the particle size of NaCl. Figures 3.1.2(d) and e presents the functionally gradient SMPU foam and the dual scale hybrid SMPU foam with two different size pores, 100 and 400 μm , respectively. The porosity of the SMPU foam was calculated by using the following equation.

$$V_g = \left(1 - \frac{\rho_f}{\rho_p}\right) \times 100 \quad (3.1.6)$$

where ρ_p denotes the density of the SMPU and ρ_f is the density of the SMPU foam. As shown in figure 3.1.2(f), the porosities of SMPU foam-100, SMPU foam-200, and SMPU foam-400 were in the range from 84 to 85 %. The porosity of the hybrid SMPU foam was higher than those of the other SMPU foams because the 100 μm size pores were interspersed among the 400 μm pores. On the other hand, the porosity of the functionally gradient SMPU foam was 84.7 %, which is similar to the porosity of SMPU foam-100, SMPU foam-200, and SMPU-400.

Figure 3.1.3 shows the experimental and theoretical thermal conductivity of the SMPU foam with respect to the pore size of the SMPU foam. The thermal conductivity of the SMPU foam was measured to be in the range of 0.061 to 0.055 $\text{W/m}\cdot\text{K}$ as the pore size of the SMPU foam decreased from 400 to 100 μm . The

thermal conductivity results can be explained by the interfacial thermal resistance [29]. The interfacial thermal resistance is generated between pores in the SMPU foam. Since a larger interface is created between cells according to reduction of the pore size of the SMPU foam, the heat transfer of the SMPU foam is disturbed due to the effect of phonon scattering. It was reported that the radiation heat transfer inside the foam was reduced by decreasing the pore size of the foam [30, 31]. The experimental thermal conductivity of the hybrid SMPU foam was $0.047 \text{ W/m}\cdot\text{K}$, which was the lowest value among the samples because it has the highest interfacial area and porosity. The theoretical thermal conductivity of the SMPU foam yielded similar results by adjusting the correction factor. The predicted thermal conductivity of the SMPU foam became lower as the cell size decreased since the radiation heat transfer in the SMPU foam varied with the cell size.

The specific compressive modulus of SMPU foams was predicted by carrying out FE simulation. Figures 3.1.4(a) and (b) show the simplified 3D geometric structures of the SMPU foams considered in the calculation. Since the SMPU foam-400 has lower porosity, it experiences lower compressive stress. There is no effect of the pore size on the predicted compressive stresses since the elastic solid analysis deals with a liner system. That is why the foams with the same porosities even with different size pores have the same mechanical behavior. Moreover, the porosity is not a function of pore size when considering the spatial arrangement of pores.

The stress-strain behavior of the SMPU foam obtained by the compressive test is shown in figure 3.1.5. As shown in figure 3.1.5(a), the specific compressive stress of the SMPU foam was increased with decreasing the pore size in the SMPU foam. This can be explained by the buckling effect [32]. The ratio of the length to the cross sectional area of a column is called the slenderness ratio. As the slenderness ratio in the SMPU foam increased, the SMPU structure is easily bent and buckled. Since increasing the pore size of the SMPU foam may have generated a larger slenderness ratio, the buckling phenomenon can occur more readily. On the other hand, it was found that the hybrid SMPU foam has the highest specific compressive stress and modulus. This can be explained by not only the slenderness ratio but also the

synergistic effect.

In particular, the latter may arise from the so-called ‘size effect’ of dual scale pores. Regarding the slenderness, the hybrid SMPU had the lowest slenderness ratio among the other SMPU foam specimens including SMPU foam-100, SMPU foam-200, SMPU foam-400, and functionally gradient SMPU foam. The specific compressive moduli of the SMPU foam-400 and the hybrid SMPU foam predicted by the numerical calculation are compared with experimental data in figure 3.1.5(c). The measured specific compressive modulus was consistent with the numerical results. The hybrid SMPU foam had the highest specific compressive modulus, which could be explained by the synergistic effect.

Thermo-mechanical cyclic tests were performed to investigate the shape memory effect of the prepared SMPU foam-400. The experimental results of the thermo-mechanical cycles are shown in figure 3.1.6. The stress-strain curve is obtained from each loading and unloading cycle. The compressive stress was decreased slightly with respect to the number of cycles. Linear elastic deformation was observed in the initial stress region because of the elastic buckling of cells and the densification of the structure, while the shape fixity and shape recovery of SMPU foam was maintained well. The shape recovery and shape fixity of the SMPU foams are demonstrated in Supporting Information. The Shape recovery of the SMPU foam was higher than 98 % and shape fixity of the SMPU foam ranged from 97 to 98 %.

Figure 3.1.7 shows the morphological and thermal behavior of the SMPU foam-400 during the thermo-mechanical cycles. The main advantage of the SMPU foam adopted in this study is the capability of controlling the thermal characteristics of foam materials in a systematic manner. The cells in the SMPU foam with a pore size of 400 μm were dented during the compression of the SMPU foam at above transition temperature. The porosity of the SMPU foam decreased from 85.5 to 58.7 % at room temperature. After heating to above the transition temperature (T_{tr}), the porosity of the SMPU foam changed from 58.7 to 84.6 %. It can be seen that the pores of the SMPU foam almost recovered to their original shape as shown in figure 3.1.7(c). Figure 3.1.7(d) demonstrates the porosity changes during the cycle.

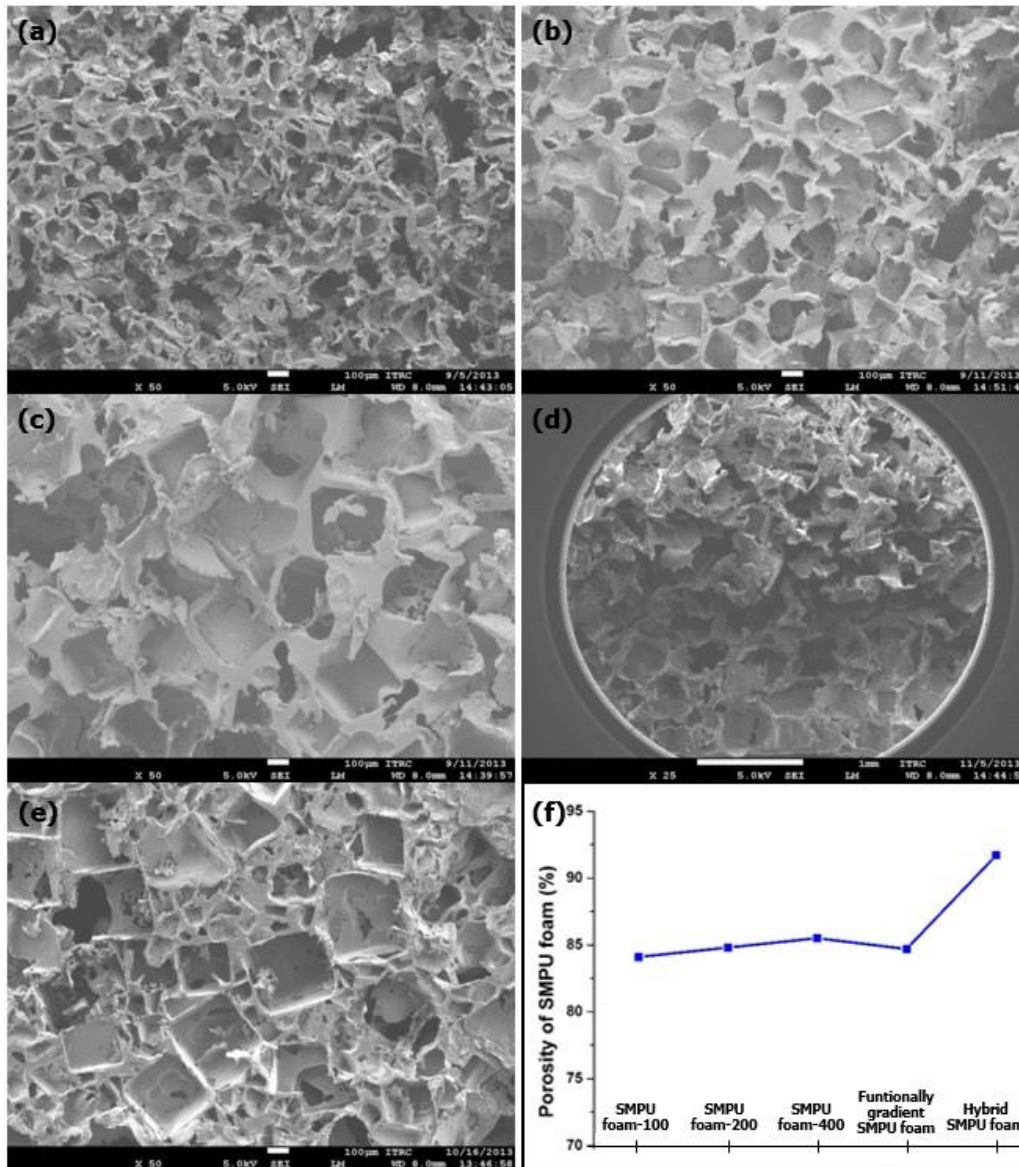


Figure 3.1.2. SEM images of SMPU foam specimens: (a) SMPU foam-100, (b) SMPU foam-200, (c) SMPU foam-400, (d) functionally gradient SMPU foam, and (e) hybrid SMPU foam and (f) porosity of the SMPU foams.

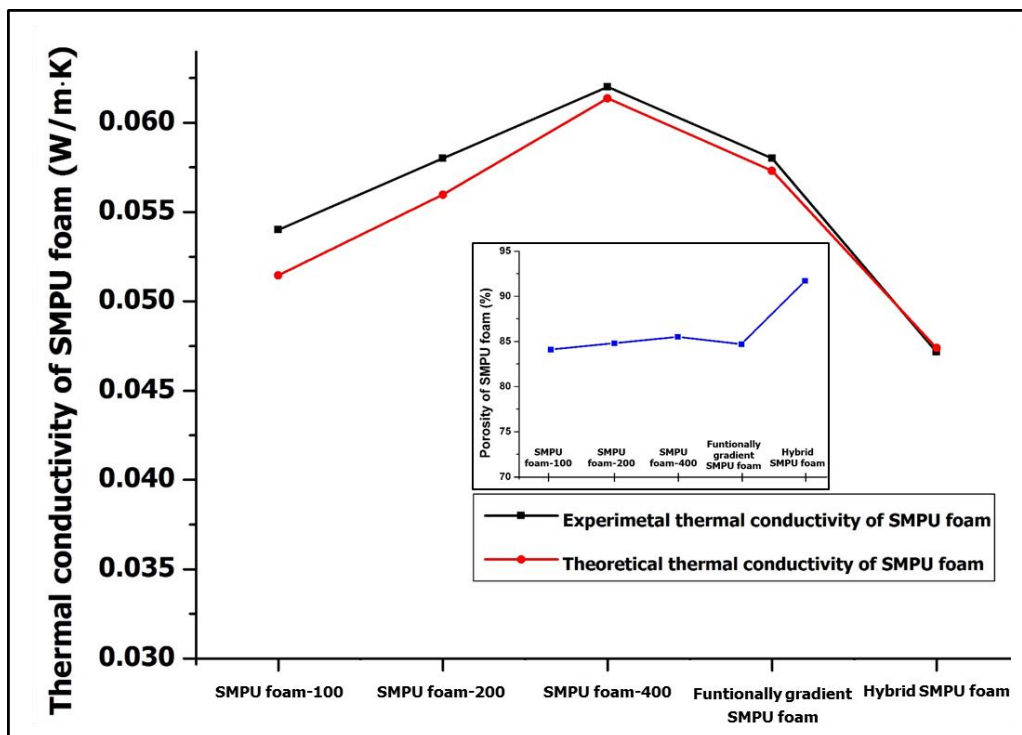


Figure 3.1.3. Experimental and theoretical thermal conductivity of SMPU foams.

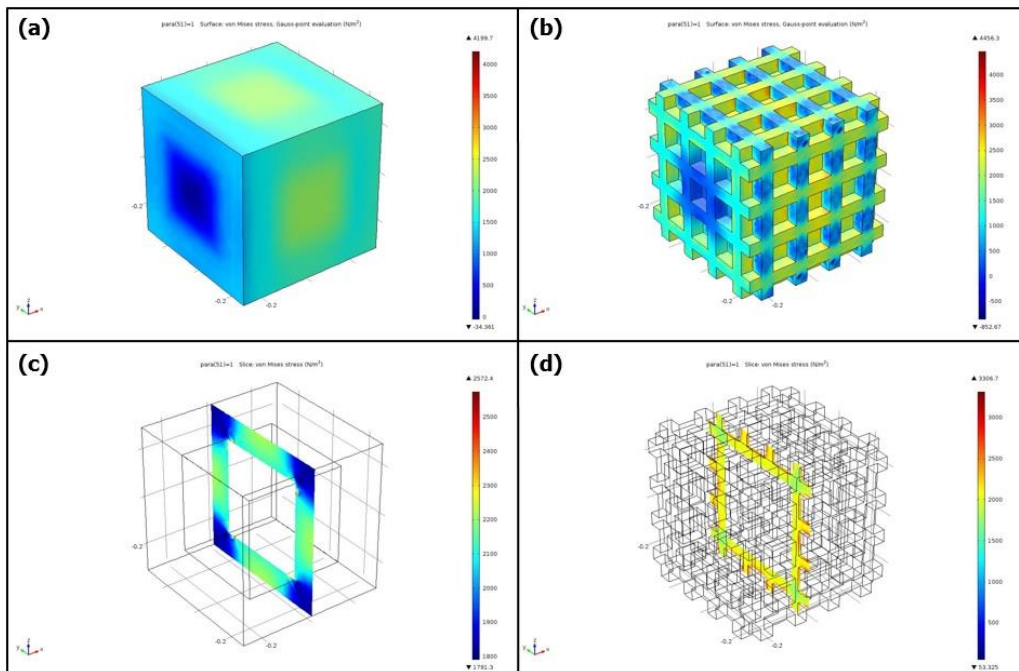


Figure 3.1.4. Numerical simulation results: (a) 3 dimensional unit cell of SMPU foam-400, (b) 3 dimensional unit cell of hybrid SMPU foam, (c) compressive stress field of SMPU foam-400, and (d) compressive stress field of hybrid SMPU foam.

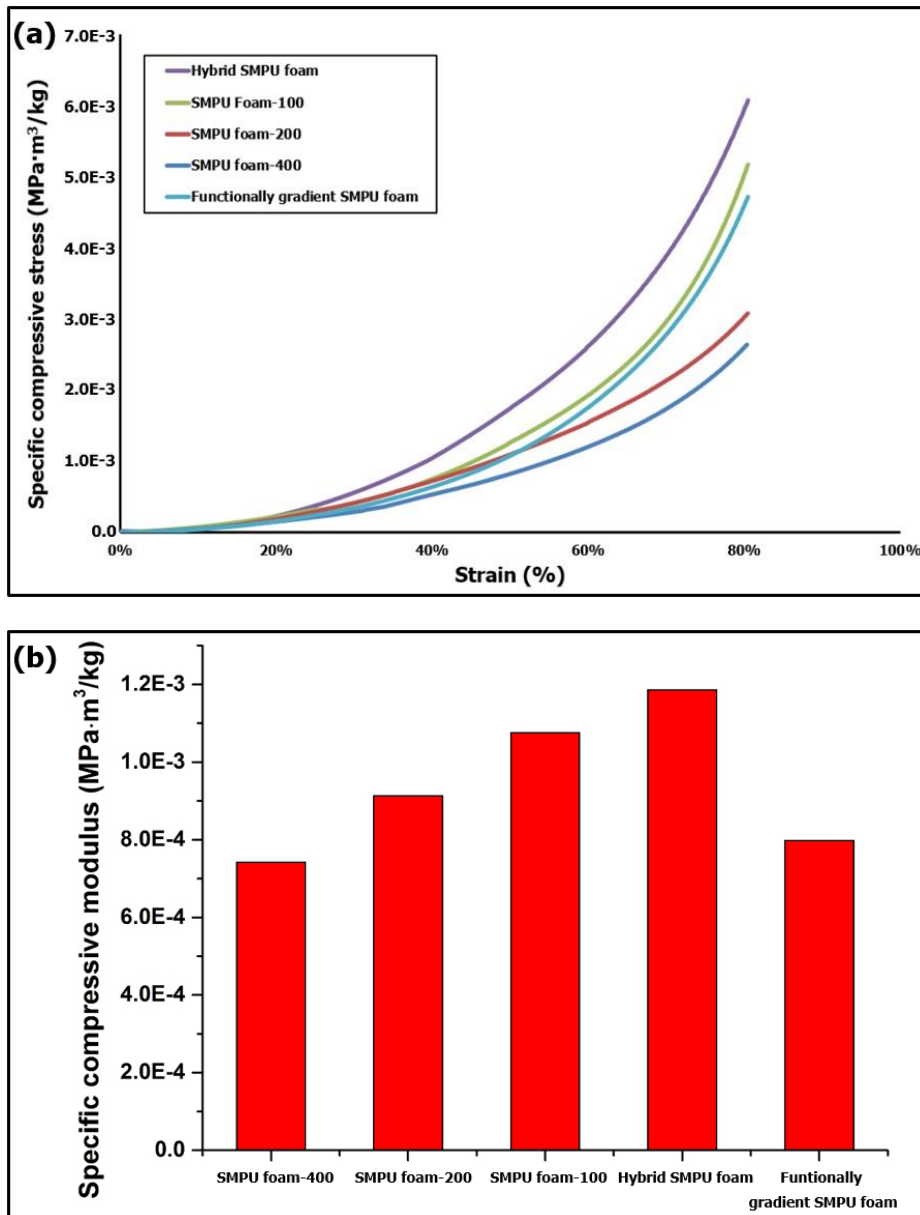


Figure 3.1.5. (a) Compressive stress-strain curves of SMPU foams, (b) moduli of the SMPU foams, and (c) comparison of experimental and numerical specific compressive moduli of SMPU foams.

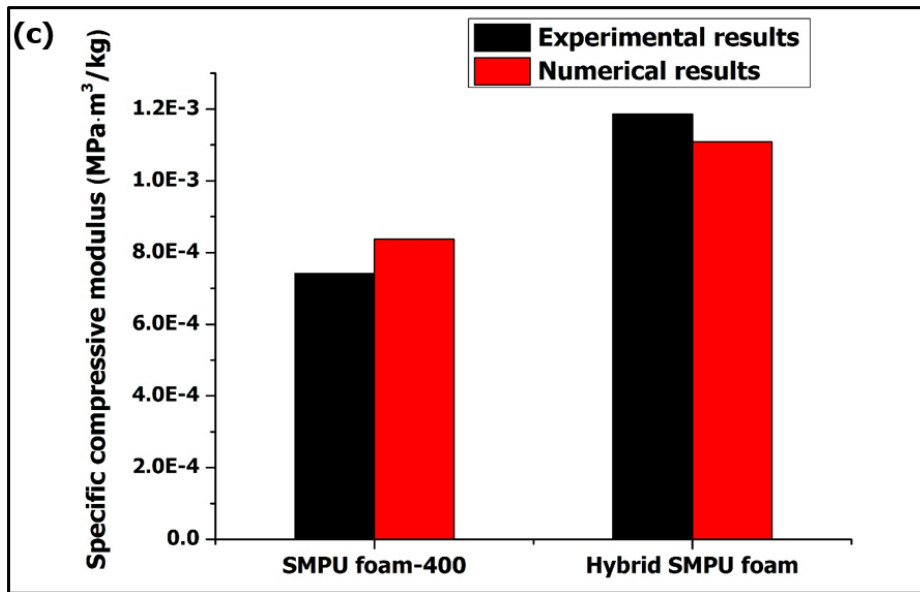


Figure 3.1.5. (continued)

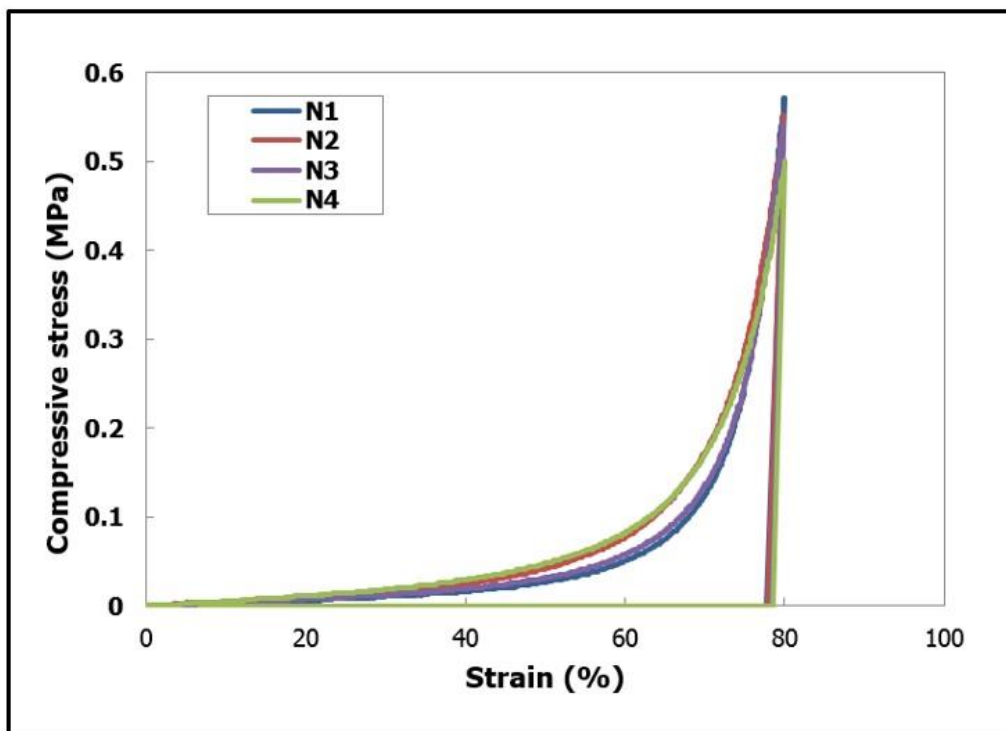


Figure 3.1.6. Results of each thermo-mechanical cyclic loading of the SMPU foam-400 specimen for 4 cycles.

Change in the thermal conductivity and thermal resistance of the SMPU foam in the original, compressed, and recovered states is presented in figure 3.1.7(e). In particular, the thermal resistance of the SMPU foam showed a dramatic change depending on the thermo-mechanical state. Thermal conductivity of the original SMPU foam was increased from 0.061 to 0.074 W/m·K by compressing the SMPU foam and the thermal conductivity of the compressed SMPU foam was decreased to 0.063 W/m·K after heated to T_{tr} . The thermal resistance is associated with the heat flux through a unit area of a sample due to temperature difference between two surfaces. Therefore, the thermal resistance of the SMPU foam is affected significantly by the thickness of a specimen. The equation for the thermal resistance is given by the following equation [33].

$$R = \frac{\Delta T}{q} = \frac{L}{k} \quad (3.1.7)$$

where ΔT represents the temperature difference between the hot and the cold surfaces, q is the heat flux, k is the thermal conductivity, and L is the thickness of the sample. The thermal resistance of the SMPU foam was decreased to 0.04 m²·K/W when the SMPU foam was compressed by loading. After shape recovery of the SMPU foam, the thermal resistance of the SMPU foam was increased to 0.22 m²·K/W, a value very similar to that of the original SMPU foam. The thermal resistance of the SMPU foam showed an opposite behavior to the thermal conductivity.

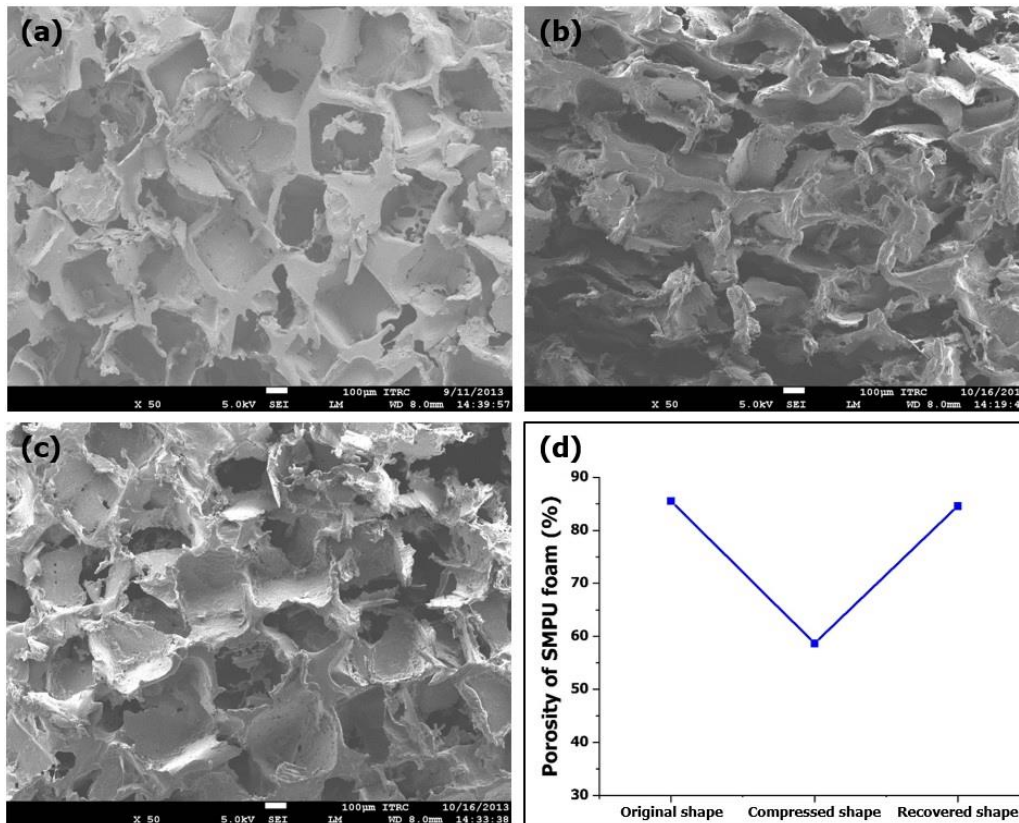


Figure 3.1.7. (a)-(c) SEM images of SMPU foam-400: (a) original, (b) compressed, and (c) recovered states, (d) porosity of SMPU foam-400 in the thermo-mechanical cycle, and (e) thermal conductivity and thermal resistance of SMPU foam-400 in the thermo-mechanical cycle.

3.1.5. Summary

Dual scale shape memory foams were prepared in this study by using the salt leaching method. We demonstrated that the mechanical and thermal properties of the hybrid foams were enhanced significantly due to the synergistic effect. The thermal conductivity of SMPU foams was modelled and compared with experimental results. Thermo-mechanical features of the SMPU foam were also investigated. Thermal conductivity of the SMPU foam was decreased with decrease in the pore size of the foam and such decrease in the pore size lead to increase in the mechanical properties of SMPU foams. All SMPU foam specimens exhibited high shape recovery of 98 %. The hybrid SMPU foam with dual scale pore sizes of 100 and 400 μm showed low thermal conductivity of 0.047 W/m·K. In particular, it provided a superior specific compressive stress due to the low slenderness ratio and synergistic effect. A fabrication method was proposed in this study for production of dual scale hybrid foams which had low thermal conductivity and high compressive stress with shape memory features.

3.1.6. Supplementary Information

3.1.6.1. Numerical simulation

Two different unit cells of SMPU foam specimens were modelled schematically in the 3D mode as shown in figure S3.1.4 to simulate the dynamic behavior of SMPU foam. The plane stress condition was employed in the simulation. The following governing equation was used:

$$\begin{aligned} -\nabla \sigma &= \mathbf{F} \\ \mathbf{S} - \mathbf{S}_0 &= \mathbf{C} : (\boldsymbol{\varepsilon} - \boldsymbol{\varepsilon}_0 - \boldsymbol{\varepsilon}_{inel}) \\ \boldsymbol{\varepsilon} &= \frac{1}{2} \left[(\nabla \mathbf{u})^T + \nabla \mathbf{u} + (\nabla \mathbf{u})^T \nabla \mathbf{u} \right] \end{aligned}$$

where σ is the Cauchy stress, \mathbf{F} is the deformation gradient, \mathbf{S} is the second Piola-Kirchhoff stress, \mathbf{C} is the elasticity tensor, $\boldsymbol{\varepsilon}$ is the Green strain, $\boldsymbol{\varepsilon}_0$ is the initial strain, $\boldsymbol{\varepsilon}_{in}$ is the inelastic strain, and $\nabla \mathbf{u}$ is the displacement gradient. The material properties were determined by experiments. For boundary conditions, a compressive stress was applied to the right side (yz-plane) of the unit cell of SMPU foam, and the left side (yz-plane) was fixed in all directions. The other 4 sides were considered symmetric.

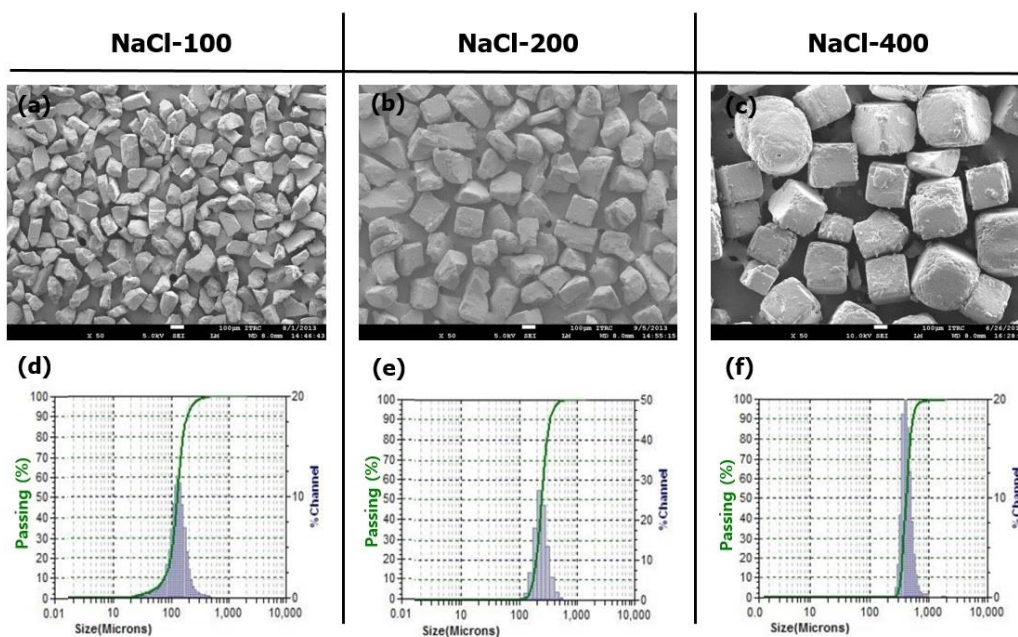


Figure S3.1.1. SEM images of the filtered NaCl particles: sintered glass filter size of (a) 100, (b) 200, and (c) 400 μm and particle size distribution of the filtered NaCl particles. Average particle size of the NaCl was (d) 127.5, (e) 242, and (f) 413.8 μm .

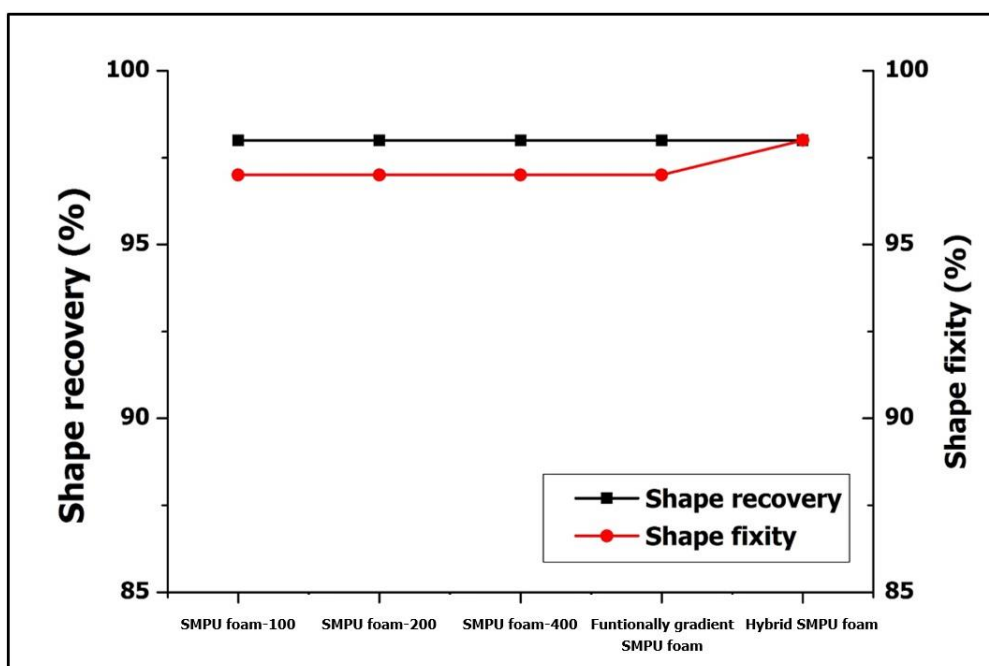


Figure S3.1.2. Shape recovery and shape fixity of SMPU foam specimens.

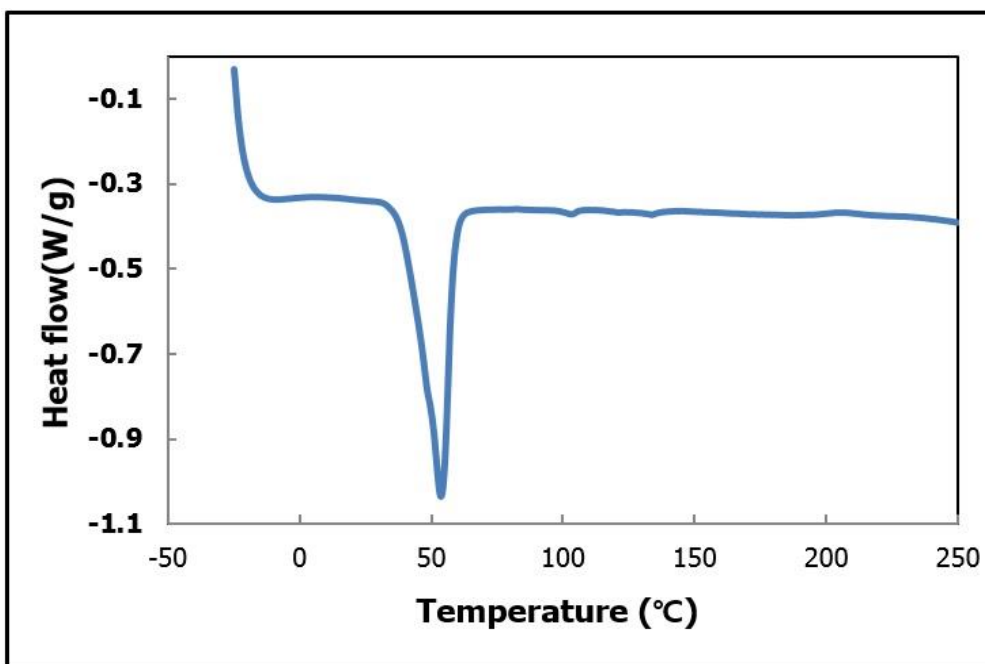


Figure S3.1.3. DSC result of the synthesized SMPU.

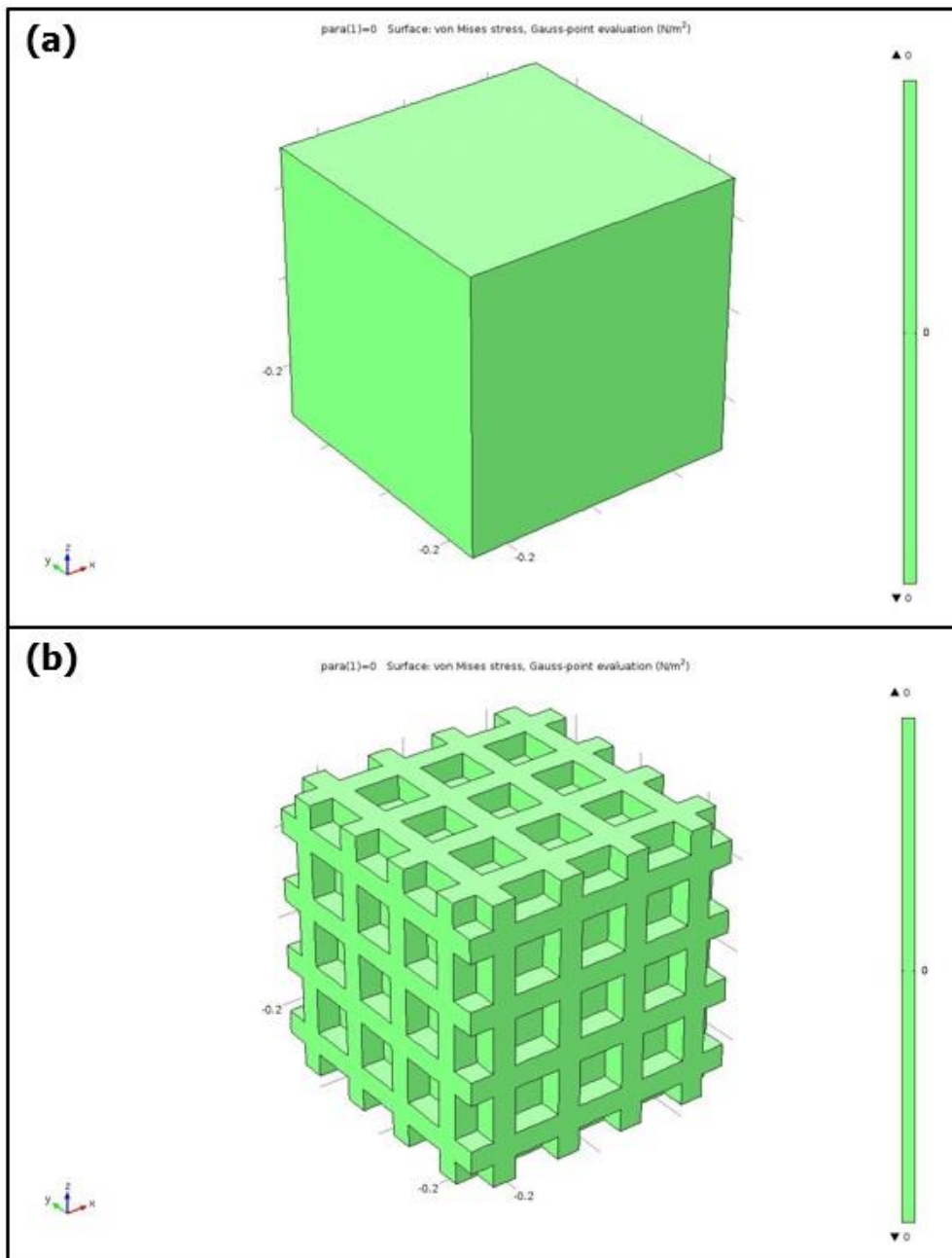


Figure S3.1.4. 3D unit cell images (a) SMPU foam-400, and (b) hybrid SMPU foam.

3.1.7. References

- [1] Gibson L, Ashby M. Cellular solids: structure and properties. Cambridge university press 1999.
- [2] Li W, Ryan A, Meier I. Effect of chain extenders on the morphology development in flexible polyurethane foam. *Macromolecules* 2002, 35, 6306.
- [3] Metcalfe A, Desfaits A, Salazkin I, Yahia L, Sokolowski W, Raymond J. Cold hibernated elastic memory foams for endovascular interventions. *Biomaterials* 2003, 24, 491.
- [4] Kagami Y, Gong J, Osada Y. Shape memory behaviors of crosslinked copolymers containing stearyl acrylate. *Macromolecular rapid communications* 1996, 17, 539.
- [5] Lendlein A, Jiang H, Jünger O, Langer R. Light-induced shape-memory polymers. *Nature* 2005, 434, 879.
- [6] Scott T, Schneider A, Cook W, Bowman C. Photoinduced plasticity in cross-linked polymers. *Science* 2005, 308, 1615.
- [7] Schmidt A. Electromagnetic activation of shape memory polymer networks containing magnetic nanoparticles. *Macromolecular Rapid Communications* 2006, 27, 1168.
- [8] Razzaq M, Anhalt M, Frommann L, Weidenfeller B. Thermal, electrical and magnetic studies of magnetite filled polyurethane shape memory polymers. *Materials Science and Engineering: A* 2007, 444, 227.
- [9] Lv H, Leng J, Liu Y, Du S. Shape-memory polymer in response to solution. *Advanced Engineering Materials* 2008, 10, 592.
- [10] Liu Y, Lv H, Lan X, Leng J, Du S. Review of electro-active shape-memory polymer composite. *Composites Science and Technology* 2009, 69, 2064.
- [11] Gall K, Dunn M, Liu Y, Finch D, Lake M, Munshi N. Shape memory polymer nanocomposites. *Acta Materialia* 2002, 50, 5115.
- [12] Lendlein A, Kelch S. Shape-memory polymers. *Angewandte Chemie International Edition* 2002, 41, 2034.
- [13] Behl M, Razzaq M, Lendlein A. Multifunctional Shape-Memory Polymers.

Advanced materials 2010, 22, 3388.

[14] Luo X, Mather P. Triple-Shape Polymeric Composites (TSPCs). *Advanced Functional Materials* 2010, 20, 2649.

[15] Wei Z, Sandström R, Miyazaki S. Shape-memory materials and hybrid composites for smart systems: Part I Shape-memory materials. *Journal of Materials Science* 1998, 33, 3743.

[16] Otsuka K, Wayman C. *Shape memory materials*. Cambridge University Press 1999.

[17] Dunand D, Müllner P. Size Effects on Magnetic Actuation in Ni-Mn-Ga Shape-Memory Alloys. *Advanced Materials* 2011, 23, 216.

[18] Lee B.S, Chun B. C, Chung Y. C, Sul K. I, Cho J. W. Structure and thermomechanical properties of polyurethane block copolymers with shape memory effect. *Macromolecules* 2001, 34, 6431.

[19] Zhang C, Ni Q, Fu S, Kurashiki K. Electromagnetic interference shielding effect of nanocomposites with carbon nanotube and shape memory polymer. *Composites Science and Technology* 2007, 67, 2973.

[20] Gunes I, Jimenez G, Jana S. Carbonaceous fillers for shape memory actuation of polyurethane composites by resistive heating. *Carbon* 2009, 47, 981.

[21] Yao H, Ge J, Wang C, Wang X, Hu W, Zheng Z, Ni Y, Yu S. A flexible and highly pressure-sensitive graphene–polyurethane sponge based on fractured microstructure design. *Advanced Materials* 2013, 25, 6692.

[22] Hu W, Koberstein J. The effect of thermal annealing on the thermal properties and molecular weight of a segmented polyurethane copolymer. *Journal of Polymer Science Part B: Polymer Physics* 1994, 32, 437.

[23] Lin J, Chen L. Study on shape-memory behavior of polyether-based polyurethanes. I. Influence of the hard-segment content. *Journal of applied polymer science* 1998, 69, 1563.

[24] D'hollander S, Van Assche G, Van Mele B, Du Prez F. Novel synthetic strategy toward shape memory polyurethanes with a well-defined switching temperature. *Polymer* 2009, 50, 4447.

- [25] Ferrigno T. Rigid plastics foams. Vol 2: Reinhold Pub. Corp. 1967.
- [26] Koo M. S, Chung K, Youn J. R. Reaction injection molding of polyurethane foam for improved thermal insulation. *Polymer Engineering & Science* 2001, 41, 1177.
- [27] Thirumal M, Khastgir D, Singha N, Manjunath B, Naik Y. Effect of foam density on the properties of water blown rigid polyurethane foam. *Journal of applied polymer science* 2008, 108, 1810.
- [28] Mikos A, Sarakinos G, Leite S, Vacant J, Langer R. Laminated three-dimensional biodegradable foams for use in tissue engineering. *Biomaterials* 1993, 14, 323.
- [29] Glicksman L, Schuetz M, Sinofsky M. Radiation heat transfer in foam insulation. *International journal of heat and mass transfer* 1987, 30, 187.
- [30] Han Z, Fina A. Thermal conductivity of carbon nanotubes and their polymer nanocomposites: a review. *Progress in polymer science* 2011, 36, 914.
- [31] Pak S. Y, Kim H. M, Kim S. Y, Youn J. R. Synergistic improvement of thermal conductivity of thermoplastic composites with mixed boron nitride and multi-walled carbon nanotube fillers. *Carbon* 2012, 50, 4830.
- [32] Rusch K. Load-compression behavior of flexible foams. *Journal of Applied Polymer Science* 1969, 13, 2297.
- [33] Chen Q, Ren J. Generalized thermal resistance for convective heat transfer and its relation to entransy dissipation. *Chinese Science Bulletin* 2008, 53, 3753.
- [34] Li F, Hou J, Zhu W, Zhang X, Xu M, Luo X, Ma D, Kim B. K. Crystallinity and morphology of segmented polyurethanes with different soft-segment length. *Journal of applied polymer science* 1996, 62, 631.
- [35] Kim H. D, Lee T. J, Huh J. H, Lee D. J. Preparation and properties of segmented thermoplastic polyurethane elastomers with two different soft segments. *Journal of applied polymer science* 1999, 73, 345.
- [36] Ratna D, Karger-Kocsis J. Recent advances in shape memory polymers and composites: a review. *Journal of Materials Science* 2008, 43, 254.
- [37] Skochdopole R. Environmental factors in thermal conductivity of plastics foams. *Modern plastics*, 1962.
- [38] Placido E, Arduini-Schuster M, Kuhn J. Thermal properties predictive model for

insulating foams. *Infrared physics & technology* 2005, 46, 219.

[39] Glicksman L, Torpey M. The influence of cell size and foam density on the thermal conductivity of foam insulation. *Polyurethanes World Congress*, Germany, 1987.

[40] Kuhn J, Ebert H, Arduini-Schuster M, Büttner D, Fricke J. Thermal transport in polystyrene and polyurethane foam insulations. *International journal of heat and mass transfer* 1992, 35, 1795.

[41] T. Jones. The effect of thickness and temperature on heat transfer through foamed polymers. In Peter Koestenbaum (ed.) 1968.

3.2. Shape memory polyurethane foams embedded CNTs and their remote shape control induced microwave radiation

3.2.1. Introduction

As shape memory polymers (SMPs) are being emerged as smart polymers, SMPs have received a significant attention recently because of their fascinating properties, such as a wide temperature range for shape recovery (-30 ~ 70 °C), high shape recoverable strain (up to 1000 %), easy processing conditions and low cost [1, 2]. SMPs have very high potential for applications in civil, medical and industrial applications because they can be deformed in response to external stimuli, such as light, heat, pH, electric and magnetic fields [3-8].

Various responsive manners, which were generated by electric and magnetic energy, have been developed by convenient methods. However, their further application in certain environments can be strongly limited because a direct contact between the polymer and electrode is required [6]. On the other hand, it is reported that microwaves are considered as a non-contact actuator of SMPs. In comparison with other electromagnetic waves, microwaves possess better penetrability due to the long wavelength and enable a response to SMPs without considerable heat loss because of the low attenuation degree during transportation. Since pure SMPs have no response in microwaves, appropriate microwave energy absorbers are required to fabricate thermal responsive SMPs from a distance. Shape memory effects induced microwave radiation are proposed by Du et al. and Xu et al., and water molecules and T-ZnOw nanoparticles have been demonstrated to be good microwave energy absorbers [9, 10]. Some ferroelectric nanoparticles such as BaTiO₃ and reinforcements for polymer composites have been applied to improve the microwave properties and potential shape memory effects of SMPs [11-14]. Carbon nanotubes (CNTs) are suitable as the fillers due to their superb electrical, mechanical properties, and strong microwave absorbing capacity. Several composites and blends including CNTs show the excessive heating effect by strong absorption of microwaves [15, 16]. Under vacuum, CNTs can be

heated to a temperature of 1550 °C in a 700 W, 2.45 Hz microwave field. K. R. Paton et al. have contributed to this topic experimentally by adding as little as 0.04 wt% CNTs into the silicone oil for enhancement of microwave absorbance [17]. Bulk ceramic/CNT composites are proposed by A. L. Higginbotham et al. to demonstrate rapid initial heating rates [18].

In this study, shape memory polyurethane (SMPU) foams were prepared with various CNTs weight fractions in order to control the remote actuation of SMPU foams by microwave radiation. Experimental analysis for thermal and mechanical responses of the SMPU foams was carried out by adding small amount of CNTs. Effects of the CNTs on shape memory behavior of the SMPU foams were investigated and the results were explained in terms of the good infrared absorption and reflectivity of the CNTs.

3.2.2. Experimental Section

3.2.2.1. Synthesis of SMPU

Poly(ϵ -caprolactone)diol (PCL, Perstorp) and 4,4'-Methylenebis(phenyl isocyanate) (MDI, JUNSEI) were mixed in a four neck cylindrical flask with continuous mechanical stirring under nitrogen atmosphere at 80 °C for 3h to react each other. 1,4-Butanediol (BD, DAEJUNG) was chosen as a chain extender to control the degree of polymerization. The SMPU resin fabricated by prepolymerization method was dried at room temperature under vacuum to evaporate the solvent and hardened further at 100 °C in an oven for morphological stabilization.

3.2.2.2. Fabrication of SMPU/CNT foam

The manufacturing process for the SMPU/CNT foam is described schematically in figure 3.2.1. Tetrahydrofuran (THF, DAEJUNG) was used as a solvent to dissolve the SMPU resins and a 25 wt% solution of SMPU in THF was prepared. Sodium chloride (NaCl, DAEJUNG) particles were added to the SMPU solution at a volume ratio of 8 to 10. The SMPU foam materials with different concentrations (0.01 wt%, 0.05 wt% and 0.1 wt%) of carbon nanotubes (CNTs, Hanhwa chemical) were prepared for our study. The CNTs were mixed with the SMPU/NaCl solution with continuous mechanical stirring. In order to disperse CNTs well, the SMPU/NaCl/CNT suspension was treated by ultrasonic excitation for 1 h. The mixture of SMPU/NaCl/CNT was placed in a vacuum oven to completely remove the air bubble and THF at 40 °C for 3 days. SMPU/NaCl/CNT composite were immersed in deionized (DI) water to fabricate the foam structure by leaching NaCl particles. The SMPU/CNT foams with pore size of 300 μm were prepared by drying at room temperature for 2 days.

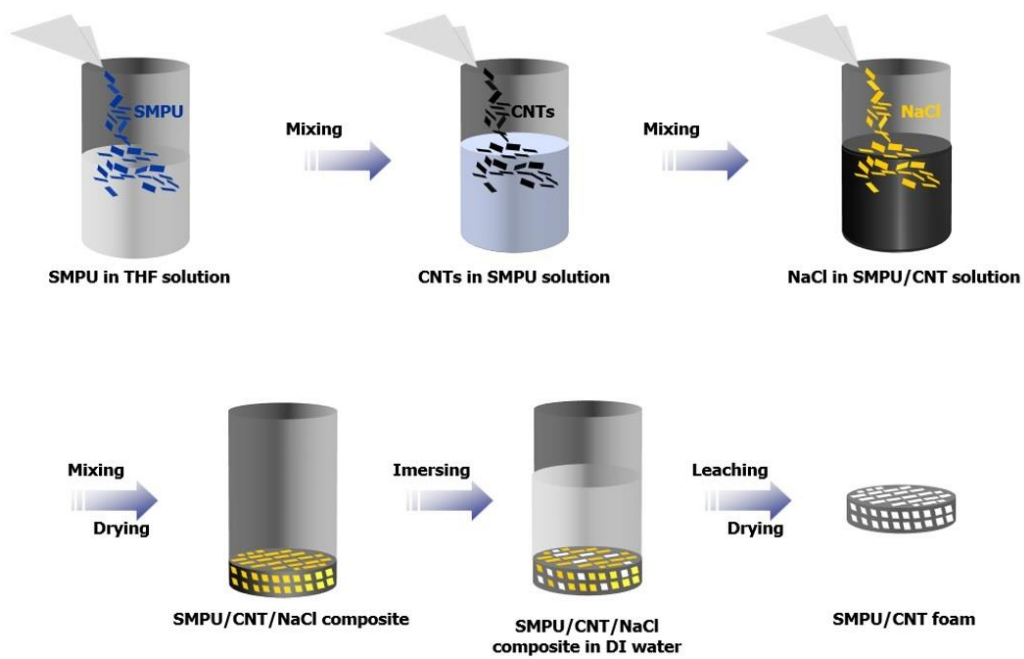


Figure 3.2.1. Processing procedure for preparation of SMPU/CNT foams.

3.2.2.3. Structural Characterization

The surfaces of the SMPU/CNT foam specimens were coated with platinum for 300 s using a sputter coating machine (Sputter Coater-108, Cressinton Scientific Instruments, Watford, UK). The fractured surfaces of the SMPU/CNT foams were observed with a field emission scanning electron microscopes (FE-SEM, JSM-7600F, JEOL) to examine the internal structure of SMPU/CNT foam.

3.2.2.4. Thermal Characterization

The transition temperature (T_{tr}) of the samples was measured with a differential scanning calorimeter (DSC, 200 F3 Maia, Netzsch) from -20 to 250 °C at a heating rate of 10 °C/min. Thermogravimetric analysis (TGA, Q-5000 IR, USA) of the specimens was carried out from 0 to 700 °C at a heating rate of 10 °C/min under a nitrogen flow. Thermal conductivity of the specimens was measured by using a thermal analyzer (C-Therm TCi, C-THERM, New Brunswick, Canada) based on the modified transient plane source (MTPS) method. A small amount of heat at the interface between the sensor and the foam heat was generated by applying an electric current to the heating part of a sensor, and a temperature was risen by about 2 °C. Rising temperature at the interface could provoke a voltage drop in the sensor element. The thermal conductivity was calculated by measuring the rate of increase in sensor voltage and the range of measurable thermal conductivity of the apparatus is from 0 to 100 W/m·K.

3.2.2.5. Mechanical Characterization

Thermo-mechanical tests were carried out with universal testing machine (UTM, WL2100, WITHLAB) to investigate the compressive stress of the SMPU/CNT foam. The specimens were compressed through the loading and unloading processes under a constant strain rate at a constant temperature.

3.2.2.6. Shape Memory Characterization

In order to demonstrate the shape memory properties of the SMPU/CNT foams by microwave radiation, the specimens were prepared with a size of 35 (diameter) \times 20 (thickness) mm². A microwave field was exposed by an altered microwave oven due to its convenience. The output of microwave power was controlled to 200 W with a frequency of 2.45 GHz. A visual infrared thermometer was used to measure the temperature distribution. Before investigating the shape recovery test, the specimen was heated at a temperature of 80 °C and compressed to 80 % of its original thickness with a crosshead speed of 10 mm/min. The specimen was cooled down to 20 °C and then maintained at the temperature for 10 min after the removal of the load. The specimen was exposed by microwave radiation for 5 min and maintained for 10 min. The shape recovery and shape fixity are obtained by using the following equations.

$$\text{Shape recovery (\%)} = \frac{\varepsilon_m - \varepsilon_r}{\varepsilon_m} \times 100 \quad (3.2.1)$$

$$\text{Shape fixity (\%)} = \frac{\varepsilon_f}{\varepsilon_m} \times 100 \quad (3.2.2)$$

where ε_m = strain at an 80 % compression, ε_r = recovered strain after microwave exposure, and ε_f = strain before microwave exposure.

3.2.3. Results and Discussion

Thermal conductivity is the most important property of thermal insulation foams. Figure 3.2.2 shows thermal conductivity of the SMPU/CNT foams with respect to the CNT content. It is inferred that the thermal conductivity of the SMPU foam without CNTs was measured to 0.04864 W/m·K, then the thermal conductivities of the SMPU foams were decreased from 0.04463 to 0.04361 W/m·K as the contents of CNTs were ranged from 0.01 to 0.1 wt%. The drop in thermal conductivity of SMPU/CNT foam may be due to reduction in radiative heat transfer by CNTs [19]. The mechanisms associated with heat transfer in plastic foams are well known and documented by many researchers [19, 20]. The effective thermal conductivity of polymer foams is composed of contributions from various mechanisms of heat transfer such as conduction, convection and radiation. For polymer foams with small cells, the convection contribution to thermal conductivity can be neglected [21, 22]. As a result, the overall thermal conductivity of polymer foams is given by the following equation.

$$k = k_s + k_g + \frac{16\sigma T^3}{3\varepsilon} \quad (3.2.3)$$

where k_s is the conduction through the cell wall and the solid struts, k_g is the conduction through the gas phase, σ is the Stefan-Boltzmann constant, ε is the extinction coefficient, and T is temperature. Thus, the thermal conductivity of polymer foams is mainly determined by the combination of conduction and radiation [23]. Compared to pure SMPU foam, the addition of CNTs may slightly increase k_s because the CNTs have very high thermal conductivity. However, when the CNTs are added very small amount such as 0.01 wt%, 0.05 wt%, and 0.1 wt%, carbonaceous materials such as graphite, graphene and CNTs have been shown to decrease the radiative heat transfer in PU foams by absorbing and reflecting the infrared radiation instead of transmitting the heats [24]. Therefore, thermal conductivities of the SMPU foams including low concentrations of CNTs were decreased compared to that of the pure

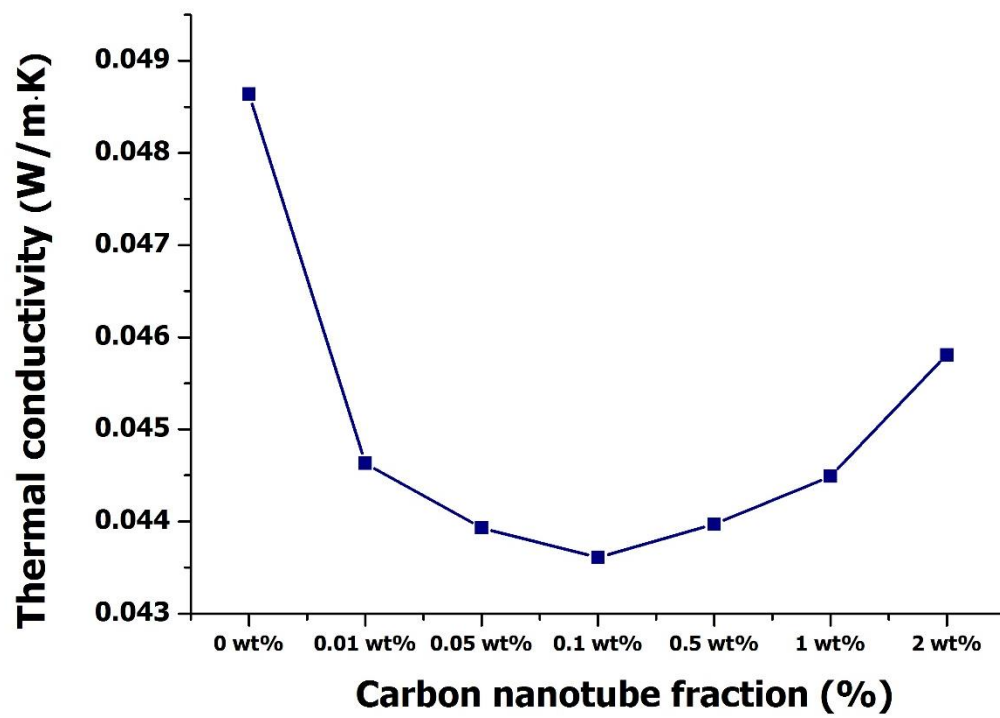


Figure 3.2.2. Thermal conductivity of SMPU foams as a function of CNTs weight fraction.

SMPU foam because the passage of infrared radiation through the foam was decreased.

The morphologies of the SMPU/CNT foams manufactured by leaching NaCl particles are shown in figure 3.2.3. It can be observed that the pore size of the SMPU/CNT foam was consistent with the particle size of NaCl. The porosities of SMPU/CNT foams were in the range from 89 to 90 % with respect to the CNT weight fraction. As shown in figure 3.2.3(c), the CNTs were exhibited a relatively well dispersion and embedded CNTs could be led to absorb or reflect the microwave energy in the SMPU foams.

The thermal behavior of the SMPU/CNT foams obtained by the thermogravimetric analysis is shown in figure 3.2.4. Since the well-dispersed CNTs might have restricted the thermal motion of PU chains and diffusion of volatile decomposition products, the thermal stability of the SMPU foam was enhanced by CNTs, which could slightly improve the thermal decomposition temperature of SMPU foams [25, 26].

As shown in figure 3.2.5, a significant improvement of mechanical properties for SMPU foams reinforced by CNTs was observed from the compressive test. This indicates that the enhancement of interfacial bonding between polymer and CNTs can be led to increase the normalized Young's modulus of SMPU/CNT foams [27, 28].

The T_{tr} of SMPs refers to the switching temperature at which the modulus of SMPs significantly decreases and shows the shape memory effect. Therefore, the T_{tr} of SMPs plays on important factor to investigate shape memory properties such as shape recovery and shape fixity. Figure 3.2.6 shows the T_{tr} of the SMPU foams with respect to the CNT weight fraction. Results of endothermic peak of SMPU foams displayed a range of T_{tr} values from 49.6 to 47.3 °C as the amount of CNTs increased from 0.01 to 0.1 wt%. Previous studies have reported the relation between the transition temperature and effect of CNTs. Results of the DSC analysis can be also explained by the relative motion of macromolecule segment which affects the T_{tr} .

Figure 3.2.7(a) shows the thermo-physical features of SMPU foams embedded CNTs. The drastic improvement in temperature was observed for the SMPU foam containing 0.1 wt% CNTs due to the microwave absorbance. Microwave energy

yielded by CNTs can be transformed into thermal energy to heat the SMPU foam volumetrically [29, 30]. The shape recovery and shape fixity of the SMPU/CNT foams are demonstrated in figure 3.2.7(b). The shape recovery of the SMPU/CNT foam induced by microwave radiation ranged from 78 to 84 % and shape fixity of the SMPU/CNT foam was higher than 94 %.

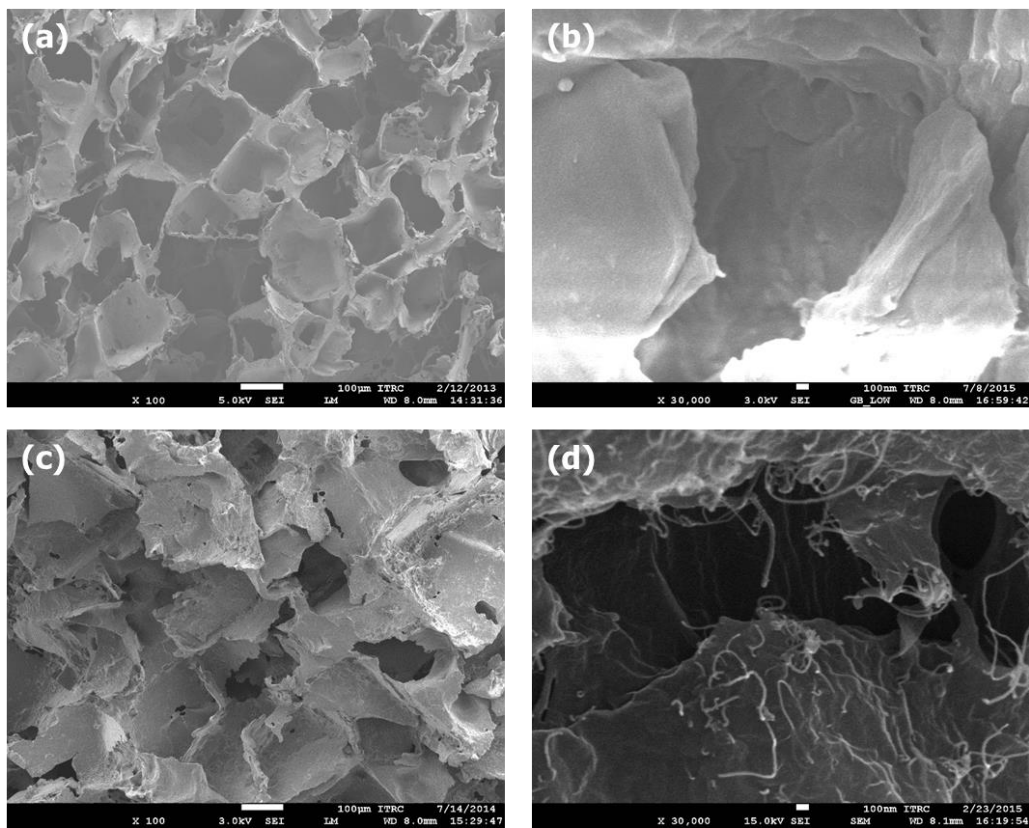


Figure 3.2.3. SEM images of SMPU/CNT foam specimens: (a), (b) raw SMPU foam, (c) and (d) SMPU foam with 0.1 wt% of CNTs.

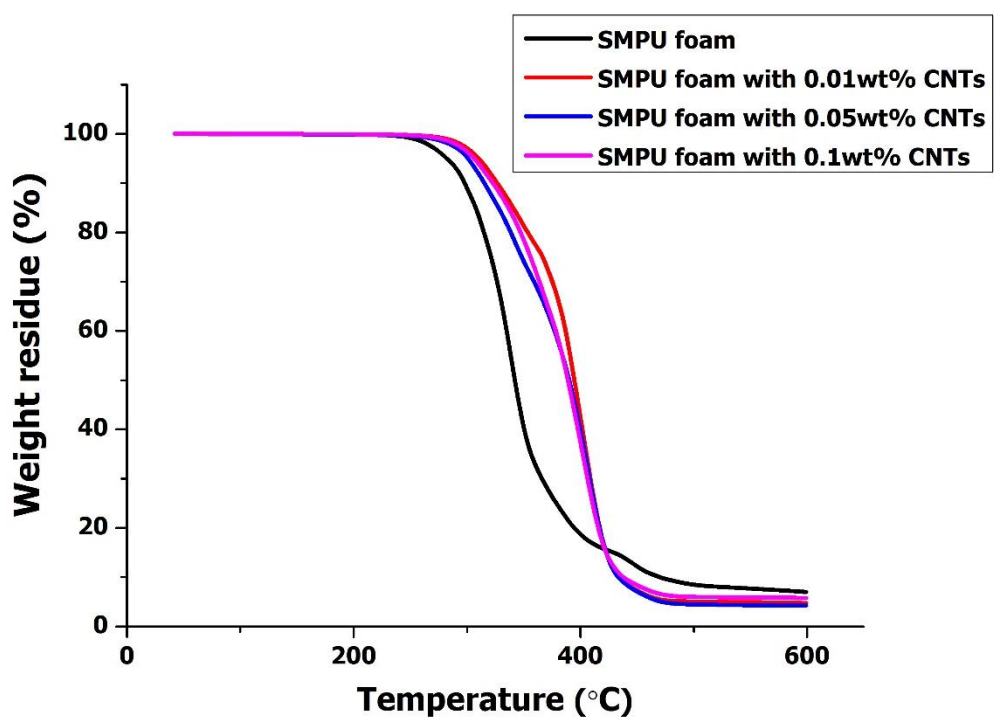


Figure 3.2.4. Thermogravimetric analysis curves for the SMPU/CNT foams with respect to CNTs weight fraction.

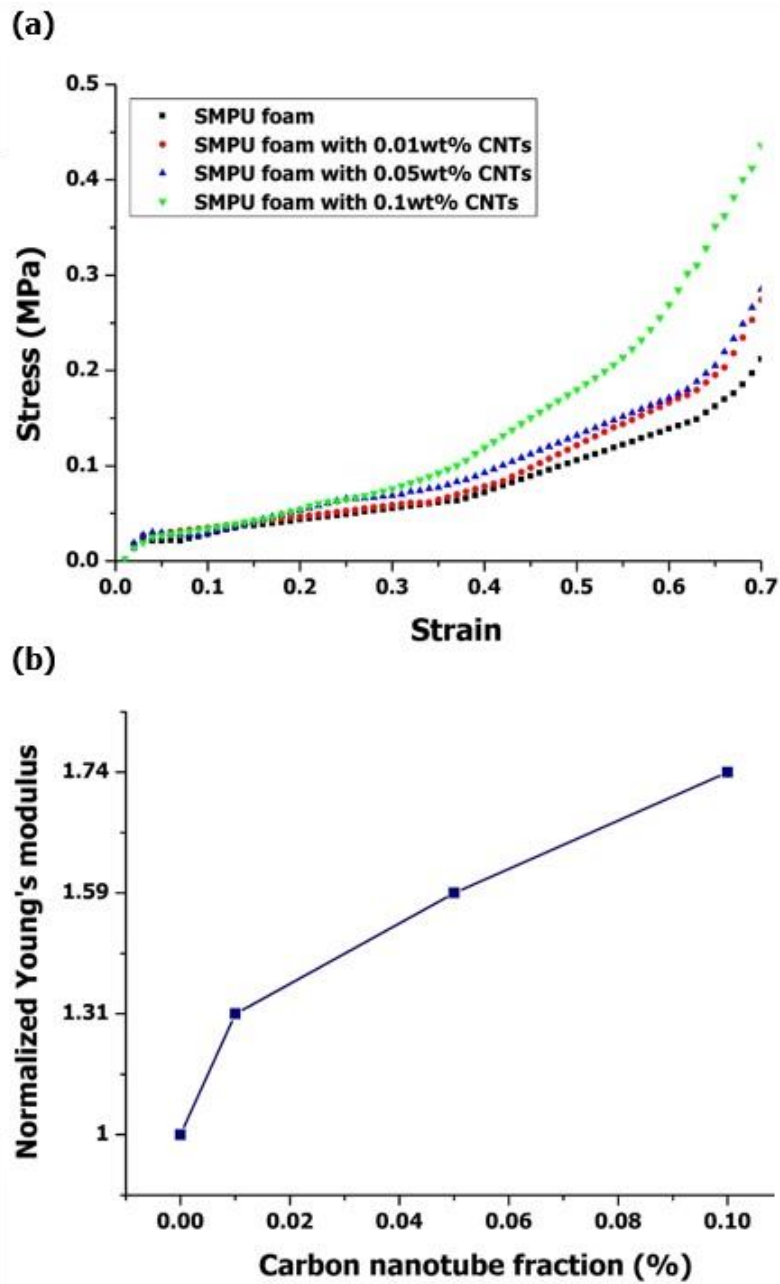


Figure 3.2.5. (a) Compressive stress-strain curves of SMPU/CNT foams, and (b) normalized Young's moduli of SMPU foams as a function of CNTs weight fraction.

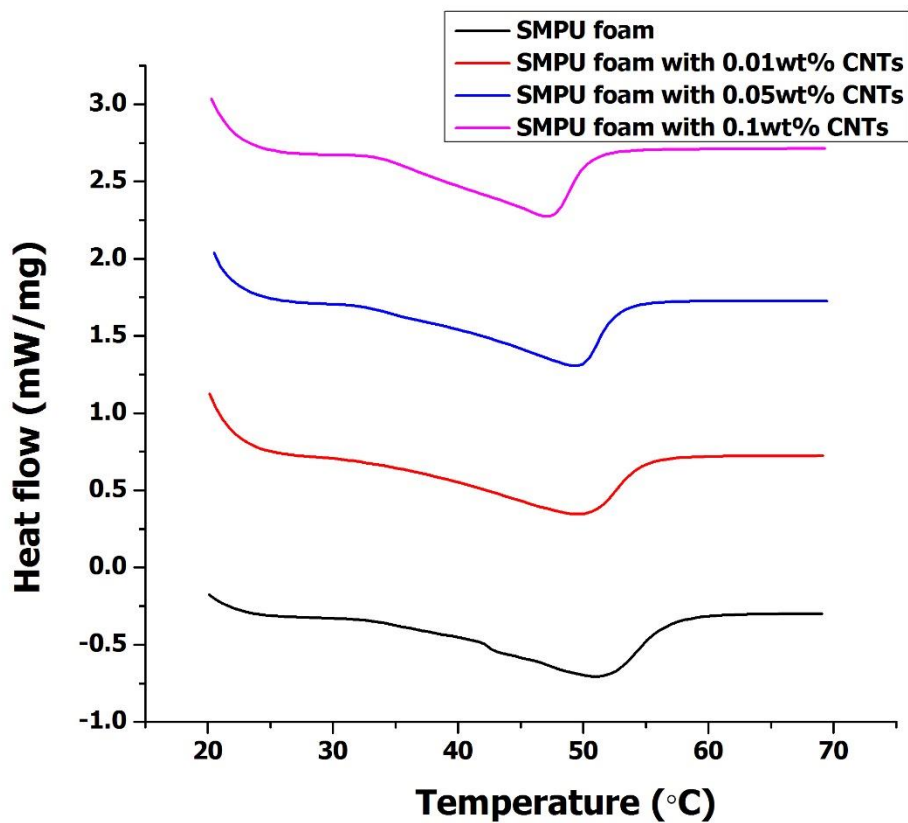


Figure 3.2.6. DSC results of the SMPU foams as a function of CNTs weight fraction.

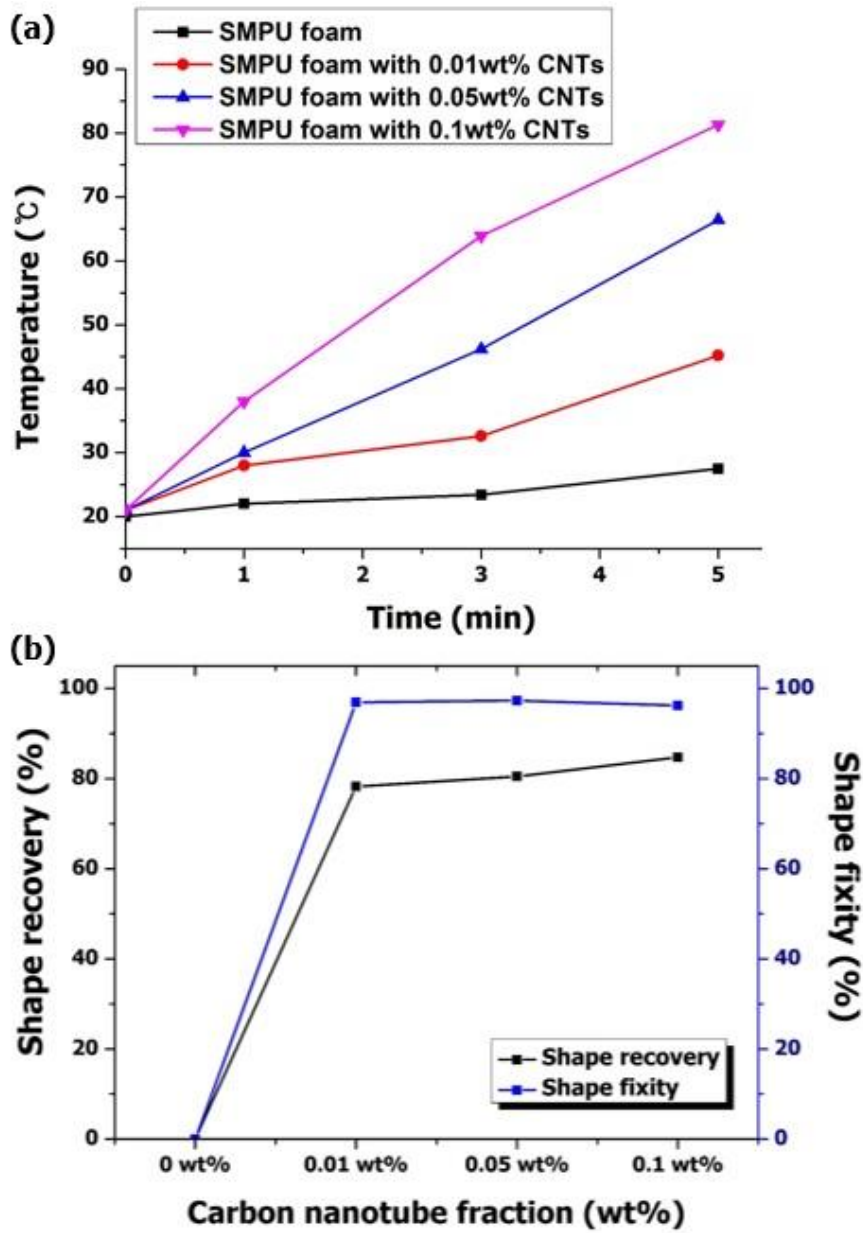


Figure 3.2.7. (a) Temperature versus time for the SMPU/CNT foams with microwave radiation, and (b) shape recovery and shape fixity of SMPU foam specimens as a function of CNTs weight fraction.

3.2.4. Summary

Shape memory foams embedded CNTs were prepared in this study by using the salt leaching method. Results from the thermal and mechanical measurements displayed that the thermal insulation properties of SMPU foams were enhanced by adding CNTs due to microwave absorption and thermo-mechanical properties of SMPU foams were also improved significantly with increase of the CNT content from 0 to 0.1 wt%. Moreover, the thermogravimetric investigation exhibited that the thermal stability of SMPU foams was developed along with the addition of CNTs. All SMPU foams embedded CNTs were well-triggered by microwave exposure and represented high shape recovery of 84% by absorption of microwave radiation. The SMPU foam with 0.1 wt% CNTs showed low thermal conductivity of 0.04361 W/m·K and superior compressive stress due to the low infrared radiation transmitted through the foam and high interfacial bond. We demonstrated that the composition of internal structure and appropriate weight fraction of the CNTs in the SMPU foams were important factors determining the thermal insulation and mechanical properties of SMPU foams. Overall, this study was proposed the fascinating method for fabrication of SMPU/CNT foams which provided low thermal conductivity and high compressive stress with remote shape control.

3.2.5. References

- [1] Lan X, Liu Y, Lv H, Wang X, Leng J, Du S. Fiber reinforced shape-memory polymer composite and its application in a deployable hinge. *Smart Materials and Structures* 2009, 18, 024002.
- [2] Ahmad M, Luo J, Xu B, Purnawali H, King P, Chalker P, Fu Y, Huang W, MirafTAB M. Synthesis and Characterization of Polyurethane-Based Shape-Memory Polymers for Tailored T_g around Body Temperature for Medical Applications. *Macromolecular Chemistry and Physics* 2011, 212, 592-602.
- [3] Huang W, Yang B, An L, Li C, Chan Y. Water-driven programmable polyurethane shape memory polymer: demonstration and mechanism. *Applied Physics Letters* 2005, 86, 114105.
- [4] Lendlein A, Jiang H, Jünger O, Langer R. Light-induced shape-memory polymers. *Nature* 2005, 434, 879-882.
- [5] Scott T, Schneider A, Cook W, Bowman C. Photoinduced plasticity in cross-linked polymers. *Science* 2005, 308, 1615-1617.
- [6] Schmidt A. Electromagnetic activation of shape memory polymer networks containing magnetic nanoparticles. *Macromolecular Rapid Communications* 2006, 27, 1168-1172.
- [7] Lu H, Liu Y, Gou J, Leng J, Du S. Electroactive shape-memory polymer nanocomposites incorporating carbon nanofiber paper. *International Journal of Smart and Nano Materials* 2010, 1, 2-12.
- [8] Leng J, Lan X, Liu Y, Du S. Shape-memory polymers and their composites: stimulus methods and applications. *Progress in Materials Science* 2011, 56, 1077-1135.
- [9] Zhihong X, Yao Z. MICROWAVE ACTIVATED SHAPE MEMORY POLYMER.
- [10] Du H, Yu Y, Jiang G, Zhang J, Bao J. Microwave-Induced Shape-Memory Effect of Chemically Crosslinked Moist Poly (vinyl alcohol) Networks. *Macromolecular Chemistry and Physics* 2011, 212, 1460-1468.
- [11] Li J, Claude J, Norena-Franco L, Seok S. I, Wang Q. Electrical energy storage in ferroelectric polymer nanocomposites containing surface-functionalized BaTiO₃

- nanoparticles. *Chemistry of Materials* 2008, 20, 6304-6306.
- [12] Ohlan A, Singh K, Chandra A, Dhawan S. Microwave absorption properties of conducting polymer composite with barium ferrite nanoparticles in 12.4-18 GHz. *Applied Physics Letters* 2008, 93, 053114-053114-053113.
- [13] Guo Z, Lee S. E, Kim H, Park S, Hahn H, Karki A, Young D. Fabrication, characterization and microwave properties of polyurethane nanocomposites reinforced with iron oxide and barium titanate nanoparticles. *Acta Materialia* 2009, 57, 267-277.
- [14] Morales C, Dewdney J, Pal S, Skidmore S, Stojak K, Srikanth H, Weller T, Wang J. Tunable magneto-dielectric polymer nanocomposites for microwave applications. *Microwave Theory and Techniques, IEEE Transactions on* 2011, 59, 302-310.
- [15] Saito R, Dresselhaus G, Dresselhaus M. *Physical properties of carbon nanotubes*. World Scientific 1998.
- [16] Vázquez E, Prato M. Carbon nanotubes and microwaves: interactions, responses, and applications. *ACS Nano* 2009, 3, 3819-3824.
- [17] Walton D, Boehnel H, Dunlop D. Response of magnetic nanoparticles to microwaves. *Applied physics letters* 2004, 85, 5367-5369.
- [18] Higginbotham A, Moloney P, Waid M, Duque J, Kittrell C, Schmidt H, Stephenson J, Arepalli S, Yowell L, Tour J. Carbon nanotube composite curing through absorption of microwave radiation. *Composites Science and Technology* 2008, 68, 3087-3092.
- [19] Glicksman L. Heat transfer in foams. In *Low density cellular plastics*. Springer 1994, 104-152.
- [20] Schuetz M, Glicksman L. A basic study of heat transfer through foam insulation. *Journal of Cellular Plastics* 1984, 20, 114-121.
- [21] Suh K. *Polystyrene and structural foam*. Polymeric Foams, Oxford University Press 1991, 151.
- [22] Modesti M, Lorenzetti A, Dall'Acqua C. New experimental method for determination of effective diffusion coefficient of blowing agents in polyurethane foams. *Polymer Engineering & Science* 2004, 44, 2229-2239.
- [23] Glicksman L, Torpey M. The influence of cell size and foam density on the

thermal conductivity of foam insulation. In Polyurethanes World Congress, Germany, 1987, 80-84.

[24] Almanza O, Rodríguez-Pérez M, De Saja J. Prediction of the radiation term in the thermal conductivity of crosslinked closed cell polyolefin foams. *Journal of Polymer Science Part B: Polymer Physics* 2000, 38, 993-1004.

[25] AngeláRodríguez-Perez, M, de Saja J, AngeláLopez-Manchado M. Functionalized graphene sheet filled silicone foam nanocomposites. *Journal of Materials Chemistry* 2008, 18, 2221-2226.

[26] Yan D, Dai K, Xiang Z, Li Z, Ji X, Zhang W. Electrical conductivity and major mechanical and thermal properties of carbon nanotube-filled polyurethane foams. *Journal of applied polymer science* 2011, 120, 3014-3019.

[27] Bernal M, Lopez-Manchado M., Verdejo R. In situ foaming evolution of flexible polyurethane foam nanocomposites. *Macromolecular Chemistry and Physics* 2011, 212, 971-979.

[28] Verdejo R, Mar Bernal M, Romasanta L, Tapiador F, Lopez-Manchado M. Reactive nanocomposite foams. *Cellular Polymers* 2011, 30, 45.

[29] Jordan C, Galy J, Pascault J, Moré C, Delmotte M, Jullien H. Comparison of microwave and thermal cure of an epoxy/amine matrix. *Polymer Engineering & Science* 1995, 35, 233-239.

[30] Nightingale C, Day R. Flexural and interlaminar shear strength properties of carbon fibre/epoxy composites cured thermally and with microwave radiation. *Composites Part A: Applied Science and Manufacturing* 2002, 33, 1021-1030.

IV. ZnO/GO/PET film

4.1. Hydrodynamic fabrication of structurally gradient ZnO nanorods

4.1.1. Introduction

Structurally or functionally gradient nanomaterials have received increasing attention in advanced materials engineering due to their fascinating advantages stemming from optimum material design and fabrication. Precise manipulation of such nanostructures is, therefore, critical to materialize the superior characteristics in various applications such as electronics, biology, optics, energy, and chemistry. In particular, a lot of efforts have been made to fabricate structurally gradient materials (SGM) with help of physical stimuli such as heat, concentration, and electromagnetic field. Among nanomaterials, zinc oxide (ZnO) is known as a material capable of forming abundant configurations of nanostructures including nanowires, nanorods, nanotubes, and nanoflakes [1-5]. Since ZnO has a direct wide band gap of 3.4 eV at room temperature (RT) with the capability of emitting light in the ultraviolet spectral region and a large exciton binding energy of 60 meV, it can be used for high efficiency ultraviolet (UV) optoelectronic devices and light emitting diodes (LEDs) [6, 7]. ZnO possesses the piezoelectric effect due to its non-centrosymmetric structure [8]. Moreover, ZnO can be directly applied to biosensor because of its bio-safeness and biocompatibility [9]. Several methods, such as vapor–liquid–solid growth with metal catalysts, metal-organic chemical vapor deposition (MOCVD), and pulsed laser deposition (PLD), have been developed for synthesizing 1D ZnO nanostructures [10-13]. However, they require a high temperature ranging from 400 °C to 600 °C and complex procedures [14-16]. Furthermore, ZnO nanorods with high quality can be grown only on expensive substrates such as GaN or Al₂O₃ using the heteroepitaxy method [17, 18]. Recently, it

is reported that the hydrothermal method can fabricate diverse shapes of ZnO nanostructures at a low temperature with large areal uniformity [19, 20]. For instance, the change in temperature and concentration of the nutrient solution allows one to control the morphology and density of ZnO nanorods [21-23]. However, the influence of other external factors generated by rotating the Si wafer and the physics behind such a fabrication process under shear stress onto the Si wafer are still not fully understood.

In this study, we propose a novel hydrothermal fabrication method of ZnO nanorods to develop structurally gradient nanostructures using the effect of shear stress. The hydrodynamics based method can act as a robust and powerful platform for controlling the dimension and orientation of nanostructures in a facile, systematic manner. The effect of shear stress on the structural properties of ZnO nanorods is investigated experimentally and theoretically. Transport phenomena of momentum and mass in the rotating fluid are analyzed through numerical simulation.

4.1.2. Experimental Section

Si wafers with a size of 4 inch were used as the substrate for the deposition of ZnO nanocrystals. Before the ZnO nanocrystals were deposited on the substrate, the Si wafers were cleaned using sulfuric acid (H_2SO_4) and hydrogen peroxide (H_2O_2) and then etched with 5% hydrogen fluoride (HF). For the pre-treatment of substrate, Si wafers were ultra-sonicated consecutively in acetone, ethanol, isopropyl alcohol (IPA), and de-ionized (DI) water each for 10 min. The wafers were dried in nitrogen gas and baked in an oven at 200 °C for 5 min to remove adsorbed moisture. ZnO seeds were prepared into 10 mM zinc acetate ($\text{Zn}(\text{C}_2\text{H}_3\text{O}_2)_2$) dissolved in ethanol solution at 60 °C for 5 min. The ZnO seed layer was deposited for several times onto the Si wafer by spin casting at a spin rate of 1000 rpm for 10 s and 3000 rpm for 20 s. Thereafter, the wafers were dried in room temperature and annealed at 250 °C for 10 min to evaporate a residual solvent and form crystal seeds. Then, the Si substrate was immersed upside down in the aqueous solution consisting of 25 mM zinc nitrate hexahydrate ($\text{Zn}(\text{NO}_3)_2 \cdot 6\text{H}_2\text{O}$), 25 mM hexamethylenetetramine ($\text{C}_6\text{H}_{12}\text{N}_4$, HMT) and DI water. During the rotation of the Si substrate in the growth solution at a spin rate of 100 rpm, ZnO nuclei on the surface of the Si substrate were affected by applied shear stress in this stage. ZnO nanorods were grown by the constant supply of zinc ions and hydroxyl radicals in the growth solution while ZnO seeds were deformed by shear fluid. The principal growth of ZnO nanorods was carried out at 90 °C for 2 h. Finally, the Si substrate was rinsed with DI water for several times and dried at 90 °C for several hours. The surface morphology of ZnO nanocrystals was characterized through field emission scanning electron microscopy (FE-SEM). The X-ray diffraction (XRD) measurement was performed on a Rigaku D/Max diffractometer with Cu K α radiation to determine the structure of the ZnO nanorod arrays.

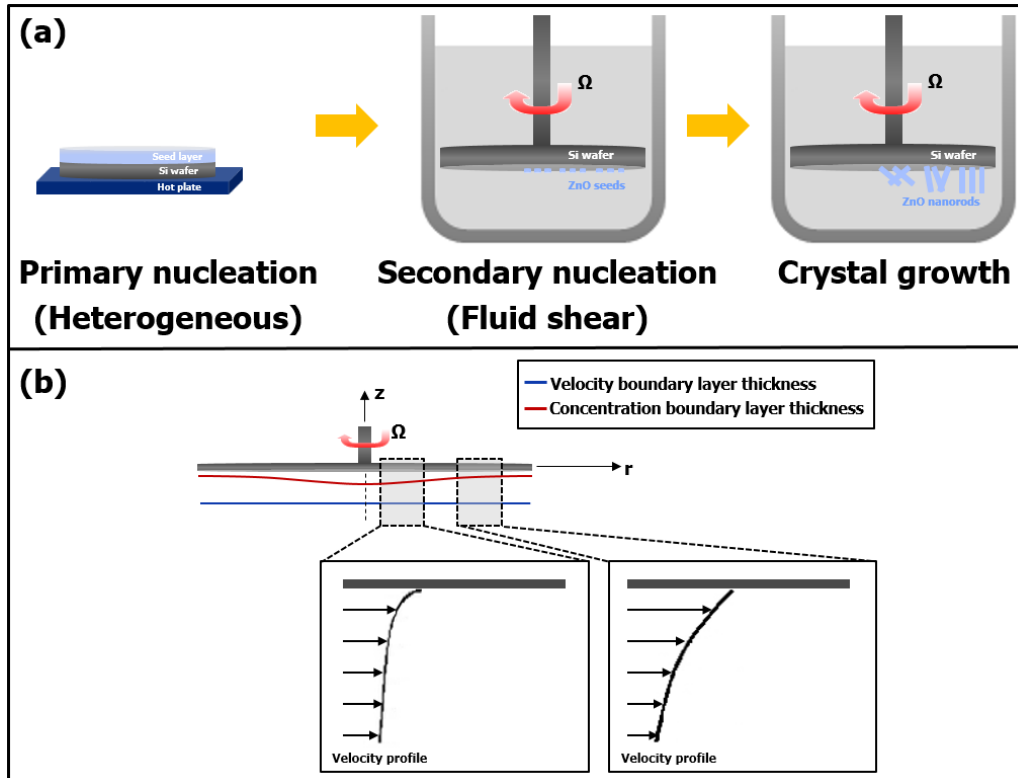


Figure 4.1.1. Schematic diagrams of (a) the experimental procedures for the primary nucleation of ZnO seeds by heterogeneous nucleation, the secondary nucleation of ZnO nuclei by shear flow, and the growth of ZnO nanorods under shear stress and (b) a conceptual model of velocity boundary thickness and concentration boundary layer thickness developed by shear stress.

4.1.3. Results and Discussion

The fabrication process of ZnO nanorods is described schematically in figure 4.1.1(a). First, ZnO seeds are formed on the Si substrate for the primary nucleation, and the heterogeneous nucleation of ZnO occurs on the Si substrate. The heterogeneous nucleation is more likely to happen than the homogenous nucleation since it requires a relatively lower activation energy barrier. Moreover, the interfacial energy between crystals and substrates is usually smaller than that between crystals and solutions [24, 25]. Therefore, the heterogeneous nucleation takes place at a lower saturation ratio onto a substrate than the homogeneous nucleation. Without rotating the Si wafer, epitaxial crystal growth occurs from the generated nuclei along the direction of crystallization. Indeed, a condensed phase of single-crystalline rods perpendicular to the substrate is obtained if the concentration of precursor is high. However, the shear stress applied by rotating the Si wafer in the growth solution leads to the secondary nucleation. As a result, the ZnO nanostructure including dimension, orientation, and density is controlled by the shear stress developed during the nanowire formation process. The resulting nucleation phenomenon can be explained using a shear-induced nucleation theory [26]. The hydrodynamic forces determines the secondary nucleation generation by applying the shear stress to the seed crystal surface. This indicates that the orientation of ZnO nanorods is determined depending on the magnitude of the applied hydrodynamic forces. The change in the Gibbs free energy ΔG associated with the nucleation process is considered as follows [27, 28].

$$\Delta G = 4\pi r^2 \gamma + \frac{4}{3} \pi r^3 \Delta G_v \quad (4.1.1)$$

where ΔG_v is the free energy change of the transformation per unit volume, r is the radius of the spherical nucleus, and γ is the interfacial tension. The shear stress induced nucleation can be described using the cell stretch model to investigate the effect of shear stress on the secondary nucleation procedure and orientation of ZnO nanorod

[29]. Since nuclei with the critical radius r_c are affected by shear flow, some nucleation sites can be expanded under shear stress. According to Hinch and Acrivos, the critical radius is given by[30]

$$\frac{r_c}{r^*} = 3.45Ca^{\frac{1}{2}} = 3.45\left(\frac{\eta\dot{\gamma}r^*}{\gamma}\right)^{\frac{1}{2}} \quad (4.1.2)$$

where Ca is the capillary number (i.e., the ratio of viscous force to interfacial tension), η is the viscosity, $\dot{\gamma}$ is the shear rate, and r^* is the modified radius under shear stress. Now, let us define the critical radius under shear stress as $r_c^* = (\gamma/\eta)^{1/3}(r_c/3.45)^{2/3}$. The critical free energy of formation can be re-expressed as below.

$$\Delta G'_{crit} = \frac{4\pi\gamma r_c^{*2}}{3} = \frac{4\pi\gamma}{3} \left(\frac{\gamma}{\eta\dot{\gamma}}\right)^{\frac{2}{3}} \left(\frac{r_c}{3.45}\right)^{\frac{4}{3}} \quad (4.1.3)$$

Under shear stress, the nucleation rate (e.g. the number of nuclei formed per unit time per unit volume), is given by

$$\frac{dN}{dt} = N_0 e^{-\frac{\Delta G'_{crit}}{kT}} \quad (4.1.4)$$

where N_0 is the total number of available nucleation sites, k is the Boltzmann constant, and T is the solution temperature. Equation (4.1.3) suggests that the critical free energy required for nucleation is reduced significantly as the shear rate is increased. Therefore, the density of nucleation is increased by applying the shear stress because the nucleation rate is increased. Large ZnO seeds can be formed offering an excess of nucleation position after annealing. The interactive effect among ZnO nanorods is

inevitable during the growth process. As a result, ZnO nanorods can be grown densely and vertically at the edge of the Si substrate due to the high density of nucleation [31].

The fluid flow arising from the rotation of the Si wafer is a determinant for the dimensions of ZnO nanorods because it influences the momentum and mass transfer associated with the ZnO nucleation and growth [32]. The principal flows and relevant boundary layers are depicted in figure 4.1.1(b). In this study, the fluid flow is regarded as a rotationally symmetric and steady flow. The dimensionless variables such as the dimensionless axial location and the dimensionless radial velocity component are introduced as $z^*=z(\Omega/\nu)^{1/2}$, $u_r^*(z^*)=u_r/r\Omega$, $u_\phi(z^*)=u_\phi/r\Omega$, $u_z^*(z^*)=u_z/(\nu\Omega)^{1/2}$, and $p^*(z^*)=-p/\mu\Omega=-p/\rho\nu\Omega$ [33].

Using appropriate parameters, the continuity equation and the Navier-Stokes equations can be cast as the following forms.

$$\frac{du_{z^*}}{dz^*} + 2u_{r^*} = 0 \quad (4.1.5)$$

$$\frac{d^2u_{r^*}}{dz^*{}^2} - u_{z^*} \frac{\partial u_{r^*}}{\partial z^*} - u_{r^*}^2 + u_{\phi^*}^2 = 0 \quad (4.1.6)$$

$$\frac{d^2u_{\phi^*}}{dz^*{}^2} - u_{z^*} \frac{du_{\phi^*}}{dz^*} - 2u_{r^*}u_{\phi^*} = 0 \quad (4.1.7)$$

$$\frac{d^2u_{z^*}}{dz^*{}^2} - u_{z^*} \frac{\partial u_{z^*}}{\partial z^*} - \frac{\partial p^*}{\partial z^*} = 0 \quad (4.1.8)$$

The boundary conditions were applied as $u_r^*=0$, $u_\phi^*=1$, $u_z^*=0$, and $p^*=0$ at $z^*=0$ and $u_r^*=0$ and $u_\phi^*=0$ at $z^*=\infty$.

According to the von Karman's similarity solution for the free disc, the velocity boundary layer thickness, defined as the axial distance from the rotating wafer, can be estimated by solving $u_\phi=0.01r\Omega$ [34]. This indicates that $u_\phi^*=u_\phi/\Omega r=0.01$ which

corresponds to a value for z^* of about 5.5. As a result, the following relationship for a laminar boundary layer thickness δ on the Si substrate is obtained [33].

$$\delta \approx 5.5 \sqrt{\frac{v}{\Omega}} \quad (4.1.9)$$

The concentration boundary thickness is usually defined as the axial distance from the rotating wafer where the absolute concentration is less than 99% of the far field concentration, that is, $[(C_{A,S}-C_A)/(C_{A,S}-C_{A,\infty})]=0.99$ [35]. As shown in figure 4.1.1(b), the concentration boundary thickness decreases with respect to the radial location of the Si substrate. Since the concentration boundary layer thickness at the tip of the Si substrate is relatively thinner than that at the center of the Si substrate, the convection mass transfer at the edge of the Si substrate is more active than that at the center of the Si substrate [36-37]. In this sense, even a small difference in surface flow can change the dimensions of the ZnO nanorods dramatically.

The velocity profile, nucleation density, and concentration distribution induced by shear stress were predicted by carrying out finite element (FE) simulation (Figure. 4.1.2). As illustrated by the simulation results shown in figures 4.1.2(a) and 4.1.2(b), the local shear rate is maximized at the edge of the Si substrate because the velocity magnitudes on the surface of the Si substrate increased gradually as approaching the edge of the Si substrate. Consequently, the normalized nucleation density of ZnO nanorods at the edge of the Si substrate is higher than that at other sites of the Si substrate, as observed in the thermodynamic analysis presented above. From these results, it is noticed that the gradient of ZnO nanorods is related to the density of nucleation. The fluid velocity can be coupled to a convection-diffusion phenomenon to describe the reaction rate during the growth of ZnO nanorods in the nutrient solution. The variation of concentration at the local position of the Si substrate is depicted in figure 4.1.2(e). In figure 4.1.2(f), the concentration boundary layer thickness decreased along in the radial direction. Overall, the ZnO nanorods located at the edge of the Si substrate is the largest since the convective mass transfer at the edge of the Si substrate is highest.

The SEM images show the ZnO nanorods grown on the Si substrate to illustrate the effect of shear stress. As shown in figures 4.1.3(a)-3(c), the ZnO nanorods were distributed randomly over the entire region of the Si substrate without shear stress. Figures 4.1.3(d)-3(f) show the SEM images of ZnO nanorods prepared at a spin rate of 100 rpm. In contrast to the orientation of the ZnO nanorods at the center of the Si substrate, the ZnO nanorods were found to have vertical orientation near the edge of the Si substrate. That is, structurally gradient nanostructures were fabricated by changing the hydrodynamic condition. The XRD patterns for the different location of the Si substrate for the growth of ZnO nanorods are shown in figure 4.1.4. Figure 4.1.4(a) shows the XRD pattern of the grown ZnO nanorods on the center of the Si substrate and all diffraction peaks can be indexed to wurtzite structure of ZnO such as (100) and (101) peaks. We can see that when the effect of shear stress onto the Si substrate increases, the (002) diffraction peak is intense gradually and other diffraction peaks disappear as shown in figure 4.1.4(c). It indicates that the fabricated ZnO nanorods are highly oriented along the c-axis. Also, the diameter of the ZnO nanorods at the end of the Si substrate was larger than that at the center of the Si substrate. As shown in figure 4.1.5, the denser ZnO nanorods leads to more vertical orientation of the nanostructure, which is consistent with the previous theoretical prediction based on the density of ZnO nanorods. In addition, the average diameter of ZnO nanorods increased from 32 to 59 nm under the applied shear stress.

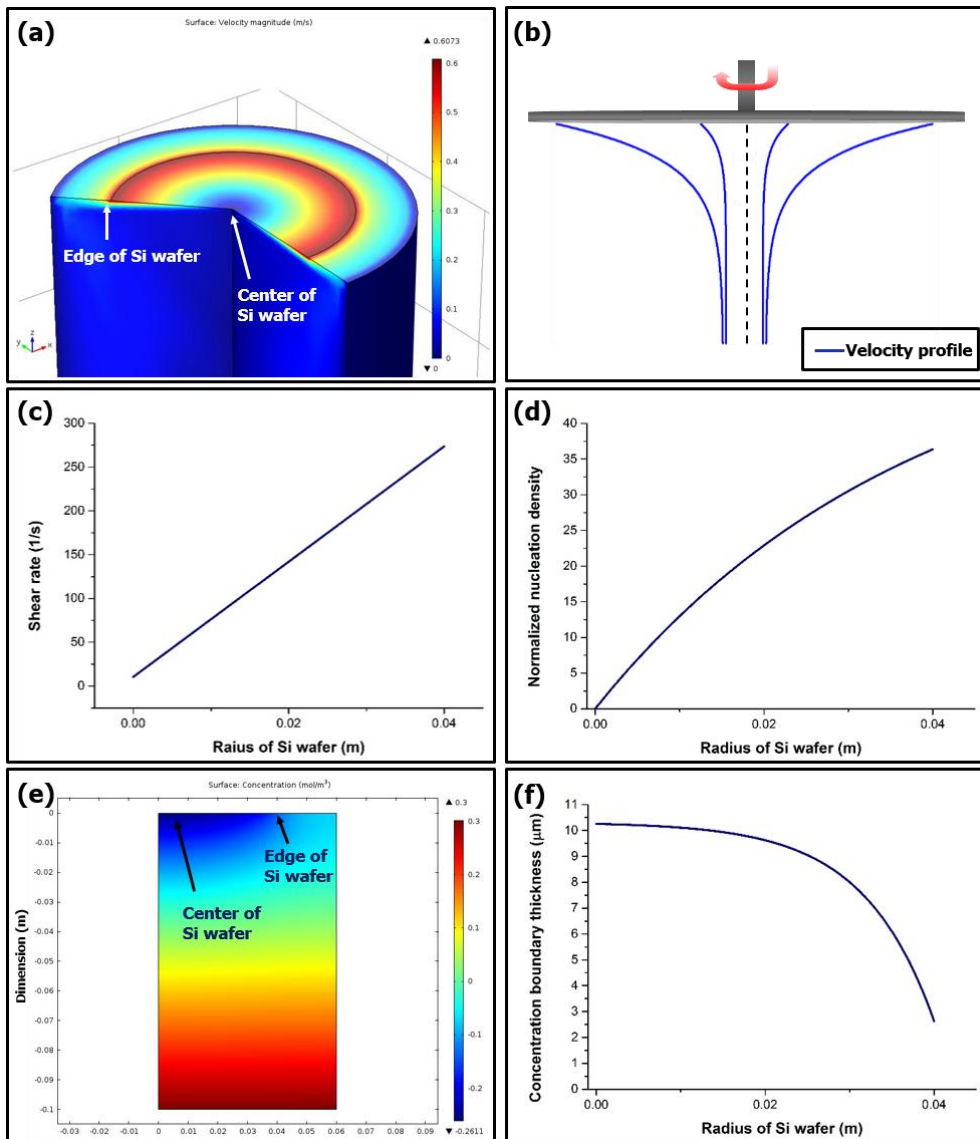


Figure 4.1.2. Simulation results: (a) 3 dimensional velocity field, (b) velocity profiles in the rotating flow, (c) shear rate as a function of the radius of Si substrate, (d) predicted normalized nucleation density of ZnO nanorods, (e) concentration distribution, and (f) predicted concentration boundary layer thickness as a function of the radius of Si substrate.

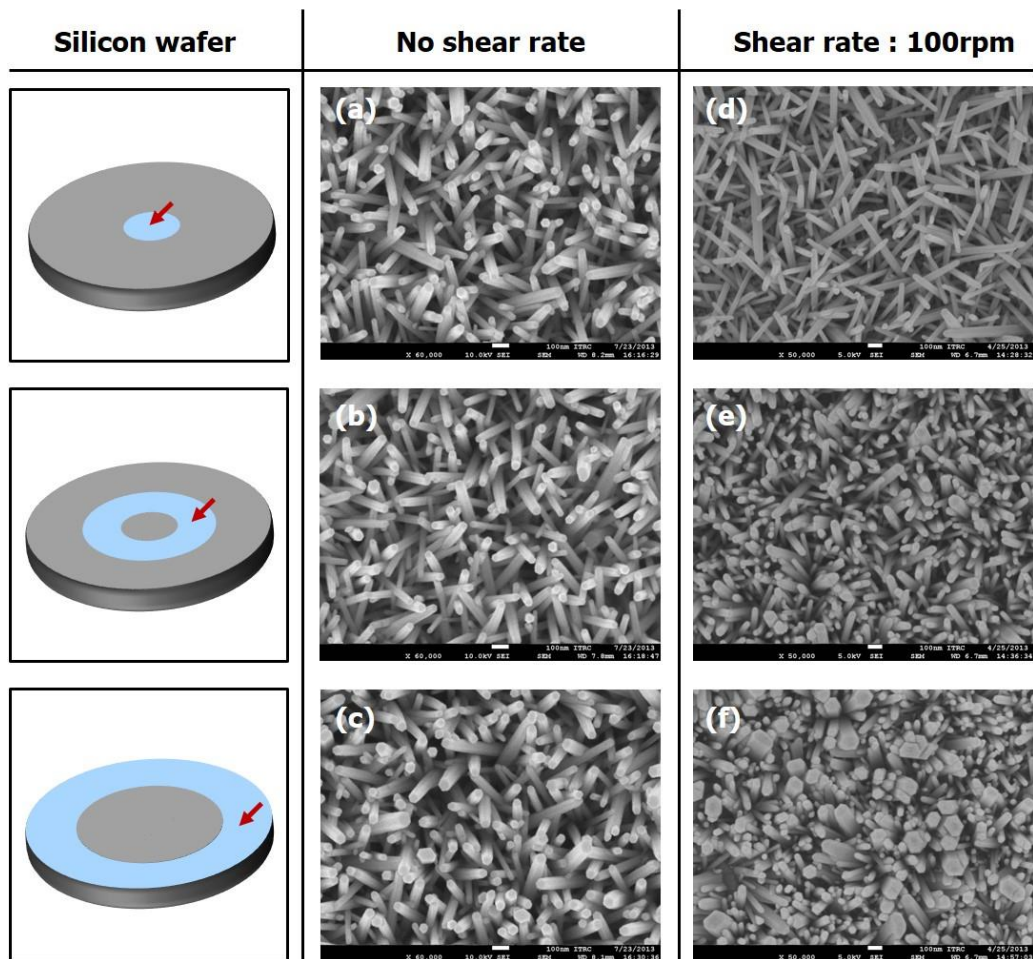


Figure 4.1.3. SEM images of the ZnO nanorods grown: the case without shear stress at (a) the center, (b) center-periphery, and (c) edge of Si substrate and the case with shear stress at (d) the center, (e) center-periphery, and (f) edge of Si substrate.

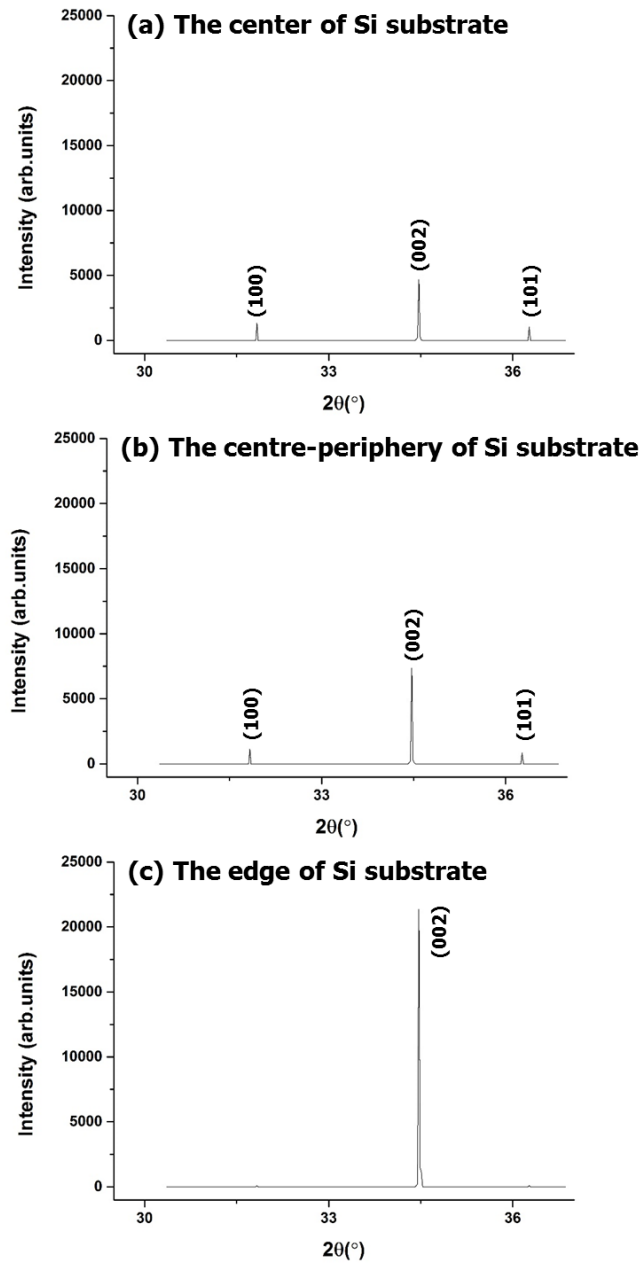


Figure 4.1.4. XRD patterns of ZnO nanorods grown at (a) the center, (b) centre-periphery, and (c) edge of Si substrate

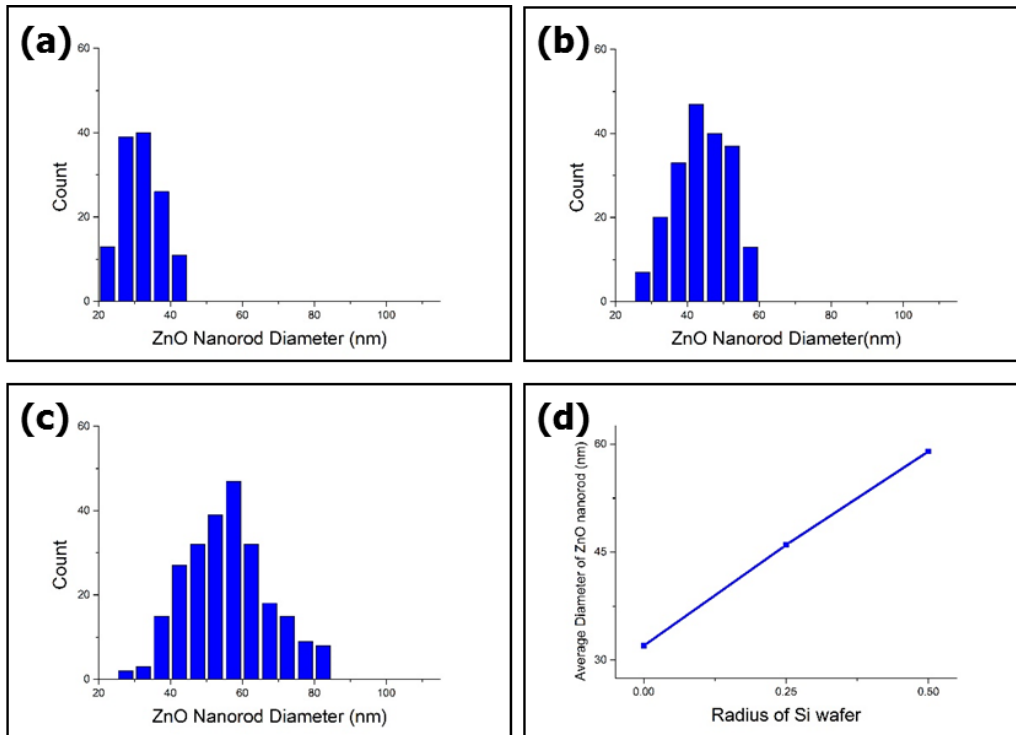


Figure 4.1.5. Diameter histograms of the ZnO nanorods grown under shear stress at (a) the center of Si substrate, (b) centre-periphery of Si substrate, and (c) edge of Si substrate and (d) correlation between the average diameter of ZnO nanorods and the radius of Si wafer.

4.1.4. Summary

Structurally gradient nanorods of ZnO were synthesized using hydrodynamics of a rotating fluid. We demonstrated that the orientation and dimensions of ZnO nanorods are significantly affected by the applied shear stress. To understand the effect of the shear stress on the fabrication of ZnO nanorods, theoretical and numerical analyses were conducted. The density of ZnO nanorods was found to increase with increasing the shear stress on the substrate surface. The change in the concentration boundary layer thickness on the surface leads to different dimensions of the ZnO nanorods formed. Overall, this study is expected to provide a powerful method for fabricating structurally gradient nanostructure in a very effective way based on the understanding of the physics associated with nanomaterial engineering and hydrodynamics.

4.1.5. Supplementary Information

4.1.5.1. Numerical simulation

To simulate the dynamic behavior of ZnO nanoparticles in a beaker, we assume that the fluid flow is incompressible and described by the Navier-Stokes equation as follow.

$$\rho \frac{\partial \mathbf{u}}{\partial t} + \rho (\mathbf{u} \cdot \nabla) \mathbf{u} = \nabla \cdot \left[-p\mathbf{I} + \mu (\nabla \mathbf{u} + (\nabla \mathbf{u})^T) \right] + \mathbf{F}$$

$$\nabla \cdot \mathbf{u} = 0$$

where \mathbf{u} is the velocity, ρ is the density, μ is the dynamic viscosity, and p is the pressure. The volumetric force component \mathbf{F} is zero. The free surface condition at $z=0$ is assumed to be stress free and all internal surfaces are taken to have a no-slip condition. The velocity components in the angular direction is equal to the angular velocity, Ω , times the radius, r . During the simulation for growth control of ZnO nanorods with shear stress, an initial angular velocity is set to be 100 rpm. It can be coupled with a mass transport convection-diffusion equation to describe the flux of ZnO nanoparticles. The conservative formulation of the convective term is given as below.

$$\frac{\partial c}{\partial t} + \nabla \cdot (c\mathbf{u}) = \nabla \cdot (D\nabla c) + R$$

where D is the diffusion coefficient, R is a consumption rate expression, and \mathbf{u} is the solvent velocity field.

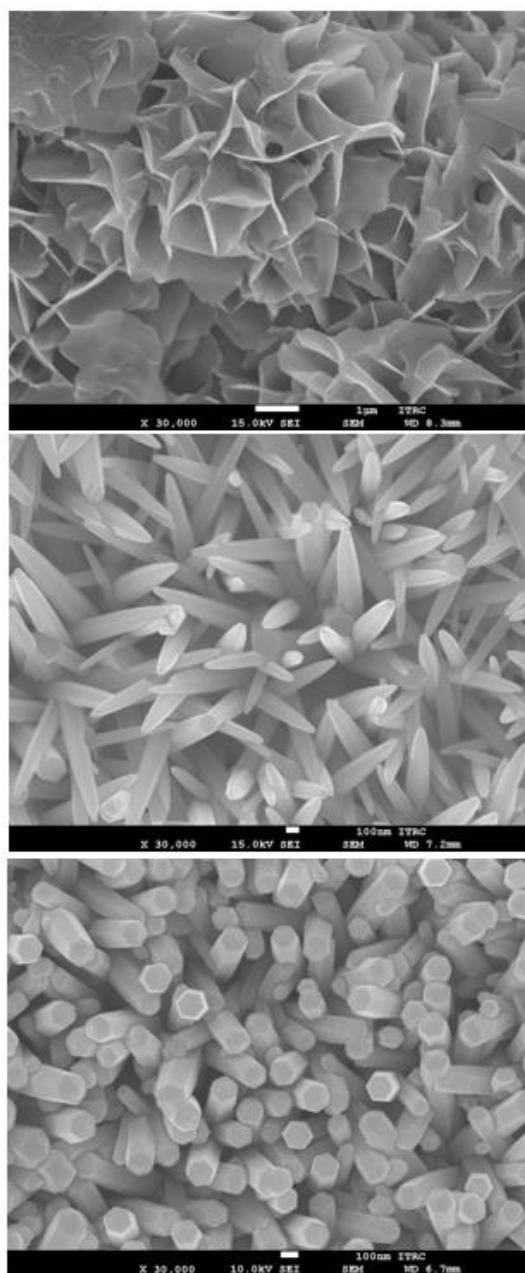


Figure S4.1.1. SEM images of ZnO nanorods grown with different temperature of the nutrient solution. (a) 40 °C (b) 70 °C (c) 90 °C.

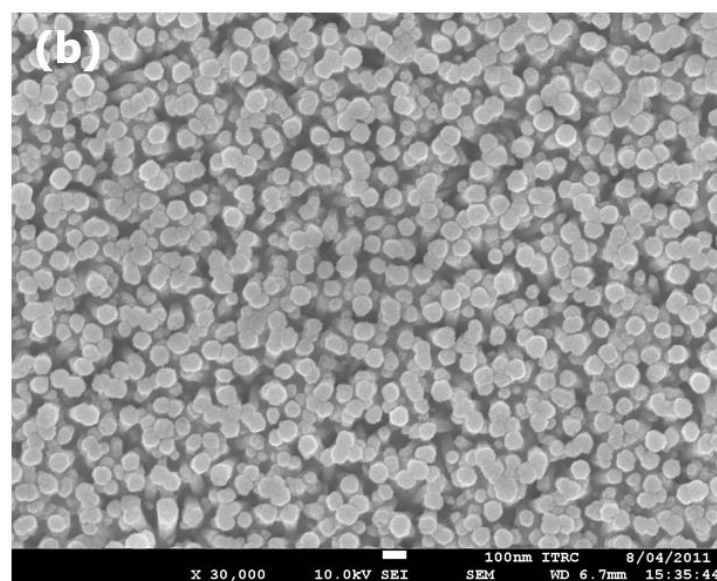
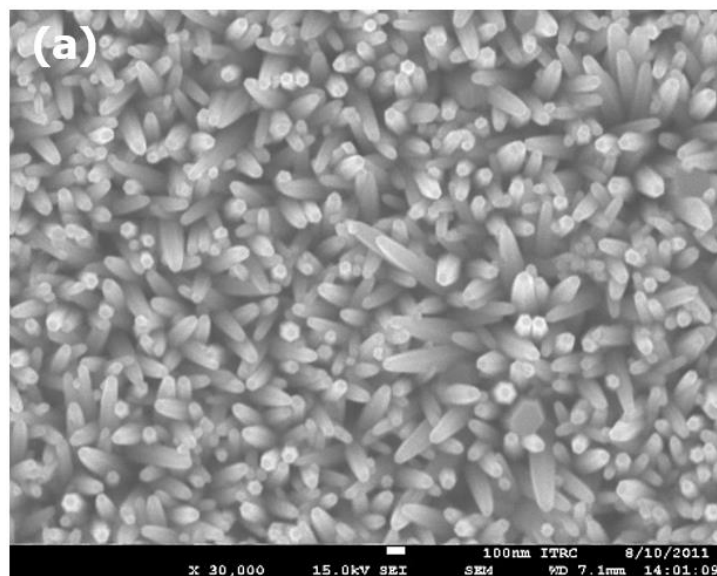


Figure S4.1.2. SEM images of ZnO nanorods grown with different concentration of ZnO colloid at temperature of 90 °C. (a) 0.03M (b) 0.05M.

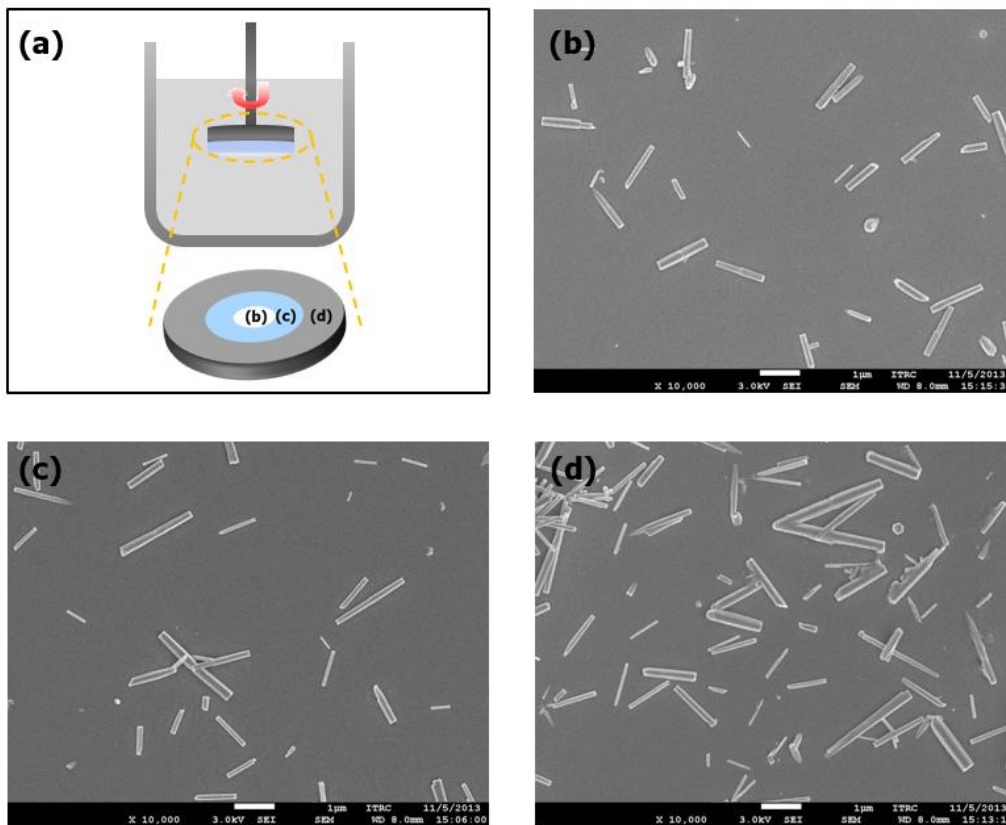


Figure S4.1.3. SEM images of ZnO nanorods grown with three spin coating times under shear stress at a rate of 100 rpm. (a) schematic diagram of experiment (b) center of Si substrate (c) centre-periphery of Si substrate (d) edge of Si substrate.

4.1.6. References

- [1] Pan Z, Dai Z, Wang Z. Nanobelts of semiconducting oxides. *Science* 2001, 291, 1947-1949.
- [2] Wu J, Liu S, Wu C, Chen K, Chen L. Heterostructures of ZnO-Zn coaxial nanocables and ZnO nanotubes. *Applied physics letters* 2002, 81, 1312-1314.
- [3] Yu K, Zhang Q, Wu J, Li L, Xu Y, Huang S, Zhu Z. Growth and optical applications of centimeter-long ZnO nanocombs. *Nano Research* 2008, 1, 221-228.
- [4] Wang Z. ZnO nanowire and nanobelt platform for nanotechnology. *Materials Science and Engineering: R: Reports* 2009, 64, 33-71.
- [5] Alammar T, Mudring A. Sonochemical synthesis of 0D, 1D, and 2D zinc oxide nanostructures in ionic liquids and their photocatalytic activity. *ChemSusChem* 2011, 4, 1796-1804.
- [6] Nadarajah A, Word R, Meiss J, Könenkamp R. Flexible inorganic nanowire light-emitting diode. *Nano letters* 2008, 8, 534-537.
- [7] Law M, Greene L, Johnson J, Saykally R, Yang P. Nanowire dye-sensitized solar cells. *Nature materials* 2005, 4, 455-459.
- [8] Emanetoglu N, Gorla C, Liu Y, Liang S, Lu Y. Epitaxial ZnO piezoelectric thin films for saw filters. *Materials Science in Semiconductor Processing* 1999, 2, 247-252.
- [9] Wang X, Summers C, Wang Z. Large-scale hexagonal-patterned growth of aligned ZnO nanorods for nano-optoelectronics and nanosensor arrays. *Nano Letters* 2004, 4, 423-426.
- [10] Huang M, Mao S, Feick H, Yan H, Wu Y, Kind H, Weber E, Russo R, Yang P. Room-temperature ultraviolet nanowire nanolasers. *Science* 2001, 292, 1897-1899.
- [11] Kaidashev E, Lorenz M, Von Wenckstern H, Rahm A, Semmelhack H, Han K, Benndorf G, Bundesmann C, Hochmuth H, Grundmann M. High electron mobility of epitaxial ZnO thin films on c-plane sapphire grown by multistep pulsed-laser deposition. *Applied Physics Letters* 2003, 82, 3901-3903.
- [12] Sivakumar K, Rosnagel S. Deposition of aluminum-doped zinc oxide thin films for optical applications using rf and dc magnetron sputter deposition. *Journal of*

Vacuum Science & Technology A 2010, 28, 515-522.

[13] Wei M, Boutwell R, Mares J, Scheurer A, Schoenfeld W. Bandgap engineering of sol-gel synthesized amorphous Zn_{1-x}Mg_xO films. Applied Physics Letters 2011, 98, 261913.

[14] Sun Y, Fuge G, Ashfold M. Growth of aligned ZnO nanorod arrays by catalyst-free pulsed laser deposition methods. Chemical Physics Letters 2004, 396, 21-26.

[15] Li C, Fang G, Su F, Li G, Wu X, Zhao X. Synthesis and photoluminescence properties of vertically aligned ZnO nanorod–nanowall junction arrays on a ZnO-coated silicon substrate. Nanotechnology 2006, 17, 3740.

[16] Qiu M, Ye Z, Lu J, He H, Huang J, Zhu L, Zhao B. Growth and properties of ZnO nanorod and nanonails by thermal evaporation. Applied Surface Science 2009, 255, 3972-3976.

[17] Yan M, Zhang H, Widjaja E, Chang R. Self-assembly of well-aligned gallium-doped zinc oxide nanorods. Journal of applied physics 2003, 94, 5240-5246.

[18] Grabowska J, Meaney A, Nanda K, Mosnier J, Henry M, Duclère J, McGlynn E. Surface excitonic emission and quenching effects in ZnO nanowire/nanowall systems: limiting effects on device potential. Physical Review B 2005, 71, 115439.

[19] Vayssieres L. Growth of arrayed nanorods and nanowires of ZnO from aqueous solutions. Adv. Mater. 2003, 15, 464-466.

[20] Kang B, Pearton S, Ren F. Low temperature (< 100°C) patterned growth of ZnO nanorod arrays on Si. Applied physics letters 2007, 90, 083104.

[21] Greene L, Law M, Goldberger J, Kim F, Johnson J, Zhang Y, Saykally R, Yang P. Low temperature wafer scale production of ZnO nanowire arrays. Angewandte Chemie International Edition 2003, 42, 3031-3034.

[22] Lee Y. J, Sounart T, Liu J, Spoerke E, McKenzie B, Hsu J, Voigt J. Tunable arrays of ZnO nanorods and nanoneedles via seed layer and solution chemistry. Crystal Growth and Design 2008, 8, 2036-2040.

[23] Kim Y. J, Yoon A, Kim M, Yi G. C, Liu C. Hydrothermally grown ZnO nanostructures on few-layer graphene sheets. Nanotechnology 2011, 22, 245603.

[24] Adamson A. Physical Chemistry of Surfaces. Wiley 1982.

- [25] Ohtaki H. Crystallization processes vol 3. John Wiley & Sons Inc 1998.
- [26] Qian R, Botsaris G. A new mechanism for nuclei formation in suspension crystallizers: the role of interparticle forces. Chemical engineering science 1997, 52, 3429-3440.
- [27] Blander M, Katz J. Bubble nucleation in liquids. AIChE Journal 1975, 21, 833-848.
- [28] Jennings J, Middleman S. Homogeneous nucleation of vapor from polymer solutions. Macromolecules 1985, 18, 2274-2276.
- [29] Chen L, Wang X, Straff R, Blizard K. Shear stress nucleation in microcellular foaming process. Polymer Engineering & Science 2002, 42, 1151-1158.
- [30] Hinch E, Acrivos A. Long slender drops in a simple shear flow. Journal of fluid mechanics 1980, 98, 305-328.
- [31] Ma T, Guo M, Zhang M, Zhang Y, Wang X. Density-controlled hydrothermal growth of well-aligned ZnO nanorod arrays. Nanotechnology 2007, 18, 035605.
- [32] Owen J, Roger R. Flow and heat transfer in rotating-disc systems, Vol. 1: Rotor-stator systems. Taunton: Research Studies Press 1989.
- [33] Shevchuk I. Convective heat and mass transfer in rotating disk systems. Springer 2009, 45.
- [34] Kármán T. Über laminare und turbulente Reibung ZAMM. Journal of Applied Mathematics and Mechanics/Zeitschrift für Angewandte Mathematik und Mechanik 1921, 1, 233-252.
- [35] Bejan A, Khair K. Heat and mass transfer by natural convection in a porous medium. International Journal of Heat and Mass Transfer 1985, 28, 909-918.

4.2. Heat diffusion of flexible ZnO/GO/PET film

4.2.1. Introduction

Excessive heating, due to the high power generation, is a limiting factor for a wide range of electronic devices [1-3]. Especially, the thermal management in micro-electronic equipment has been an important factor because of the significant increase in power densities against the decreasing of the scale. Hetero-structures fabricated by multi-layers of thin films have also shown very low thermal conductivity since the interfaces of multi-layers generate additional thermal resistance, which leads to increase the device temperature [4, 5]. Therefore, technologies and design are required to improve system efficiencies by dissipating heat fluxes.

Graphene is one of promising candidates for enhancing the heat dissipation behavior [6, 7]. Graphene, which is a two dimensional layer structure with sp^2 bonded network in atomic scale honeycomb lattice of carbon atom, has received a lot of attention from scientific and technological fields with its excellent electrical properties such as zero band gap electronic structure with low electrical resistivity (5.0×10^{-6} ohm.cm), superb mechanical properties and high thermal conductivity (3000 W/m·K) in the last few years [8-10]. These outstanding properties of graphene make it suitable for many applications such as transparent anodes, supercapacitor devices, lithium ion batteries, organic photovoltaic devices, etc [11, 12]. More importantly, the large-scale growth of single-layer and few-layer graphene on the flexible plastic substrates is one of the key issues to successful development of foldable, stretchable and transparent electronics [13, 14].

A technique for synthesizing large-scale graphene sheets using chemical vapor deposition (CVD) has been developed [15, 16]. However, some of these approaches require the use of a specific substrate material. Moreover, the high expense to maintain the ultrahigh vacuum (UHV) conditions significantly limits the use of these methods for large scale applications. Alternatively, several exfoliation techniques have been demonstrated which involve the oxidation of graphite oxide (GO) and the reduction via

thermal exfoliation, vacuum exfoliation or chemical exfoliation which can produce in large amounts of graphene sheets consisting of a few layers of 2 to 3 [17, 18]. Each of these techniques possesses definite pros and cons. Thermal treatment renders fine quality of graphene sheets but has to be carried out at extremely high temperature over 1000 °C. This energy-intensive process is unfit for mass production of graphene sheets because it is difficult to control this condition which is incompatible with plastic substrates. In addition, the failure to produce a single layer of graphene appears due to inadequate pressure and insufficient oxidation of graphite during thermal heat treatment stages. In vacuum exfoliation, the main drawbacks of this treatment are the time required for exfoliation and the cost-intensive components used in vacuum treatment. Many chemical treatments have also been reported that can produce a single layer of graphene sheets but are often inimical to the environment and inapplicable to the commercial production. Therefore, an appropriate processing method for assembling well-dispersed oxidized or reduced graphene nanosheets into thin films is required to fabricate highly controllable, conformal thin films.

Herein, we present a simple and facile approach of integrating graphene sheets into multilayers by layer-by-layer (LBL) technique to develop thermal, electrical and optical properties [19, 20]. In addition, graphene-based hybrid one-dimensional nanostructures have received enormous attentions due to their fascinating properties, offering potential applications in nanodevices, nanocomposites, and ultrathin membranes [21, 22].

One of the critical factors for the heat transport performance in thin films is the surface characteristics such as surface roughness [23, 24]. Recently, nanostructures have brought about the improvement of heat transfer with great industry interests [25, 26].

In this study, we considered a hydrothermal fabrication of zinc oxide (ZnO) nanostructures for dissipating the heat in reduced graphene oxide(rGO)/polyethylene terephthalate (PET) films. The influence of growth conditions such as concentration of the aqueous solution, temperature and growth time had been studied by controlling the morphology, dimension and density of the ZnO nanostructures on graphene sheets. In

order to achieve the direct growth of ZnO nanostructures on graphene layers, the heteroepitaxial relation between ZnO nanostructures and graphene sheets has been investigated. Moreover, the effect of nanostructured surfaces on rGO/ PET films was study to investigate the convective heat transfer characteristics. ZnO nanostructures have been reported for many potential applications in nanoelectronic and optoelectronic devices [27, 28]. Such a synergistic combination of attractive properties of ZnO nanostructures renders flexible and transparent nanodevices to the ZnO/rGO/PET hybrids.

4.2.2. Experimental Section

4.2.2.1. Preparation of graphene/PET film

Graphene oxide (GO) was synthesized from natural graphite powder by a modified Hummers method [17]. After being purified by filtration, subsequent dialysis and centrifugation, GO was exfoliated into water by ultrasonication for 30 min using a Branson Digital Sonifier (S450D, 500 W, 30 % amplitude). The prepared GO was re-dispersed in water to yield a brownish suspension, which was centrifuged to completely remove residual salts and acids.

Freestanding GO was fabricated using a simple spin-coating method. The aqueous dispersion of GO was spun at 3000 rpm for 30 s on PET substrate. After the GO/PET film was completely dried under room temperature, an integral layer of GO with smooth surfaces could be easily fabricated. The thickness of the GO/PET film could be freely tailored by controlling the spin-coating times of the GO dispersion. The GO/PET film was subsequently reduced to rGO/PET film by chemical method. In a typical procedure, the GO/PET film was directly immersed into a hydrazine (HI) solution in a sealed cuvette at room temperature for 1 h. The HI-rGO/PET film was washed with deionized (DI) water several times. Finally, rGO/PET film was obtained after being dried at room temperature for 10 h [29].

4.2.2.2. Preparation of ZnO nanorods on rGO/PET substrates

ZnO nanostructures were grown on rGO/PET substrates using a hydrothermal technique. ZnO seeds were prepared into 10 mM zinc acetate ($\text{Zn}(\text{C}_2\text{H}_3\text{O}_2)_2$) dissolved in ethanol solution at 60 °C for 5 min. Sol-gel method was carried out by coating the seed solution at a spin rate of 1000 rpm for 10 s and 3000 rpm for 20 s. In order to grow ZnO nanorods well onto the surface of graphene layers, the as-prepared aqueous solution was thermally annealed at 60 °C for 6 h. The surface-treated rGO/PET film was used as the place for the growth of ZnO nanorods which were synthesized. ZnO

nanorods were developed by the continuous supply of zinc ions and hydroxyl radicals in the aqueous solution consisting of 25 mM zinc nitrate hexahydrate ($\text{Zn}(\text{NO}_3)_2 \cdot 6\text{H}_2\text{O}$), 25 mM hexamethylenetetramine ($\text{C}_6\text{H}_{12}\text{N}_4$, HMT) and DI water. The main growth of ZnO nanorods was carried out at 90 °C for 3 h. Finally, few layers of graphene sheets with ZnO nanostructures on the PET substrate were dried at 40 °C for several hours in air ambient. The synthesis of ZnO/rGO/PET film was summarized schematically as shown in figure 4.2.1.

4.2.2.3. Characterization of ZnO nanorods/reduced graphene oxide/PET films

The synthesized ZnO/rGO/PET specimens were coated with platinum in vacuum for 300 s using a sputter coating machine (Sputter Coater-108, Cressinton Scientific Instruments, Watford, UK). Surface morphology of the materials was observed with a field emission scanning electron microscope (FE-SEM, JSM-6390LV, JEOL, Tokyo, Japan) to investigate internal structure.

Raman spectroscopy analysis was performed in order to investigate the surface defect of each sort of GO and rGO sheets by using a Raman spectrometer (LabRAM HR Evolution, HORIBA Ltd., Kyoto, Japan) equipped with an integral microscope (Olympus BH2-UMA, Olympus Co., NY, USA). The 514.54 nm radiation from a 16 mW air cooled Ar Ion laser (Model 127, Spectra Physics, Irvin, CA, U.S.A.) was used as an excitation source. All the spectra were obtained over a spectral range of 800 ~ 3500 cm^{-1} .

X-ray photoelectron spectroscopy (XPS, AXIS-HSi, Kratos, Kyoto, Japan) was used to determine chemical composition on the surface of ZnO/rGO/PET films [30]. The analysis was carried out with the Mg X-ray source at a power of 150 W in the pressure of 1×10^{-8} Torr.

The X-ray diffraction (XRD) measurements of the ZnO/rGO/PET specimens were performed on a Rigaku D/Max diffractometer with Cu $K\alpha$ radiation to determine the structure of the films [31].

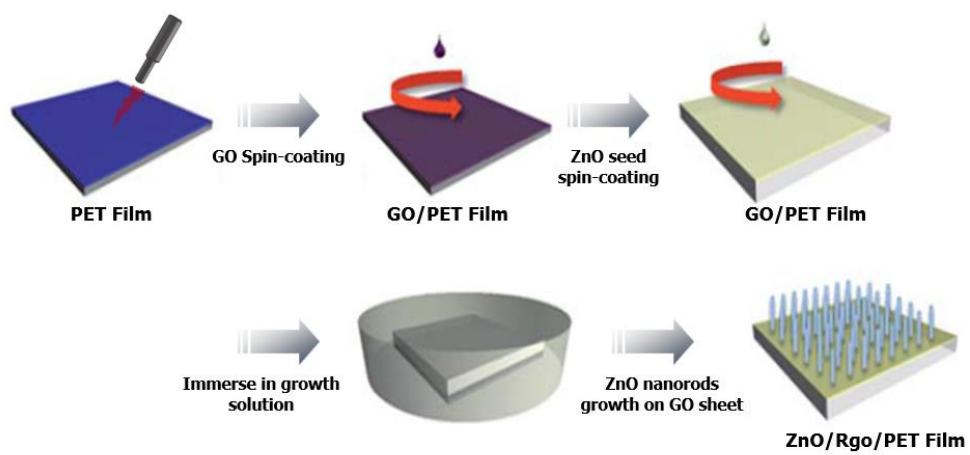


Figure 4.2.1. Processing procedure for preparation of ZnO/rGO/PET films.

The specific surface area of ZnO/rGO/PET films was measured by the Brunauer-Emmett-Teller method (BET method, ASSP 2010, Micromeritics, Norcross, GA, USA). The ZnO/rGO/PET samples were heated to 150 °C and 40 °C under vacuum (10^{-5} Torr) for 2 and 24 h to remove the adsorbed species, respectively. Nitrogen adsorption data were acquired at 77 K. All nitrogen adsorption/desorption measurements were equilibrated for 10 s before being recorded.

In order to investigate the heat transport of the ZnO/rGO/PET specimens, a time-dependent one-dimensional joule heating was used [32]. The rGO sheets were deposited onto PET substrate as both current collector and electrodes [33]. Copper wires were connected by a silver paste and a DC current was applied on the ZnO/rGO/PET film through a power supply (APS3005S) as a voltage source. Visual infrared thermometer (FLUKE VT04) was used to measure the temperature rise during device operation.

4.2.3. Results and Discussion

The FE-SEM images clearly reveal the typical morphology of ZnO nanostructures on rGO/PET films as shown in figure 4.2.2. Figure 4.2.2(c) shows a plane view FE-SEM image of the highly abundant ZnO nanorod arrays grown vertically and a wide distribution over the entire surface of graphene nanosheets [34].

The selective nucleation and growth of ZnO nanostructures heteroepitaxially on graphene sheets may be attributed that ZnO nanorods appear quite uniform diameters, lengths and densities.

Raman spectroscopy is a valuable technique to characterize the defect on graphene sheets. Figure 4.2.3 shows Raman spectra of the GO and rGO nanosheets. As depicted in figure 4.2.3, two dominant peaks at 1350 cm^{-1} and 1580 cm^{-1} were observed in the Raman spectra, namely the D and G bands, respectively. The D band was a breathing mode of π -point phonons of A_{1g} symmetry, which was usually attributed to the existence of disorder in the graphitic lattice and some defects which were induced during the manufacturing process and located at the edge of graphene sheets [35]. The reason why the carbon structure is disorder is the nano-sized graphitic planes and other forms of carbon such as vacancies, kinks and heteroatoms. The G band was generally ascribed to the E_{2g} phonon of sp^2 bonds of carbon atoms in graphene layers. The magnitude of D band peak dropped by a reduction of the GO/PET film, and the intensity ratio between the D and G bands of graphene nanosheets in Raman spectroscopy decreased ranging from 0.95 to 0.90, indicating a decreasing disorder of carbon structure [36].

XPS analyses were performed to investigate the effect of composition of graphene sheets on the ZnO/rGO/PET films. Figure 4.2.4 illustrates the C1s deconvolution spectrum of GO and rGO sheets [37]. As shown in figure 4.2.4(b), compared with graphene oxide, the intensities of all C1s peaks of the carbon binding to oxygen, especially the peak of C=O, decreased dramatically, indicating that most of the oxygen-containing functional groups were removed.

Figure 4.2.5 shows the XRD patterns of GO/PET and ZnO/rGO/PET film,

respectively. In GO/PET film, PET represented a diffraction peak centered at $2\theta = 27^\circ$. GO denoted the characteristic peak at $2\theta = 9.8^\circ$ indicating the d-spacing of 0.9 nm [38, 39]. In contrast, no characteristic peak at $2\theta = 9.8^\circ$ displayed and the new reflection of the ZnO/rGO/PET films exhibited one dominant peak at $2\theta = 34.3^\circ$, corresponding to the ZnO wurtzite structure. It can be seen that the ZnO nanorods are well-oriented and perpendicular to substrate surface, which attributed to [0002] direction [40, 41].

As shown in figure 4.2.6, the saturated temperature and the response time were different between rGO/PET and ZnO/rGO/PET films when the input power was supplied with a constant voltage. rGO sheets were heated by Joule heating, where heat was dissipated from surface of ZnO/rGO/PET film through convection [42, 43]. To investigate the structural effect on convective heat transfer, ZnO nanostructures were grown on rGO/PET substrate. The temperature was increased exponentially with time and reached the saturated equilibrium value at long time limit [44, 45]. However, the saturated temperature of ZnO/rGO/PET film was lower than that of rGO/PET film, which could be explained by the surface roughness of the nanostructures and convective heat transfer mechanism. In general, input power is balanced by the heat power loss. The equation for convective power loss is given by the following equation.

$$Q = hA(T - T_s) \quad (4.2.1)$$

where h is the convective heat transfer coefficient, A is the surface area, and T_s is the initial surface temperature. It is obvious that change in the saturated temperature depends on the convective heat transfer coefficient and the surface area. From the BET results listed in Table 4.2.1, since increasing the surface areas on the the ZnO/rGO/PET film may have generated a larger convective heat transfer coefficient, internal heat in the ZnO/rGO/PET film can more readily release to outside. Overall, the fabrication of nanostructures on the film had a great effect on the thermal dissipation of the film.

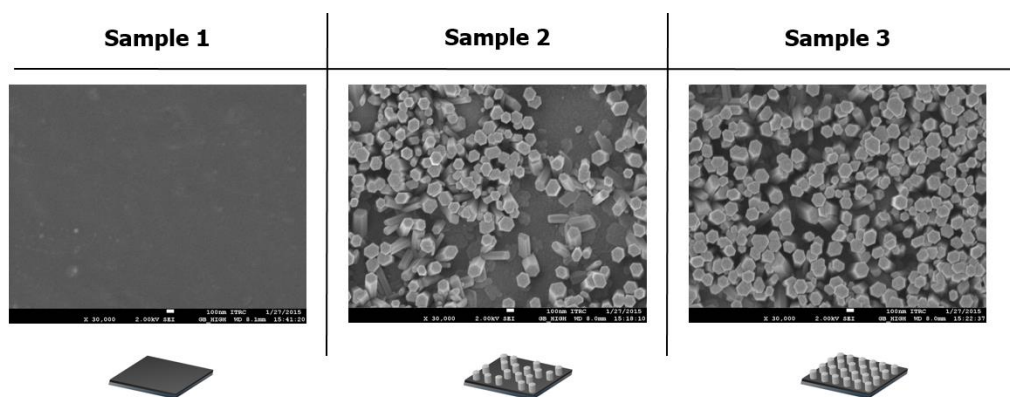


Figure 4.2.2. SEM images of graphene film specimens: (a) rGO/PET film, (b) rGO/PET with sparse ZnO nanostructures, and (c) rGO/PET with abundant ZnO nanostructures.

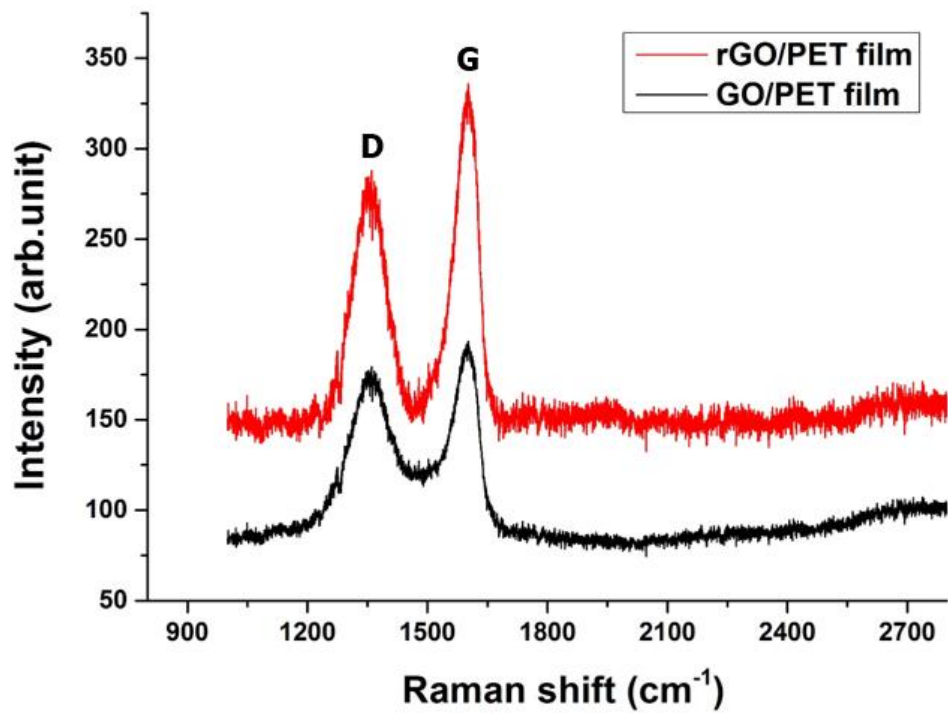


Figure 4.2.3. Raman spectra of graphene oxide/PET and reduced graphene oxide film.

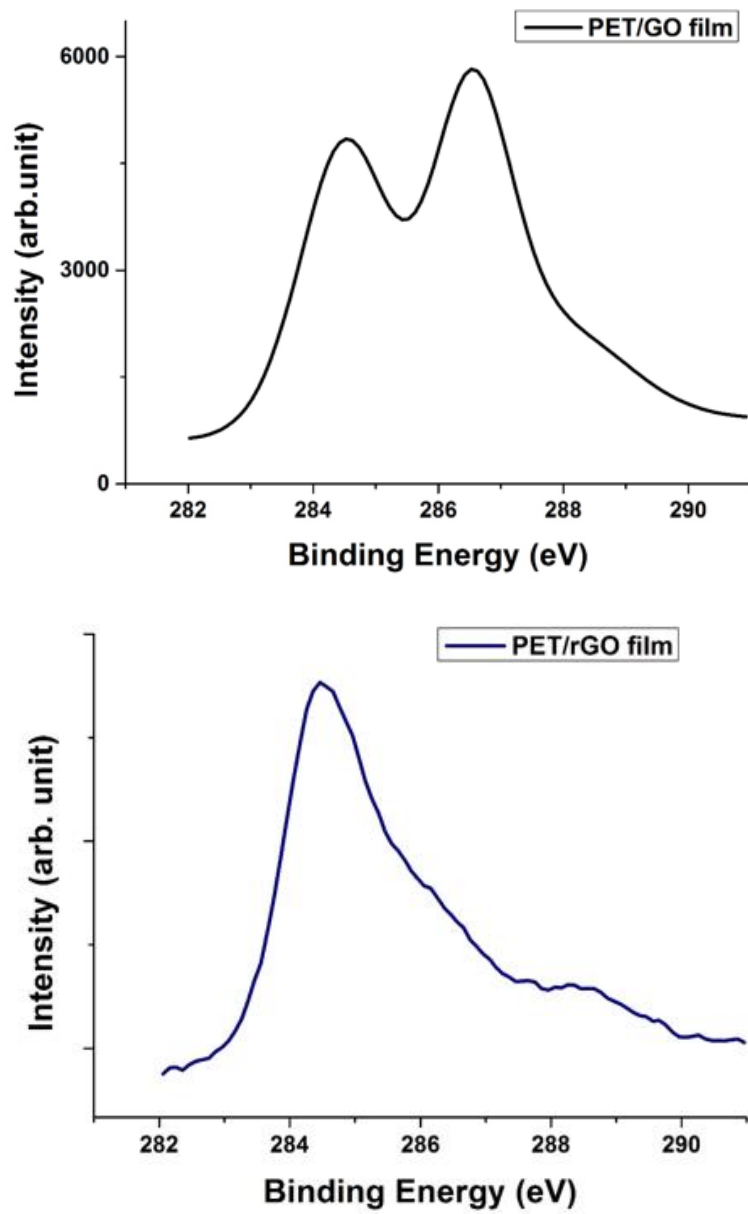


Figure 4.2.4. XPS spectra of (a) graphene oxide/PET film, and (b) reduced graphene oxide/PET film.

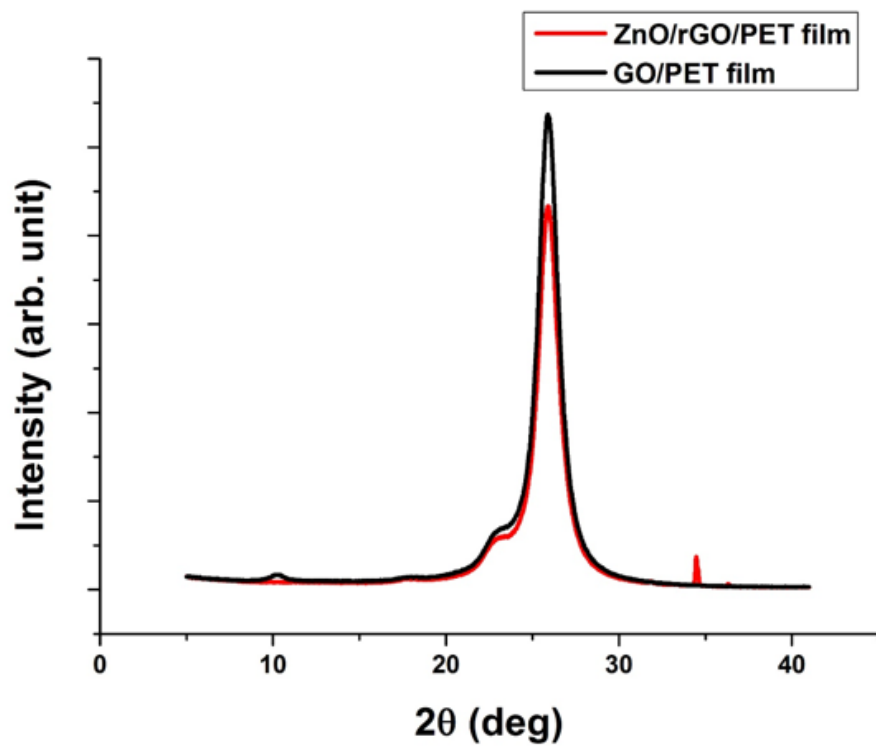


Figure 4.2.5. XRD spectra of graphene oxide/PET film and reduced graphene oxide/PET films with ZnO nanostructures.

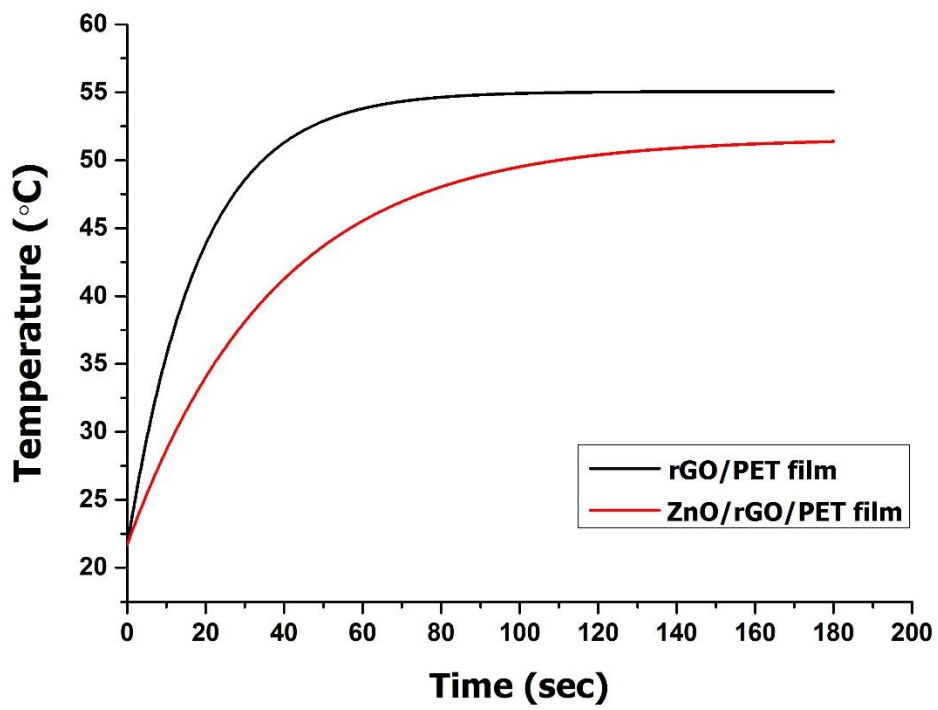


Figure 4.2.6. Temperature profiles of rGO/PET with and without ZnO nanostructures.

4.2.4. Summary

Uniformed large area graphene films, which is suitable for heat conduction and heat sink, were developed by the LBL assembly technique. Vertical oriented ZnO nanostructures were synthesized on the graphene/PET films by using a hydrothermal method. We demonstrated that the structural properties of GO and rGO with and without ZnO nanorods were studied. Compared with a pure rGO/PET film, the thermal dissipation properties of the film with nanostructures were enhanced significantly due to the effect of nanostructures. The noteworthy phenomenon in the thermal properties is attributed to the nano-sized assemblies. Therefore, the results obtained from this study show that ZnO nanostructures grown on rGO/PET film have a great potential application such as thermal management in nanoelectronics.

4.2.5. References

- [1] Min G, Rowe D. Cooling performance of integrated thermoelectric microcooler. *Solid-State Electronics* 1999, 43, 923-929.
- [2] Schroder D, Babcock J. Negative bias temperature instability: Road to cross in deep submicron silicon semiconductor manufacturing. *Journal of Applied Physics* 2003, 94, 1-18.
- [3] Chen G. *Nanoscale energy transport and conversion: a parallel treatment of electrons, molecules, phonons, and photons.* Oxford University Press 2005.
- [4] Goodson K., Ju Y. Heat conduction in novel electronic films. *Annual Review of Materials Science* 1999, 29, 261-293.
- [5] Zou J, Balandin A. Phonon heat conduction in a semiconductor nanowire. *Journal of Applied Physics* 2001, 89, 2932-2938.
- [6] Kang, J, Kim H, Kim K. S, Lee S. K, Bae S, Ahn J. H, Kim Y. J, Choi J. B, Hong B. H. High-performance graphene-based transparent flexible heaters. *Nano letters* 2011, 11, 5154-5158.
- [7] Sui D, Huang Y, Huang L, Liang J, Ma Y, Chen Y. Flexible and transparent electrothermal film heaters based on graphene materials. *Small* 2011, 7, 3186-3192.
- [8] Novoselov K, Geim, A, Morozov S, Jiang D, Zhang Y, Dubonos S, Grigorieva I, Firsov A. Electric field effect in atomically thin carbon films. *Science* 2004, 306, 666-669.
- [9] Novoselov K, Jiang D, Schedin F, Booth T, Khotkevich V, Morozov S, Geim A. Two-dimensional atomic crystals. *Proceedings of the National Academy of Sciences of the United States of America* 2005, 102, 10451-10453.
- [10] Lee C, Wei X, Kysar J, Hone J. Measurement of the elastic properties and intrinsic strength of monolayer graphene. *Science* 2008, 321, 385-388.
- [11] Schedin F, Geim A, Morozov S, Hill E, Blake P, Katsnelson M, Novoselov K. Detection of individual gas molecules adsorbed on graphene. *Nature materials* 2007, 6, 652-655.
- [12] Bae S, Kim H, Lee Y, Xu X, Park J. S, Zheng Y, Balakrishnan J, Lei T, Kim H. R,

Song Y. I. Roll-to-roll production of 30-inch graphene films for transparent electrodes. *Nature nanotechnology* 2010, 5, 574-578.

[13] Li X, Zhu Y, Cai W, Borysiak M, Han B, Chen D, Piner R, Colombo L, Ruoff R. Transfer of large-area graphene films for high-performance transparent conductive electrodes. *Nano letters* 2009, 9, 4359-4363.

[14] Ruiz-Vargas C, Zhuang H, Huang P, van der Zande A, Garg S, McEuen P, Muller D, Hennig R, Park J. Softened elastic response and unzipping in chemical vapor deposition graphene membranes. *Nano letters* 2011, 11, 2259-2263.

[15] Reina A, Jia X, Ho J, Nezich D, Son H, Bulovic V, Dresselhaus M, Kong J. Large area, few-layer graphene films on arbitrary substrates by chemical vapor deposition. *Nano letters* 2008, 9, 30-35.

[16] Kim K. S, Zhao Y, Jang H, Lee S. Y, Kim J. M, Kim K. S, Ahn J. H, Kim P, Choi J. Y, Hong B. H. Large-scale pattern growth of graphene films for stretchable transparent electrodes. *Nature* 2009, 457, 706-710.

[17] Li D, Müller M. B, Gilje S, Kaner R, Wallace G. Processable aqueous dispersions of graphene nanosheets. *Nature nanotechnology* 2008, 3, 101-105.

[18] Fowler J, Allen M, Tung V, Yang Y, Kaner R, Weiller B. Practical chemical sensors from chemically derived graphene. *ACS Nano* 2009, 3, 301-306.

[19] Kovtyukhova N, Ollivier P, Martin B, Mallouk T, Chizhik S, Buzaneva E, Gorchinskiy A. Layer-by-layer assembly of ultrathin composite films from micron-sized graphite oxide sheets and polycations. *Chemistry of Materials* 1999, 11, 771-778.

[20] Shen J, Hu Y, Li C, Qin C, Shi M, Ye M. Layer-by-layer self-assembly of graphene nanoplatelets. *Langmuir* 2009, 25, 6122-6128.

[21] Wang L, Wang Z, Zhang X, Shen J, Chi L, Fuchs H. A new approach for the fabrication of an alternating multilayer film of poly (4-vinylpyridine) and poly (acrylic acid) based on hydrogen bonding. *Macromolecular rapid communications* 1997, 18, 509-514.

[22] Such G, Quinn J, Quinn A, Tjipto E, Caruso F. Assembly of ultrathin polymer multilayer films by click chemistry. *Journal of the American Chemical Society* 2006, 128, 9318-9319.

- [23] Koo J, Kleinstreuer C. Analysis of surface roughness effects on heat transfer in micro-conduits. *International Journal of Heat and Mass Transfer* 2005, 48, 2625-2634.
- [24] Shen S, Xu J, Zhou J, Chen Y. Flow and heat transfer in microchannels with rough wall surface. *Energy Conversion and Management* 2006, 47, 1311-1325.
- [25] Yoon Y. H, Song J. W, Kim D, Kim J, Park J. K, Oh S. K, Han C. S. Transparent Film Heater Using Single-Walled Carbon Nanotubes. *Advanced materials* 2007, 19, 4284-4287.
- [26] Wu Z, Xu Q, Wang J, Ma J. Preparation of large area double-walled carbon nanotube macro-films with self-cleaning properties. *Journal of Materials Science & Technology* 2010, 26, 20-26.
- [27] Huang M. H, Mao S, Feick H, Yan H, Wu Y, Kind H, Weber E, Russo R, Yang P. Room-temperature ultraviolet nanowire nanolasers. *Science* 2001, 292, 1897-1899.
- [28] Wang X, Zhu H, Xu Y, Wang H, Tao Y, Hark S, Xiao X, Li Q. Aligned ZnO/CdTe core-shell nanocable arrays on indium tin oxide: synthesis and photoelectrochemical properties. *ACS nano* 2010, 4, 3302-3308.
- [29] Becerril H, Mao J, Liu Z, Stoltenberg R, Bao Z, Chen Y. Evaluation of solution-processed reduced graphene oxide films as transparent conductors. *ACS nano* 2008, 2, 463-470.
- [30] Wang S, Zhang Y, Abidi N, Cabrales L. Wettability and surface free energy of graphene films. *Langmuir* 2009, 25, 11078-11081.
- [31] Chieu T, Dresselhaus M, Endo M. Raman studies of benzene-derived graphite fibers. *Physical Review B* 1982, 26, 5867.
- [32] Bae M. H, Ong Z. Y, Estrada D, Pop E. Imaging, simulation, and electrostatic control of power dissipation in graphene devices. *Nano letters* 2010, 10, 4787-4793.
- [33] Dorgan V, Bae M. H, Pop E. Mobility and saturation velocity in graphene on SiO₂. *Applied Physics Letters* 2010, 97, 082112-082112-082113.
- [34] Tian Z, Voigt J, Liu J, McKenzie B, McDermott M, Rodriguez M, Konishi H, Xu H. Complex and oriented ZnO nanostructures. *Nature materials* 2003, 2, 821-826.
- [35] Ferrari A, Meyer J, Scardaci V, Casiraghi C, Lazzeri M, Mauri F, Piscanec S, Jiang D, Novoselov K, Roth S. Raman spectrum of graphene and graphene layers. *Physical*

review letters 2006, 97, 187401.

[36] Kudin K, Ozbas B, Schniepp H, Prud'Homme R, Aksay I, Car R. Raman spectra of graphite oxide and functionalized graphene sheets. *Nano letters* 2008, 8, 36-41.

[37] Stankovich S, Dikin D, Piner R, Kohlhaas K, Kleinhammes A, Jia Y, Wu Y, Nguyen S, Ruoff R. Synthesis of graphene-based nanosheets via chemical reduction of exfoliated graphite oxide. *Carbon* 2007, 45, 1558-1565.

[38] Xu J, Hu Y, Song L, Wang Q, Fan W, Liao G, Chen Z. Thermal analysis of poly (vinyl alcohol)/graphite oxide intercalated composites. *Polymer degradation and stability* 2001, 73, 29-31.

[39] Lerf A, Buchsteiner A, Pieper J, Schöttl S, Dekany I, Szabo T, Boehm H. Hydration behavior and dynamics of water molecules in graphite oxide. *Journal of Physics and Chemistry of Solids* 2006, 67, 1106-1110.

[40] Zhang H, Sun X, Wang R, Yu D. Growth and formation mechanism of c-oriented ZnO nanorod arrays deposited on glass. *Journal of crystal growth* 2004, 269, 464-471.

[41] Zhang C. High-quality oriented ZnO films grown by sol-gel process assisted with ZnO seed layer. *Journal of Physics and Chemistry of Solids* 2010, 71, 364-369.

[42] AngeláRodríguez-Perez M, de Saja J, AngeláLopez-Manchado M. Functionalized graphene sheet filled silicone foam nanocomposites. *Journal of Materials Chemistry* 2008, 18, 2221-2226.

[43] Pop E. Energy dissipation and transport in nanoscale devices. *Nano Research* 2010, 3, 147-169.

[44] Avilés F, Oliva A, Aznárez J. Dynamical thermal model for thin metallic film-substrate system with resistive heating. *Applied Surface Science* 2003, 206, 336-344.

[45] Oliva A, Maldonado R, Ceh O, Corona J, Riveros H. Study of a bimaterial system by an improved dynamical thermal model. *Surface Review and Letters* 2005, 12, 289-298.

V. Concluding Remarks

This study provides comprehensive information for micro/nano-scale materials such as heat transfer mechanism of silica aerogel composites, the thermal, mechanical, shape memory properties and the numerical modeling techniques for the deformation of the shape memory polyurethane foams, and theoretical, numerical modeling techniques for the crystallization, growth mechanism and thermal behaviors of the ZnO/graphene/PET film.

The thermal conductivity of a silica aerogel/epoxy composite was measured with respect to amount of as-received and plasma-treated aerogels. The silica aerogel/epoxy composites displayed a range of thermal conductivity values from 0.085 to 0.123 W/m·K. A high thermal conductivity was obtained for the composite fabricated by the typical liquid epoxy processing because the pores of the aerogels became filled with the epoxy resin during the processing of the composite. A preparation method for preserving the aerogel pores during the manufacturing process of the composite was proposed by using ethanol evaporation. The lowest thermal conductivity of 0.04 W/m·K was obtained for the composite containing the as-received aerogel of 75 vol% with preserved pores. The preserved aerogel pores in the composite were the most significant physical factor in determining the thermal conductivity of the composite. Another fabricating method was also developed in this study to manufacture silica aerogel composites by forming interfaces between superhydrophobic silica aerogels and the hydrophilic PVA solution. The silica aerogel/PVA composites are prepared by stirring the PVA resin to precipitate over the interfaces. Well-preserved aerogel pores were observed in the PVA-coated composites using an electron microscope and a low thermal conductivity of 0.022 W/m·K was achieved, which is only 11 % of the thermal conductivity of PVA. By assuming that the pores in silica aerogels are well kept in composites, the volume fraction of the silica aerogel is the most important factor for the thermal conductivity.

Shape memory polyurethane foams were prepared in this study by using the

salt leaching method. The thermal conductivity and specific compressive stress of SMPU foams was modelled theoretically and numerically to compare with experimental results. Thermal conductivity of the SMPU foam was decreased with decrease in the pore size of the foam while the mechanical properties of SMPU foams was increased with decrease in the pore size. We also demonstrated that the hybrid SMPU foam composed of dual scale pore size of 100 and 400 μm exhibited low thermal conductivity of 0.047 $\text{W/m}\cdot\text{K}$ he mechanical and superior specific compressive stress because of the low slenderness ratio and synergistic effect. All SMPU foam specimens displayed high shape recovery of 98 % and fixity. This study presents a novel actuation method for SMPU foams filled with carbon nanotubes (CNTs). DSC analysis on the SMPU/CNT composites showed that the transition temperature of SMPU/CNT composites decreased from 51.1 to 47.3 $^{\circ}\text{C}$ when increasing the CNT content from 0 to 0.1 wt%. Results from the thermal and mechanical tests also displayed that the embedded CNTs can be positive effect to enhance the thermal insulation and thermo-mechanical properties of SMPU/CNT foams. Moreover, the thermogravimetric investigation exhibited that the thermal stability of SMPU/CNT foams enhanced by increasing amount of CNT. Shape memory properties of SMPU/CNT foams were characterized by microwave exposure. Shape recovery of SMPU/CNT foams was triggered as the embedded CNTs could be absorbed the external electromagnetic energy. The absorption ratio of microwave radiation increased with addition of CNTs content. The composition of internal structure and appropriate weight fraction of the CNTs in the SMPU foams is an important factor determining the thermal insulation properties.

Zinc oxide (ZnO) nanorods were synthesized using shear effect of a rotating fluid in this study. Because the orientation and dimensions of ZnO nanorods are significantly affected by the applied shear stress, theoretical and numerical analyses were conducted to investigate the effect of the shear stress on the fabrication of ZnO nanorods. We demonstrated that the density of ZnO nanorods was increased with increasing the shear stress on the substrate surface because the variation in the concentration boundary layer thickness on the surface led to form diverse dimensions

of the ZnO nanorods on each place of substrate. Therefore, this study is expected to provide an influential method for manufacturing structurally gradient nanostructures in a very efficient way based on the knowledge of the physics associated with nanomaterial engineering and hydrodynamics.

The graphene-based PET films with improved uniformity were successfully prepared by reducing graphene oxide into graphene nanosheets. ZnO nanostructures were also grown vertically on the graphene/PET films using a hydrothermal method. We found that zinc acetate dehydrate is an essential element to grow ZnO nanorods on the surface of graphene sheets. Moreover, the aspect ratio and density of the nanostructure depended strongly on the concentration of seed solution and growth solution. The formation of vertically aligned ZnO nanorods was observed resulting from the nucleated seed of ZnO at graphene surface. The ZnO/graphene/PET films exhibited a significant improvement on the thermal dissipation characteristics. As a representative example, the increase of heat flux was achieved by increasing surface areas of the ZnO/graphene/PET films. Upon the degree of surface area of the films, it is assumed that there might be a critical point for enhancement of heat dissipation characteristics.

Korean Abstract

본 연구에서는, 다양한 구조와 물성을 가진 고분자 복합재료에서 발생하는 열전달 현상을 포함한 물리적인 특성에 대한 이해를 다루고 있다.

일반 고분자 복합재료보다 단열 특성을 강화하기 위해, 실리카 에어로겔을 사용하여 폼 구조를 지닌 고분자 복합재료를 제조하였다. 실리카 에어로겔의 비표면적이 열전달에 미치는 영향을 살펴보기 위해, 실리카 에어로겔 표면을 플라즈마 처리를 하였고 브루нау어-에메트-텔러(Brunauer-Emmett-Teller, BET) 방법과 전계 방출 주사 전자 현미경(Field Emission Scanning Electron Microscope, FE-SEM)으로 평가하였다. 또한, 표면 처리된 실리카 에어로겔을 에폭시 수지에 분산시켜 나노복합재료를 제조하여 각각의 재료에 대해서 내부 구조와 열적 특성을 평가하였다. 그 결과 순수한 실리카 에어로겔을 이용한 복합재료에 비해 플라즈마 처리를 통해 비표면적이 증가한 실리카 에어로겔을 이용한 에폭시 복합재료가 더 낮은 열전도도를 나타내었다. 이는 증가된 나노 구조로 인해 복합재료 안에서의 경계면 열 저항이 증가하여 포논의 이동이 억제되었기 때문이다.

본 연구에서는 실리카 에어로겔의 기공을 보호하면서 형태를 안정화시킬 수 있는 효과적인 바인더로서 폴리비닐알코올(polyvinyl alcohol, PVA)이 고려되었다. 폴리비닐알코올을 사용하여 제조된 실리카 에어로겔-PVA 복합재료의 열전도도는 실리카 에어로겔-에폭시 복합재료보다 더 낮은 열전도도를 나타내었다. 이는 기존에 연구된 실리카 에어로겔-에폭시 복합재료와는 달리 친수성을 지닌 폴리비닐알코올이 소수성을 지닌 실리카 에어로겔의 기공에 스며들지 않고 실리카 에어로겔의 표면에 코팅됨에 따라 실리카 에어로겔의 기공은 유지하면서 형태가 안정화되었기 때문이다.

본 연구에서는 능동적인 단열 재료를 개발하기 위하여 형상기억 폴리우레탄(Shape memory polyurethane, SMPU) 폼을 제조하였다. 형상기억 폴리우레탄은 전 중합반응(prepolymerization) 방법으로 합성되었고 전이온도를 파악하기 위하여 시차주사 열량측정법(Differential Scanning Calorimetry,

DSC)으로 평가하였다. 형상기억 폴리우레탄은 염류 용탈 작용(Salt leaching) 방법을 사용하여 폼 구조로 제조하였고 다양한 크기를 지닌 염화 나트륨(sodium chloride, NaCl)을 사용하여 형상기억 폴리우레탄 폼의 기공 크기를 조절하였다. 또한, 서로 다른 크기의 기공이 임의적으로 섞여있는 하이브리드 폼과 서로 다른 크기의 기공들이 각각 층을 이루고 있는 기능성 폼을 제조하여 기공의 크기와 미세 구조에 따른 폼의 열적, 기계적, 형상 회복력 등 물리적 특성을 비교하였다. 열적 특성을 수치적으로 계산하기 위해 그릭만(Grickman)과 로슬랜드(Rosseland) 이론을 사용하였으며, 형상기억 폴리우레탄 폼 구조에서 기공의 크기가 미치는 효과를 설명하기 위해 새로운 인자를 제안하였다. 예측된 결과는 정량적으로, 정성적으로 실험 결과와 잘 일치하였다. 형상기억 폴리우레탄 폼의 구조에 따른 기계적 물성 평가를 위해 3차원 구조 해석이 수행되었다. 단일 기공 크기로 이루어진 형상기억 폴리우레탄 폼에 비해 다중 기공 크기로 이루어진 하이브리드 형상기억 폴리우레탄 폼이 더 높은 기계적 강도를 나타내었고, 실험결과와 잘 일치하였다.

본 연구에서는 외부 자극 요인으로 열 뿐만 아니라 극초단파(microwave)에도 반응하여 형상기억을 조절할 수 있도록 다중벽 탄소나노튜브(Multi-Walled Carbon Nanotube, MWCNT)를 사용하였다. 다중벽 탄소나노튜브의 균진 분산을 위하여 초음파 처리를 이용하여 형상기억 폴리우레탄-MWCNT 복합재료를 제조하였다. 염류 용탈 작용 방법으로 제조된 형상기억 폴리우레탄-MWCNT 폼의 열적, 기계적, 형상회복·고정력, 극초단파 효과를 측정하였다. 형상기억 폴리우레탄 폼에 다중벽 탄소나노튜브의 무게분율이 조금씩 증가함에 따라 기계적 강도가 증가하고 극초단파(Microwave)를 통해서도 높은 형상 기억 회복율과 고정율을 나타내었지만 다중벽 탄소나노튜브의 적외선(infrared, IR) 감쇠기 역할로 인해 열전도도는 큰 변화가 없음을 확인하였다.

나노 크기를 지닌 재료의 기하학적 구조가 물질의 열전달에 미치는 효과를 연구하기 위해 산화아연을 사용하였다. 여러 가지 나노 크기를 갖는 일차원 구조(나노 막대기, 나노 벨트, 나노 벽 구조)는 양자 크기 효과로 인해 마이크로미터 크기의 벌크 물질들에서 볼 수 없었던 높은 열·전기 특

성을 나타내고 있어 벌크 물질들이 가진 여러 문제점 들을 해결할 수 있는 새로운 대안으로 제시되고 있다.

본 연구에서는 다양한 일차원 구조를 지닌 산화아연 나노 막대기 어레이를 수열 합성법을 통해 합성하였다. 박막의 표면과 단면은 전계 방출 주사 전자 현미경으로 평가하였고, 산화아연 성장 용액의 온도와 농도, 산화아연 성장 용액의 농도, 산화아연 씨앗 용액의 스핀 코팅 횟수에 따라 다양한 형태를 지닌 산화아연 나노 막대기가 성장한 것을 확인하였다.

본 연구에서는 유체 흐름 안에서의 산화아연 나노 막대기의 성장에 대해 연구를 하였다. 회전 흐름을 제어하기 위한 장치가 고안되었고, 회전으로 인해 기판 표면에서 생기는 전단 응력이 산화아연 나노 막대기의 성장 배향성과 크기에 미치는 영향에 대해 연구를 하였다. 그 결과 기판의 중앙 부분에 비해 끝부분에서 성장한 산화아연 나노 막대기가 수직 배향성을 나타내었고, 크기가 더 큰 산화아연 나노 막대기로 성장한 것을 확인하였다. 이는 회전으로 인해 기판 표면에서 생기는 전단 응력이 산화아연 나노 막대기의 핵 생성, 핵 밀도, 물질 이동에 영향을 더욱 많이 미치기 때문이다. 유체역학적 모델을 핵생성 이론에 적용하여 전단응력에 의한 효과를 이론적으로 분석하였고, 모멘텀과 물질 이동 현상을 모사하기 위해 유한요소법이 사용되었다. 예측된 결과는 측정된 실험과 잘 일치하는 결과를 보였다.

본 연구에서는 폴리에틸렌 테레프탈레이트(polyethylene terephthalate, PET)/그래핀 필름위에 다양한 패턴으로 산화아연 나노 막대기를 성장하였을 때, 필름 표면에서 생성된 나노 구조가 필름의 열전달에 미치는 효과를 연구하였다. 산화그래핀은 수정된 허머스(Hummers) 방법을 통해 제조하였고, 화학적으로 박리된 산화그래핀 용액을 사용해 폴리에틸렌 테레프탈레이트 필름 표면에 스핀 코팅 방법을 통해 증착시켰다. 환원된 그래핀/폴리에틸렌 테레프탈레이트 필름의 화학결합 상태는 X선 광전자 분광법(X-ray Photoelectron Spectroscopy, XPS), 라만 분광법(Raman spectroscopy)을 통해 평가하였다. 그래핀/폴리에틸렌 테레프탈레이트 필름 표면위에 산화아연 나노 막대기가 성장한 것을 X선 회절(X-Ray Diffraction, XRD) 분석과 전계 방출 주사 전자 현미경을 사용하여 확인하였고, 성장한 산화아연 나노 막대기의 패턴에 따른 비표면적의 차이를 브루нау어-에메트

-텔러 방법을 통해 확인하였다. 제조된 필름의 비표면적 변화에 따른 열전달 효과를 확인하기 위해 열류계를 사용하였다. 산화아연 나노 막대기의 밀도가 높을수록 열 유속이 보다 향상된 결과를 나타내었으며, 나노 구조로 인해 비표면적이 증가할수록 방열 효과가 증가하는 상관성을 가지는 것을 확인하였다.

주요어; 열이동 현상, 열전도도, 단열, 계면 저항, 실리카 에어로겔, 형상 기억 폴리우레탄, 폼 구조, 유한 요소 해석, 다중벽 탄소나노튜브, 방열, 산화아연, 그래핀, 나노구조, 계면 효과

학번: 2010-20595